

AD 642540

AD 113.

EDC FILE COPY

Final Report

Thermal Optic Distortion

CLEARINGHOUSE
FOR FEDERAL SCIENTIFIC AND
TECHNICAL INFORMATION

Hardcopy

Microfiche

\$ 3.00

\$.65

113 pp

as

1 ARCHIVE COPY

NOV 30 1966



Westinghouse

ELECTRIC CORPORATION

Final Report

Thermal Optic Distortion

Report Period: 16 June 1965 to 1 October 1966

Contract NOnr - 4874 (00)

ARPA Order No. 306 Project Code 4730

Prepared for

OFFICE OF NAVAL RESEARCH

Washington, D. C.

Westinghouse General Order WGD-38538-KD

Project Supervisor: Mr. I. T. Basil

Authors:

E. P. Riedel

G. D. Baldwin

This research is a part of Project DEFENDER under the joint sponsorship of the Advanced Research Projects Agency, the Office of Naval Research, and the Department of Defense.

Westinghouse Electric Corporation

P.O. Box 1897

Baltimore, Md. 21203

MDE 1198

ABSTRACT

The Final Report on Contract Nonr-4874(00) "Thermal Optic Distortion" quantitatively describes the optical distortion in neodymium doped glass which is induced by pump radiation. We have observed optical distortion at 6328Å and have found the optical path length dependent on four primary effects:

- 1) Change in physical length
- 2) Change in refractive index due to temperature rise
- 3) Change in index resulting from stress
- 4) Change in index associated with an excited state population of neodymium ions.

Section I presents the experimental techniques used and the results obtained throughout this contract. Included in this section are measurements of optical path length variations, pump-induced birefringence, change in physical length, change in refractive index, bulk temperature rise, and the deflection of a light beam.

In Section II, the theory of thermal optic distortion is developed for the first time to include Fermat's principle. This approach leads to equations defining both the slope and trajectory of rays through the material. The resulting equations are employed to predict ray refraction, beam divergence, and the optical path length through the material as a function of radius, time, and polarization.

Section III compares the results of Sections I and II. Good agreement between theory and experiment is achieved provided a new term is added to the expression for the change in refractive index. This term arises from the fact that the polarizability of the neodymium ion in its excited $^4F_{3/2}$ level is different from its value in the $^4I_{9/2}$ ground level. The inclusion of this new term in the expression for the change in refractive index implies that large optical distortions can exist in "athermalized" glass.

FOREWORD

This final technical report on Thermal Optic Distortion, Contract Number Nonr-4874(00), covers the period extending from 16 June, 1965 to 1 October, 1966. The objective of the contract was to formulate a mathematical model of pump-induced optical distortion in neodymium-glass laser rods and to verify this theory through experiment. The experimental measurements made during the course of this contract included interferometer measurements of optical path length variations, pump-induced birefringence, change in length and refractive index, bulk temperature rise, and the deflection of a light beam.

The general approach taken during this contract was to first measure pump-induced birefringence and the change in length of the laser rod. From this data, the temperature of the laser rod as a function of radius and time was calculated. This temperature distribution was then used to theoretically predict the results of interferometric measurements, refractive index change, bulk temperature rise, and the refraction of a light beam.

Three major sections comprise the body of this report. Section I deals with the experiments performed and the results obtained, Section II is concerned with the development of a theoretical model, while the final section shows the correlation which exists between the experimental results and the theory.

BLANK PAGE

CONTENTS

<u>Section</u>		<u>Page</u>
I	EXPERIMENTAL TECHNIQUES AND RESULTS	1-1
	A. Introduction	1-1
	B. Achievement of Radial Symmetry	1-1
	1 Optical Pump Geometry	1-1
	2 Effects of Residual Stress	1-2
	3 Laser Rod Support Effects	1-2
	4 Conclusions	1-3
	C. Quantative Optical Distortion Measurements	1-3
	1 Operating Range of Laser Rod	1-3
	2 Optical Path Length Variation	1-3
	3 Birefringence Measurements	1-15
	4 Change in Length and Refractive Index	1-19
	5 Thermocouple Temperature Rise Determination	1-27
	6 Small Diameter Light Beam Deflection	1-28
	7 Mach-Zehnder Optical Path Length Variation with Nonex Sheath	1-28
	8 Measurement of α_n	1-32
	9 Conclusions	1-33
	D. References - Section I	1-34
II	THEORETICAL CONSIDERATIONS	2-1
	A. Intrduction	2-1
	B. Ray Trajectories	2-1
	C. Optical Path Length	2-4
	D. Mach-Zehnder Analysis	2-6
	E. Birefringence Experiment - Analysis	2-9
	F. Small Diameter Beam Refraction and Amplifier Beam Divergence Angle	2-10
	G. Conclusions	2-11
	H. References - Section II	2-11
III	COMPARISON OF THEORY WITH EXPERIMENT	3-1
	A. Introduction	3-1
	B. Comparison of Theory with Experiment: Radial Dependence	3-1

CONTENTS (Continued)

<u>Section</u>		<u>Page</u>
	C. Refractive Index Change Due to Excited Neodymium Ion Population.	3-4
	D Conclusion	3-14
	E. References - Section III	3-16
IV	SUMMARY	4-1
V	RECOMMENDATIONS FOR FUTURE WORK	5-1
 APPENDICES		
A	Effects of Residual Stress	A-1
B	Laser Rod Support	B-1
C	Properties of Eastman Kodak Company Neodymium Glass Laser Rods	C-1
D	Properties of American Optical AOlux Neodymium Glass Laser Rods	D-1
E	Annealing Procedure Used for Rods AO-1 and AO-2	E-1
F	Physical Constants for Rod AO-2	F-1

LIST OF ILLUSTRATIONS

<u>Figure</u>		<u>Page</u>
1-1	Temporal Shape of Pump Source	1-4
1-2	Output vs. Input Energy for Rod AO-2	1-5
1-3(a)	Mach-Zehnder Fringe Pattern Photographs for Rod AO-2 (6400 Joules)	1-6
1-3(b)	Mach-Zehnder Fringe Pattern Photographs for Rod AO-2 (8,800 Joules)	1-6
1-3(c)	Mach-Zehnder Fringe Pattern Photographs for Rod AO-2 (11,500 Joules)	1-7
1-4	Radial Optical Path Length Variation for Rod AO-2 at 11,500j Pump Energy	1-9
1-5	Fringe Intensity Variation at $r/R = 0$ for Rod AO-2 at 11,500j Pump Energy	1-10
1-6	Total Phase Change at $r/R = 0$ for Rods AO-2 and AO-3	1-11
1-7	Percent Total Pump Energy Dissipated as a Function of Time	1-12
1-8	Mach-Zehnder Fringe Pattern Photographs for Rod AO-3 at 11,500j Pump Energy	1-13
1-9	Radial Optical Path Change Attributed to Nd^{+3} Concentration in Rod AO-2 at 11,500j Pump	1-14
1-10	Comparison Between Radial Optical Path Change Due to Nd^{+3} and Nd^{+3} Plus Host in Rod AO-2 at 11,500j Pump Energy	1-15
1-11	Experimental Diagram: Measurement of Pump Induced Birefringence. . .	1-16
1-12	Birefringence Development in Rod AO-2 at 11,500j Pump Energy	1-16
1-13	Radial Stress Phase Angle in Rod AO-2 at 11,500j Pump Energy	1-17
1-14	Comparison Between Residual and Pump Induced Stress in Rod AO-2 . .	1-18
1-15	Experimental Diagram: "Rod End" Interferometer	1-20
1-16	Mach-Zehnder Interferometer	1-20
1-17	"Rod-End" Interferometer	1-22
1-18	Fringe Count vs. Time for "Rod End" and Mach-Zehnder Interferometer for Rod AO-2	1-23
1-19	Change in Physical Length for Rod AO-2 at $r/R = 0$	1-24
1-20	Change in Refractive Index for Rod AO-2 at $r/R = 0$	1-25
1-21	Change in Physical Length for Rod AO-2 at 11,500j Pump Energy and for $r/R = 0$, $r/R = .44$, $r/R = .72$	1-26
1-22	Measured Bulk Temperature Rise in Rod AO-1	1-29
1-23	Experimental Diagram: Measurement of Light Beam Deflection	1-30
1-24	Light Beam Deflection for Rod AO-2 at 11,500j Pump Energy	1-31

LIST OF ILLUSTRATIONS (Continued)

<u>Figure</u>		<u>Page</u>
1-25	Experimental Diagram: Measurement of α_n	1-33
2-1	Ray Path Geometry	2-2
3-1	T(r, t) for Rod AO-2 at 11,500j Pump Energy	3-3
3-2	Calculated $n_r(r_o, t) - n_o$ for Rod AO-2 at 11,500j Pump Energy	3-5
3-3	Calculated $\theta_r(r_o, t)$ for Rod AO-2 at 11,500j Pump Energy	3-6
3-4	Experimental and Calculated Radial Optical Path Length Variation for Rod AO-2, 11,500j Pump Energy and $t = .38$	3-7
3-5	Experimental and Calculated Radial Optical Path Length Variation for Rod AO-2, 11,500j Pump Energy $t = 1.0$ ms	3-8
3-6	Refractive Index Component Change vs. Time at $r/R = 0$ for Rod AO-2 at 11,500j Pump Energy	3-9
3-7	Experimental Diagram: Measure of Temporal Variation in W(t)	3-13
3-8	Temporal Variation of P(t) and W(t) for Rod AO-2 at 11,500j Pump Energy	3-15

SECTION I. EXPERIMENTAL TECHNIQUES AND RESULTS

A. INTRODUCTION

This section of the Final Report on Contract Nonr-4874(00) is concerned with the experimental techniques used and the experimental results obtained throughout this contract. The most important product of the experimental work was quantitative data which was used to test the theory developed in Section II.

The ability to obtain reliable and usable quantitative data rests primarily on the achievement of good radial symmetry in the optical path length gradients across the rod diameter during the optical pump cycle. Without radial symmetry, the effect of pump-induced stress and resulting strain cannot be determined, while all other data obtained would be extremely difficult to interpret.

This section will, therefore, be concerned with two major topics. The first deals with achieving radial symmetry and the associated physical problems, while the second is concerned with the measurements of the laser rod's dynamic optical properties when exposed to a pump source.

B. ACHIEVEMENT OF RADIAL SYMMETRY

1. Optical Pump Geometry

The source used to optically pump the glass rods, which were 3/8 inch in diameter by 3 inches long, consisted of a 6-inch long xenon-filled helical lamp. The helical lamp had an inside diameter of 1.15 inches, and an outside diameter of 2.2 inches, with 9-1/2 coils along its length. Close coupled to the inside diameter of the lamp was a frosted pyrex sheath with a .06-inch wall thickness, while the outside diameter of the lamp was in contact with a heavy aluminum foil reflector. The purpose of the frosted Pyrex sheath was to prevent solarization of the Nd^{+3} rod and to diffuse the pump light before it fell on the laser rod. The aluminum reflector served to increase the total pump energy falling on the rod. The laser rod was supported in the center of the Pyrex sheath.

There were several reasons for choosing a 6-inch long helical lamp to pump a 3-inch long laser rod. Perhaps the most important was that the 6-inch lamp provided more even illumination along the length of the laser rod than a shorter lamp. An additional advantage was that the lamp (capable of dissipating 20,000 joules) was excited to a fraction of its maximum rating, thus providing very reproducible data throughout the experimental program.

The laser rod and cavity were air-cooled between firings with sufficient time allowed between shots for the rod to return to room temperature equilibrium.

2. Effects of Residual Stress*

If the residual stress in a laser rod is large compared to the stress induced during optical pumping, the measurement of the latter may be difficult or impossible. This is particularly true if the residual stress does not possess radial symmetry with respect to the rod axis. A study was therefore undertaken to determine the distribution, and where possible the magnitude, of residual stress existing in a number of glass rods and to observe the effect this residual stress had on the optical path length through the laser rod during the pump cycle. This investigation is covered in detail in Appendix A. It was observed that those rods which did not possess radially symmetric residual stress exhibited non-radial optical path length gradients and non-radial stress during the pump cycle. However, those rods which did have radially symmetric residual stress exhibited radially symmetric stress and optical path length gradients during the pump cycle.

In general, the achievement of radially symmetric optical distortions was dependent on the laser rod possessing either radially symmetric residual stress or zero stress. In addition, there were only two cases in which the residual stress appeared to be as large as the pump induced stress, while for all of the other glass rods tested, the residual stress appeared to be considerably less. The results of this study were used to select a rod (AO-2) which contained only radially symmetric residual stress and of magnitude small compared to the pump induced stress. This rod was used to take the quantitative data contained in this report.

3. Laser Rod Support Effects

Prior to determining the effects of residual stress it was found necessary to determine the distortion of the laser rod optical path caused by the laser rod supports. Basically, two types of distortion were observed. The first arose from air, which was heated at the laser rod surface, flowed around the end of the laser rod, and perturbed the optical path in the vicinity of the end of the rod. The mechanism of the second type of distortion is not yet known; however, it manifested itself by modulating the refractive index of the laser rod and appeared to originate at the point of contact between the laser rod and the rod support. The details of this investigation are to be found in Appendix B of this report.

* Residual Stress is defined as that stress present in a laser rod when the rod is at equilibrium room temperature.

After a thorough investigation of the distortion produced by several types of rod supports, a new support was designed and tested. It was found that the new rod support introduced no observable distortion.

4. Conclusion

The attainment of radially symmetric optical path length variations in a neodymium glass laser rod requires that three conditions be satisfied. It is necessary that the optical pumping cavity be so designed as to ensure uniform distribution of pump energy over the surface of the laser rod. One of two conditions with respect to residual stress must be met:

- (1) Residual stress must be small, or
- (2) the residual stress must possess radial symmetry.

Finally, it is imperative that the laser rod supports introduce no distortion. All three of these requirements have been met during this contract, thus enabling reproducible quantitative data to be obtained.

C. QUANTITATIVE OPTICAL DISTORTION MEASUREMENTS

1. Operating Range of Laser Rod

It was deemed necessary to demonstrate that the pump energies and pump cavity used to obtain the thermal-optic distortion data produced gain in the laser rod which was comparable with the gain being generated in operational laser systems. To this end, laser rod AO-2 (See Appendix A) was placed in a resonant cavity composed of a 70% reflecting front mirror and a 99%+ reflecting rear mirror. The laser rod was pumped at various energies, and the output energy in joules was recorded. Throughout this contract the light output from the lamp was temporally in the form of an unshaped pulse with a 3 db intensity duration of approximately 600 microseconds. The shape of the pump pulse is shown in figure 1-1, while figure 1-2 shows a plot of output versus input energy for rod AO-2. The low slope efficiency of .31% is not unusual considering the type of pumping cavity employed. Of major importance, however, is the fact that at the pump energies used to record the dynamic optical distortions (6400, 8800, and 11,500 joules), the laser rod possessed considerable gain.

2. Optical Path Length Variation

The dynamic optical path length variations in rod AO-2 were measured on a Mach-Zehnder interferometer and recorded by means of a Beckman and Whitley Model 350 high-speed framing camera. The experimental diagram is the same as that shown in figure A-2.* The framing camera was run at a speed of 35,900 frames per second. This speed yielded a

* Appendix A



Figure 1-1. Temporal Shape of Pump Source(200 μs /div.)

frame separation of 28 microseconds with a frame exposure time of 3 microseconds. Figure 1-3 shows some typical photographs obtained for 6400, 8800, and 11,500 joules into the helical lamp.

The film strip on which the fringe patterns were recorded was Kodak Shellburst Film. This film was developed in Kodak HC-110 developer at 68°F for 5 minutes. The film was calibrated so that relative intensity could be obtained by means of microdensitometer traces.

The phase change, measured from the center of the rod to the edge, was obtained from the microdensitometer traces in the following manner. In general, the fringe intensity at a fixed radius for the Mach-Zehnder Interferometer is given by¹

$$(I. 1) \quad I(r) = f(r) \left[1 + k g(r) + 2 \sqrt{k g(r)} \cos \delta(r) \right]$$

where $I(r)$ is the fringe intensity, $f(r)$ is the intensity in the arm of the interferometer not containing the laser rod, k is an intensity loss factor ($0 \leq k \leq 1$) introduced by the laser rod in one arm of the interferometer, $g(r)$ is a loss factor which accounts for the depolarization effects of stress, and $\delta(r)$ is the fringe phase angle. The maximum fringe intensity is given by

$$(I. 2) \quad I_{\max}(r) = f(r) \left[1 + k g(r) + 2 \sqrt{k g(r)} \right]$$

while the minimum intensity is given by

$$(I. 3) \quad I_{\min}(r) = f(r) \left[1 + k g(r) - 2 \sqrt{k g(r)} \right].$$

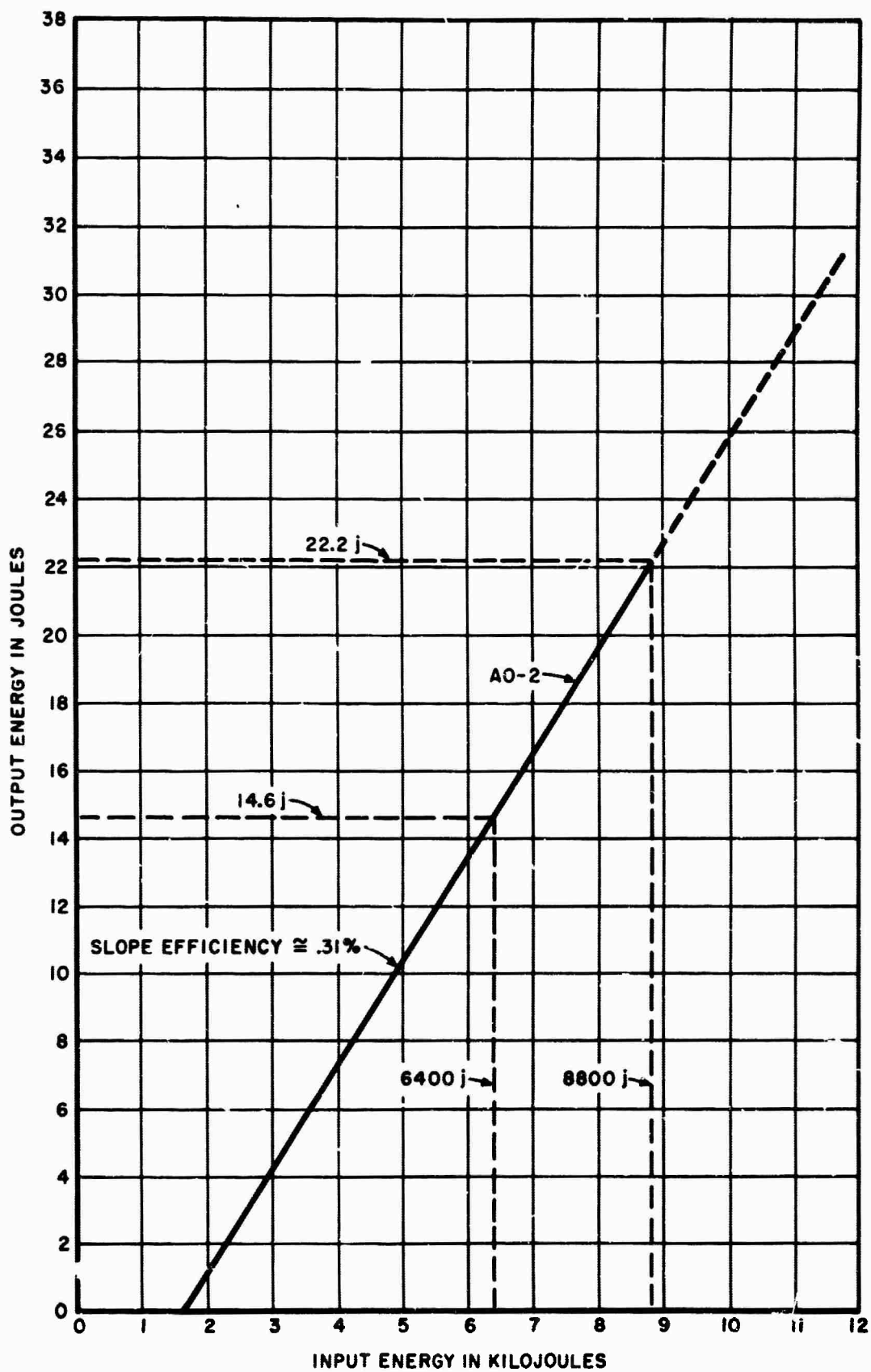


Figure 1-2. Output vs. Input Energy for Rod AO-2

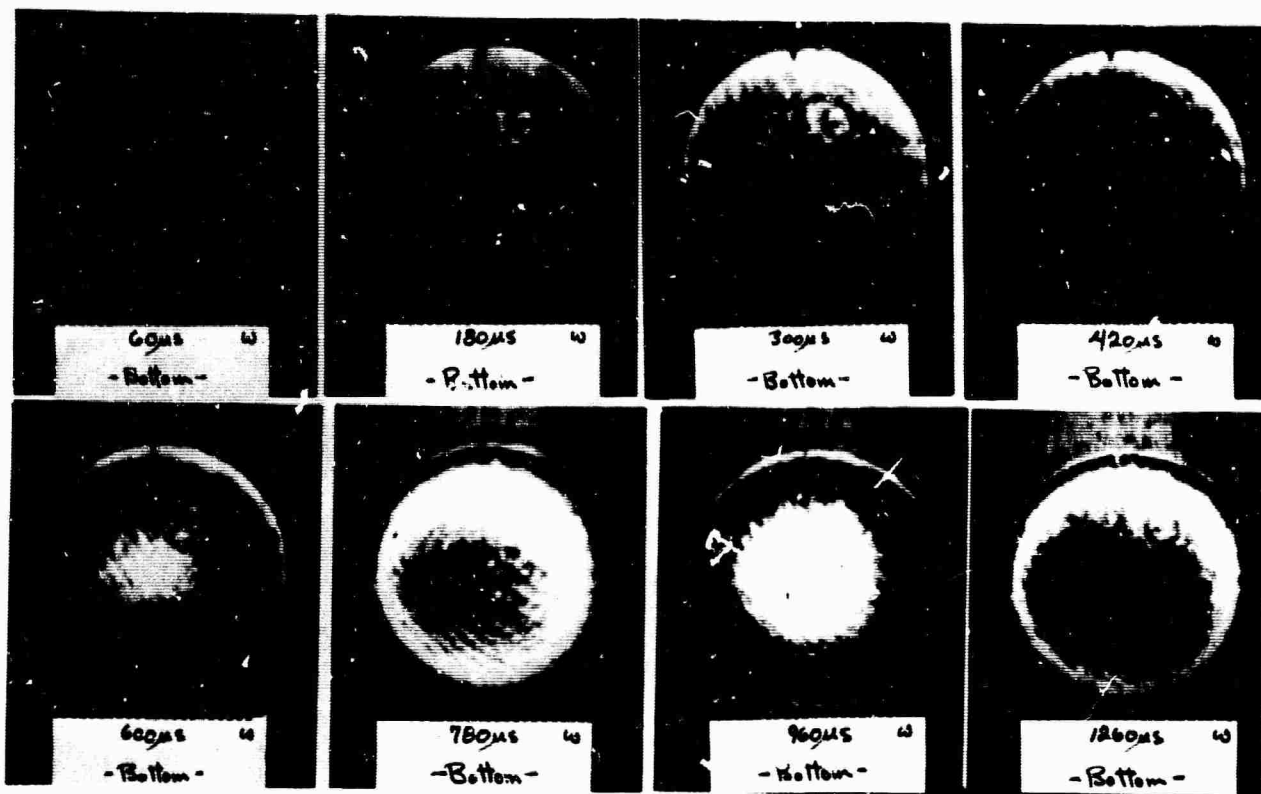


Figure 1-3(a). Mach-Zehnder Fringe Pattern Photographs for Rod AO-2 - (6,400 Joules)

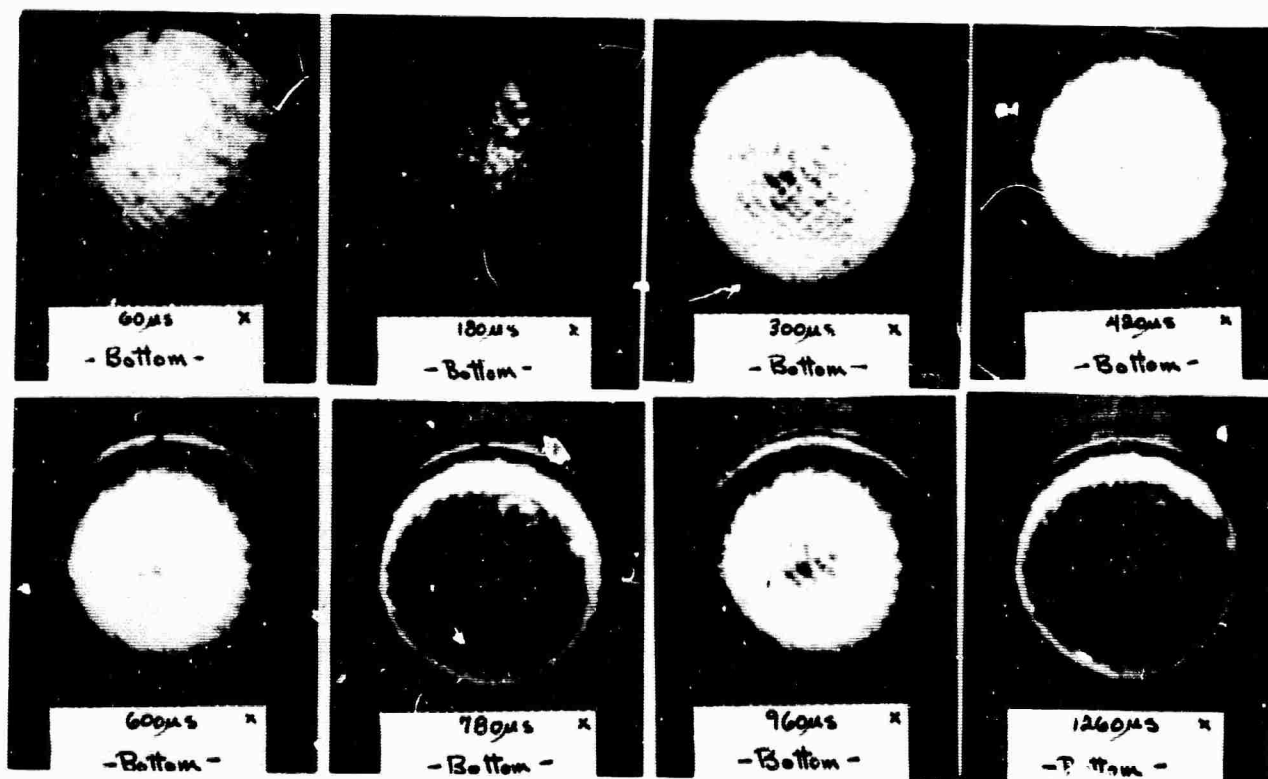


Figure 1-3(b). Mach-Zehnder Fringe Pattern Photographs for Rod AO-2 - (8,800 Joules)

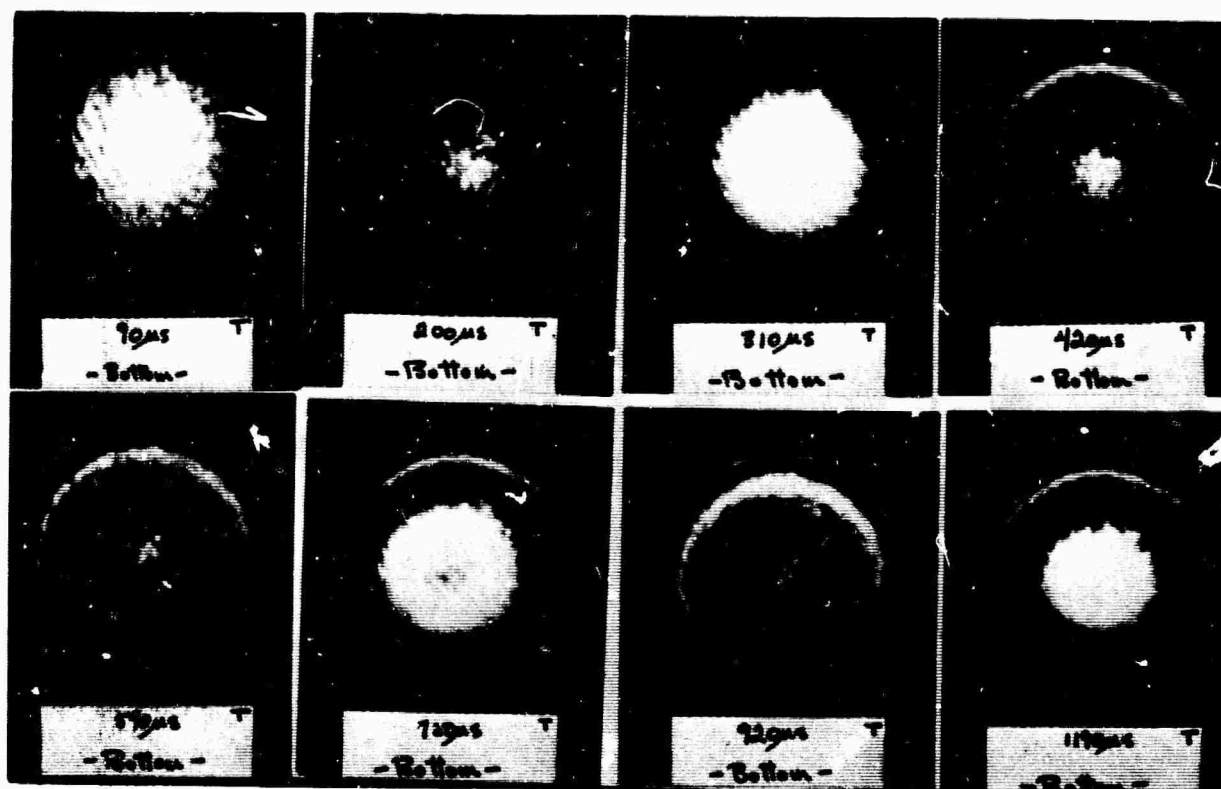


Figure 1-3(c). Mach-Zehnder Fringe Pattern Photographs for Rod AO-2 - (11,500 Joules)

For our experimental results it was found that $I_{\max}(r)$ and $I_{\min}(r)$ remained essentially constant from $r = 0$ to $r = R$. In addition, by running the microdensitometer traces parallel to the direction of the polarization of the He-Ne beam the value of $g(r)$ was 1. Since $\delta(r)$ was therefore taken for radially polarized radiation, we shall write $\delta(r)$ as $\delta_r(r)$ from now on to denote this fact. By next defining the quantity σ as the ratio $I_{\min}(r)/I_{\max}(r)$ and requiring that the value of $I_{\max}(r)$ be normalized to 1, the phase angle $\delta_r(r)$ can be expressed as

$$(I. 4) \quad \delta_r(r) = \cos^{-1} \left[\frac{\beta(r) - \oint (1+k)}{2 \oint \sqrt{k}} \right]$$

where

$$(I. 5) \quad k = \left[\frac{1 + \sqrt{\sigma}}{1 - \sqrt{\sigma}} \right]^2$$

$$(I. 6) \quad \oint = \frac{1}{1 + k + 2 \sqrt{k}}$$

and $\beta(r)$ is defined as the ratio $I(r)/I_{\max}(r)$.

Using equations (I. 4), (I. 5), and (I. 6) the phase angle across the rod radius was calculated for rod AO-2 at 11,500 joules pump energy for all frames between time t equal to zero (start of pump cycle) and $t = 1600$ microseconds (approximate end of pump cycle). Figure 1-4 shows this phase angle, normalized to zero at the center of the rod ($r/R = 0$), at selected times as a function of normalized radius r/R .

In addition to the relative phase angle across the rod, the high-speed photographs were used to give the total phase angle change at $r/R = 0$ as a function of time. First, the fringe intensity variation at $r/R = 0$ versus time was plotted, and from this curve the total phase angle change was determined. Figure 1-5 shows the intensity variation for 11,500 joules pump energy, while figure 1-6 shows the total phase angle change recorded at three separate pump energies for the doped AO-2 rod and at one energy for the undoped AO-3* rod. It is interesting to note that when the shape of the curves for the total phase angle change (figure 1-6) are compared to the shape of the curve for the percent of total light emitted from the flash lamp, figure 1-7, there is excellent agreement.

To determine the effect of the glass host on the observed optical distortions, an undoped AOlux rod (AO-3) was placed in the pumping cavity. A set of selected Mach-Zehnder fringe pattern photographs recorded at 11,500 joules is shown in figure 1-8. When comparison was made between the relative phase angle across the radius recorded for the doped rod (AO-2) with that for the undoped rod, there appeared to be no great difference between them. Thus, one must conclude that the relative phase angle across the radius as observed for the doped laser rod is primarily caused by the glass host. Although the addition of Nd^{+3} to the host did not greatly effect the relative phase angle across the radius induced by the pump, the total phase angle change was much greater for the doped rod. It can be seen from figure 1-6 that the maximum phase angle change for the doped rod is x2.7 greater than that observed for the host.

The optical path distortions noted for the undoped rod were probably caused by absorption of the U. V. pump radiation which passed through the pyrex sheath. This effect was aggravated for the AOlux host because its UV absorption band appeared to extend well into the visible blue region.

By analyzing the fringe patterns of the host in the same way as for the doped rod, the effect of the Nd^{+3} concentration alone could be determined. Four times were selected for comparison purposes. The total phase angle change for the undoped rod as a function of r/R was subtracted from the total phase angle change for the doped rod as a function of r/R , the resulting curves being shown in figure 1-9. In figure 1-10, the relative phase angle for Nd^{+3}

* See Appendix A

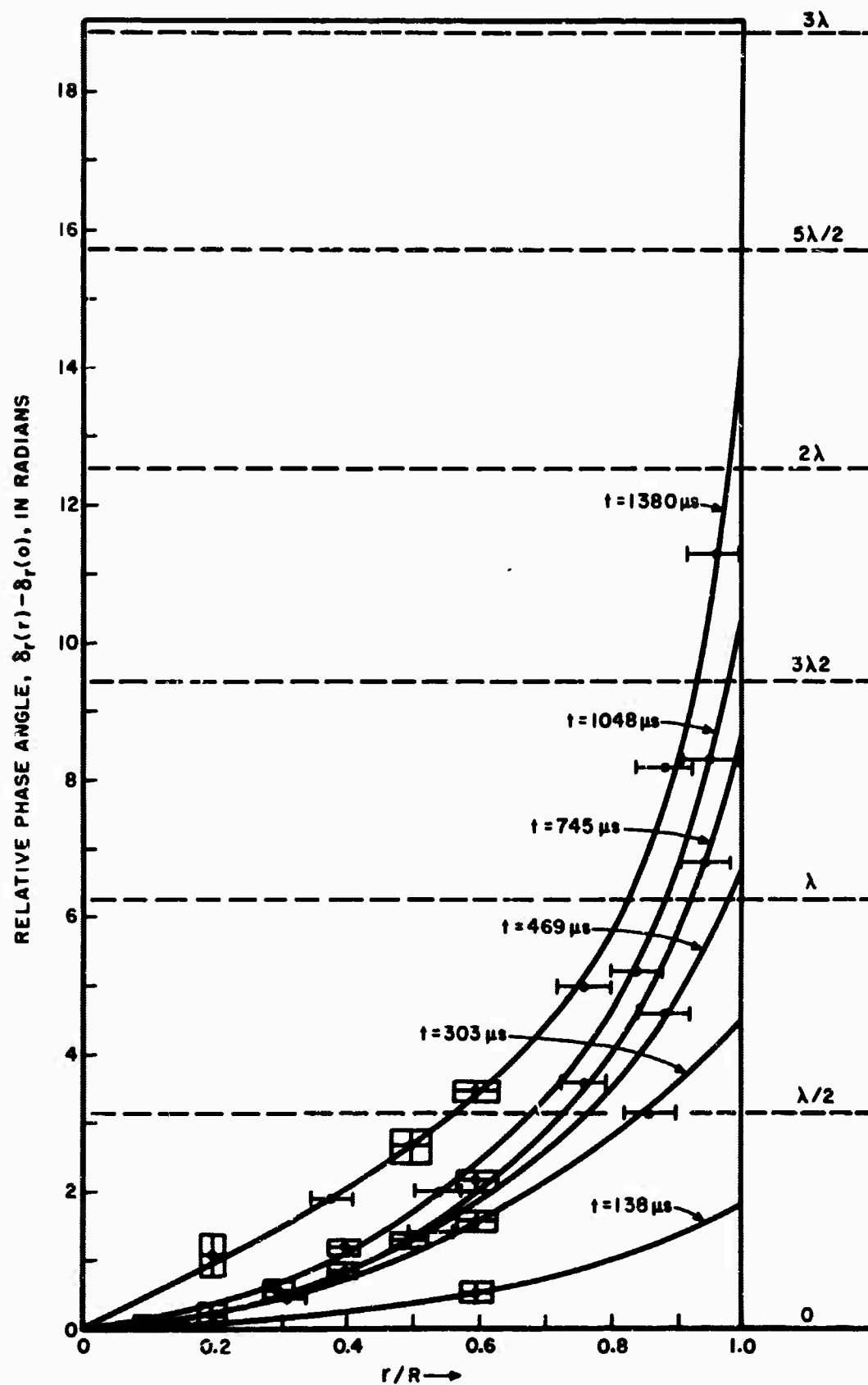


Figure 1-4. Radial Optical Path Length Variation for Rod AO-2 at 11,500j Pump Energy
(all curves normalized to zero at $r/R = 0$)

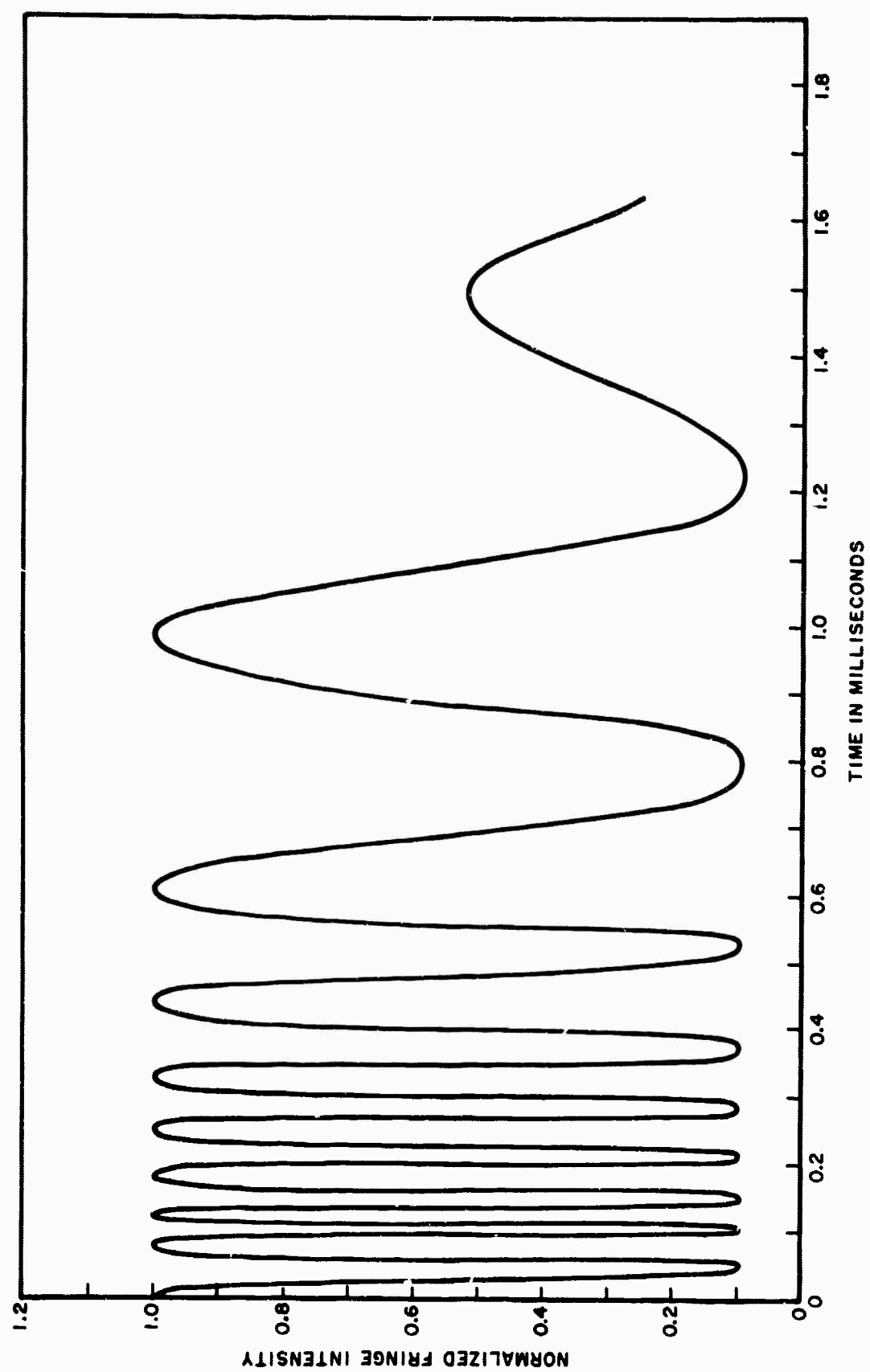


Figure 1-5. Fringe Intensity Variation at $r/R = 0$ for Rod AO-2 at 11,500j Pump Energy

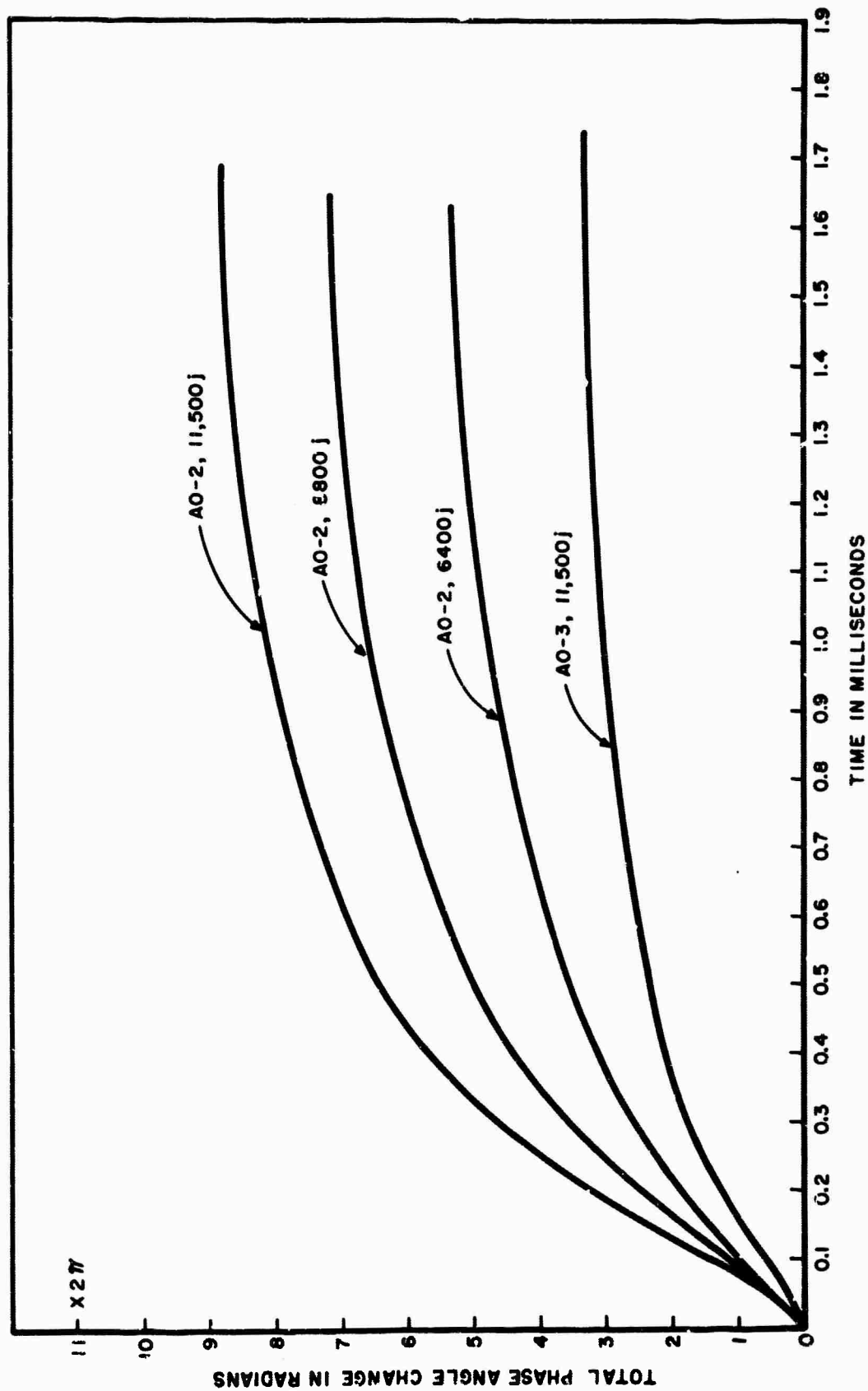


Figure 1-6. Total Phase Change at $r/R = 0$ for Rods AO-2 and AO-3

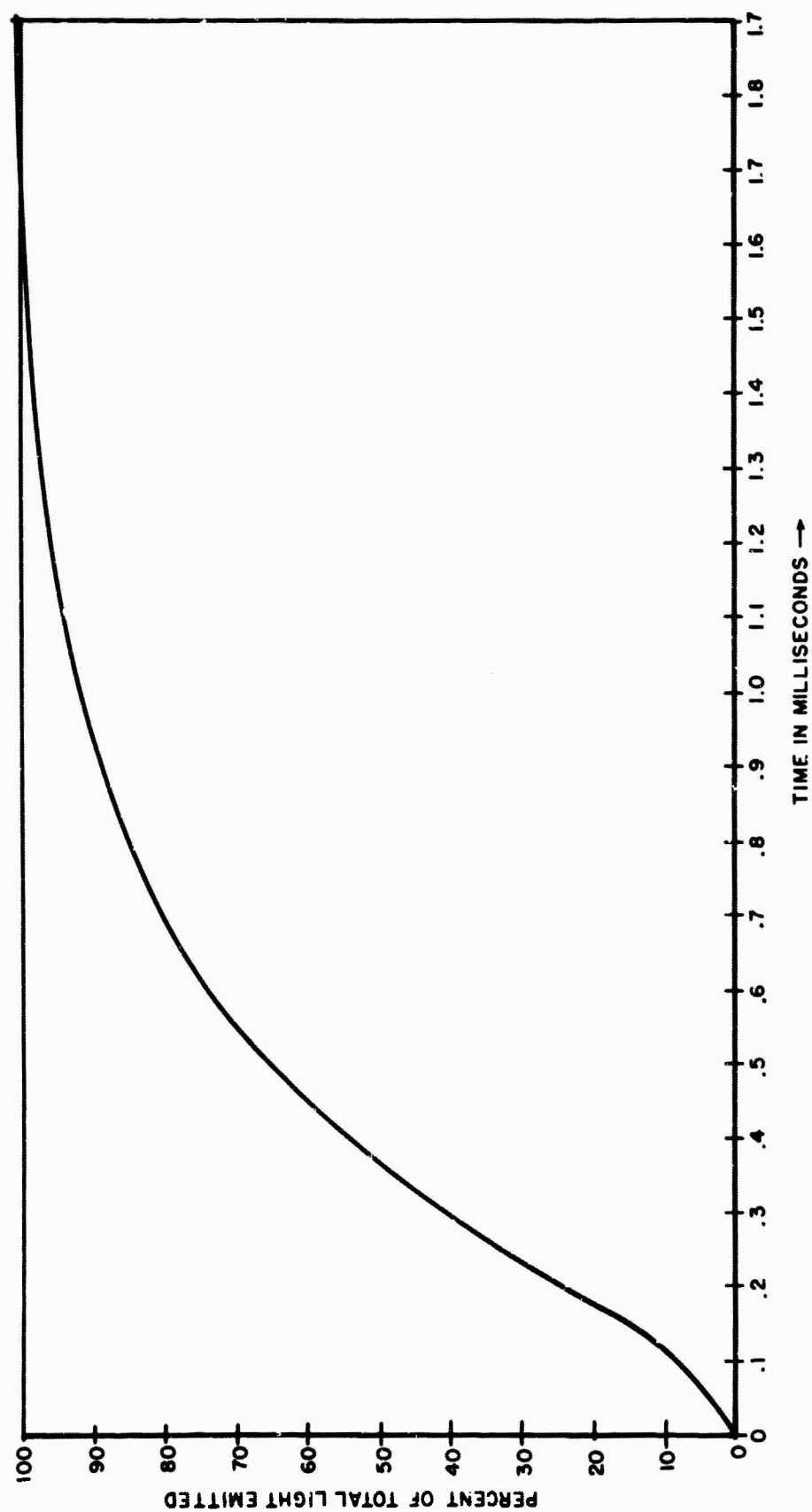


Figure 1-7. Percent Total Pump Energy Dissipated as a Function of Time

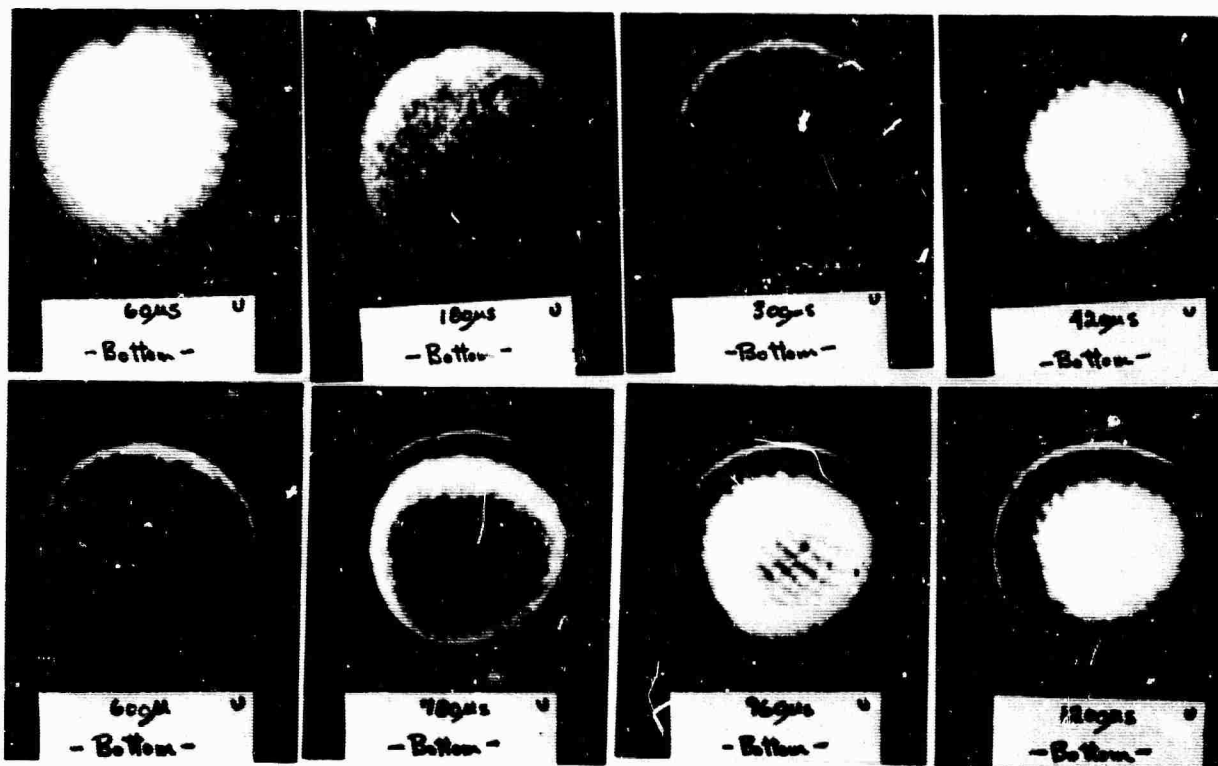


Figure 1-8. Mach-Zehnder Fringe Pattern Photographs for Rod AO-3 at 11,500j Pump Energy

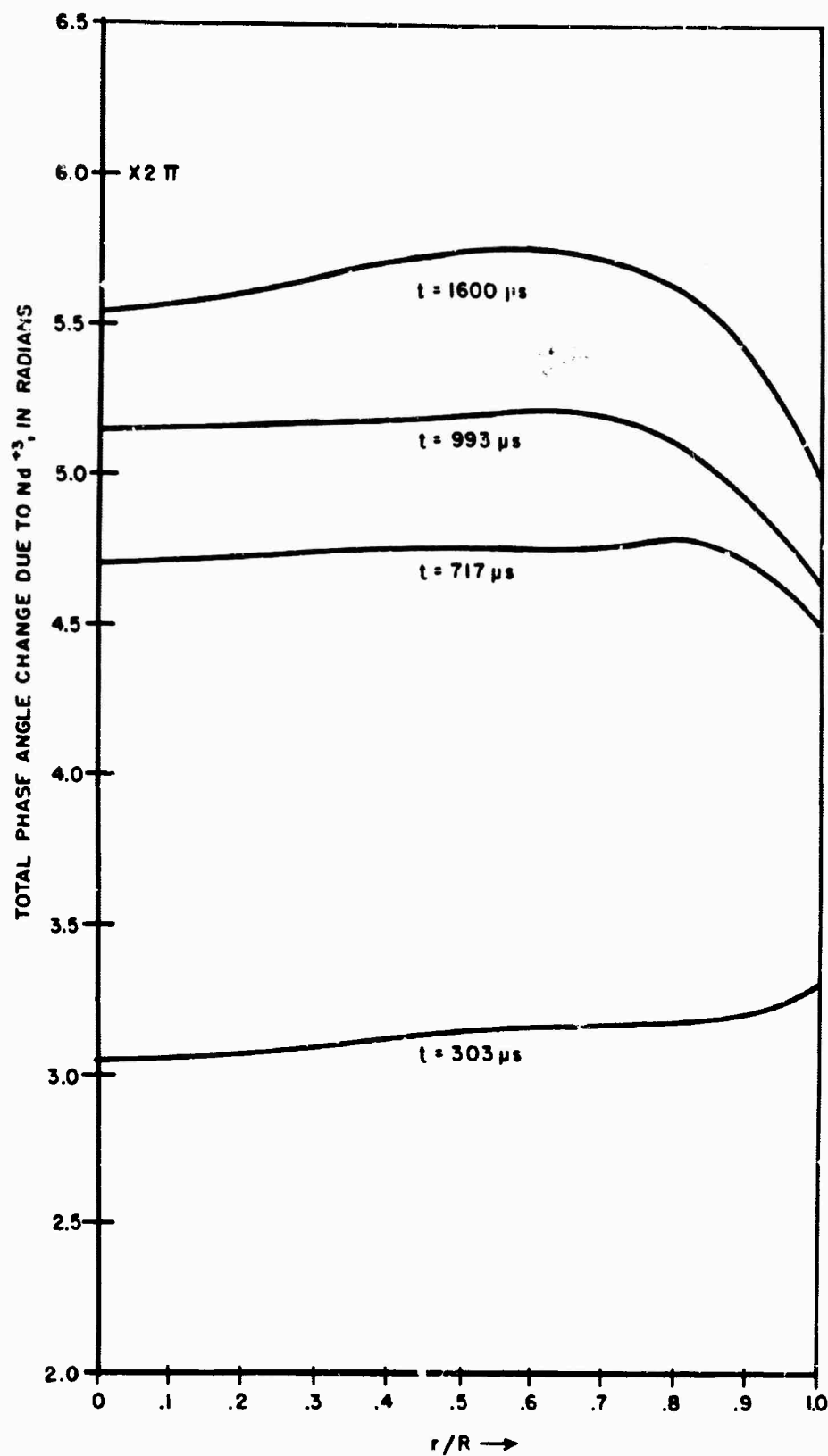


Figure 1-9. Total Change in Phase Angle attributed to Nd^{+3} in Rod AO-2 at 11,500j Pump Energy

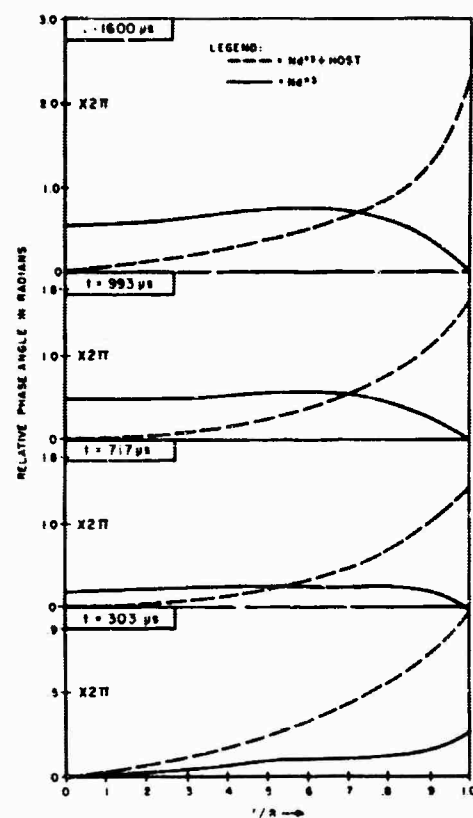


Figure 1-10. Comparison Between Radial Optical Path Change Due to Nd^{+3} and Nd^{+3} Plus Host in Rod AO-2 at 11,500j Pump Energy.

only is compared with that for Nd^{+3} plus the host. It is obvious that elimination of host absorption would noticeably reduce the optical distortion.

3. Birefringence Measurements

To assess depolarization effects and to acquire the necessary quantitative data to use in Section III to calculate the temperature rise in laser rod AO-2, the pump-induced birefringence was measured. The experimental arrangement for measuring the time resolved birefringence is shown in figure 1-11. Figure 1-12 shows selected photographs in the time development of the birefringence in rod AO-2 at 11,500 joules. As in case of the Mach-Zehnder photographs end B of the laser rod was focused at the focal plane of the camera. The film used, development procedure, film calibration data, framing speed, and frame exposure was essentially identical to that used for the Mach-Zehnder measurements. The equation used to calculate the phase angle between the radial and tangential polarization components was equation (A. 1)*. We shall call this the stress phase angle. The stress phase angle for an azimuthal angle θ of 45 degrees is shown as a function of normalized radius and time in figure 1-13 for a pump

*Appendix A

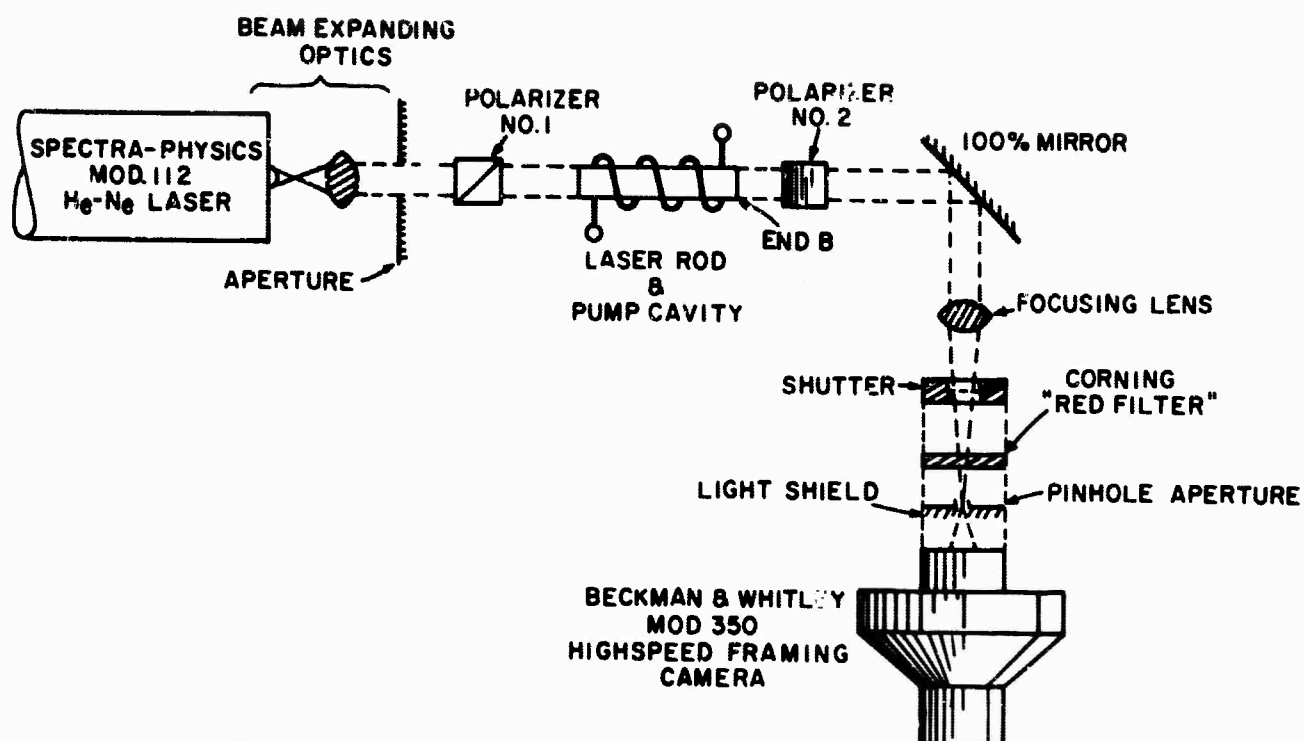


Figure 1-11. Experimental Diagram: Measurement of Pump Induced Birefringence.

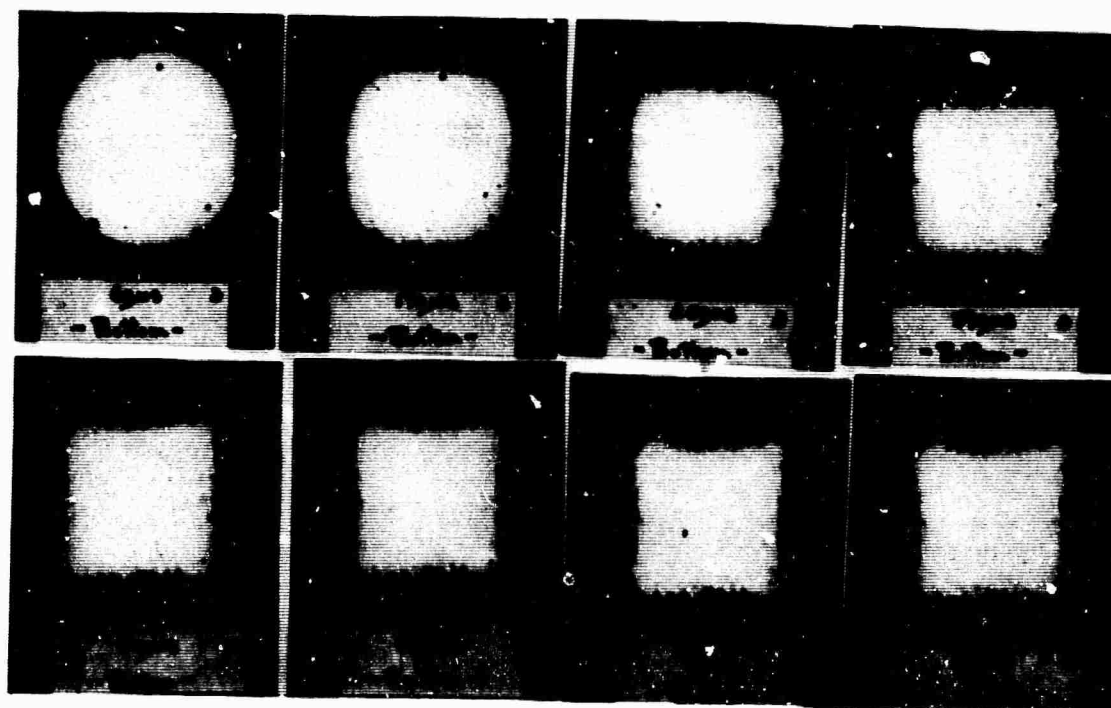


Figure 1-12. Stress Development in Rod AO-2 at 11,500j Pump Energy
(Direction of incident polarization $45^\circ \vec{E}$)

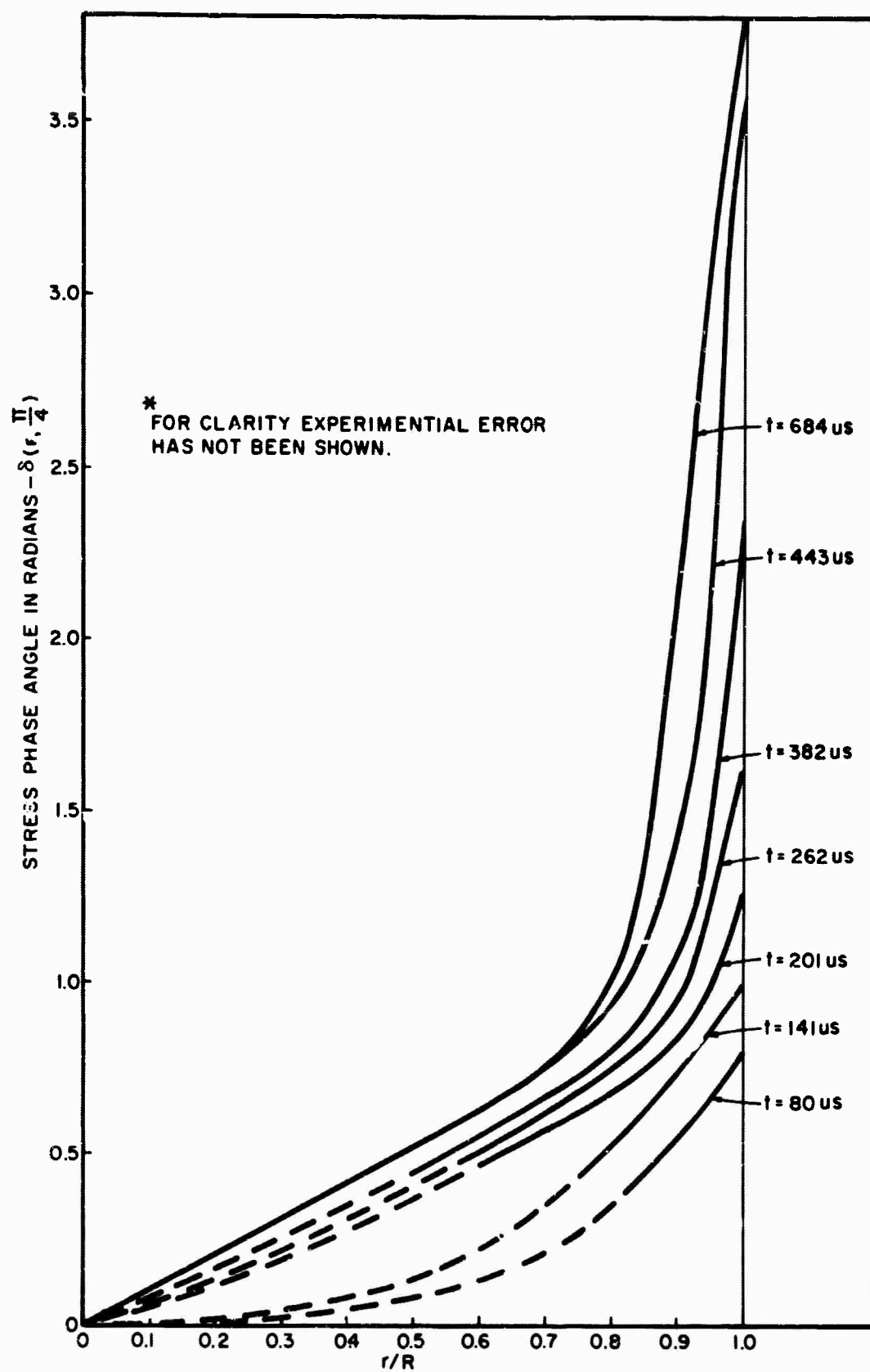


Figure 1-13. Radial Stress Angle in Rod AO-2 at 11,500j Pump Energy

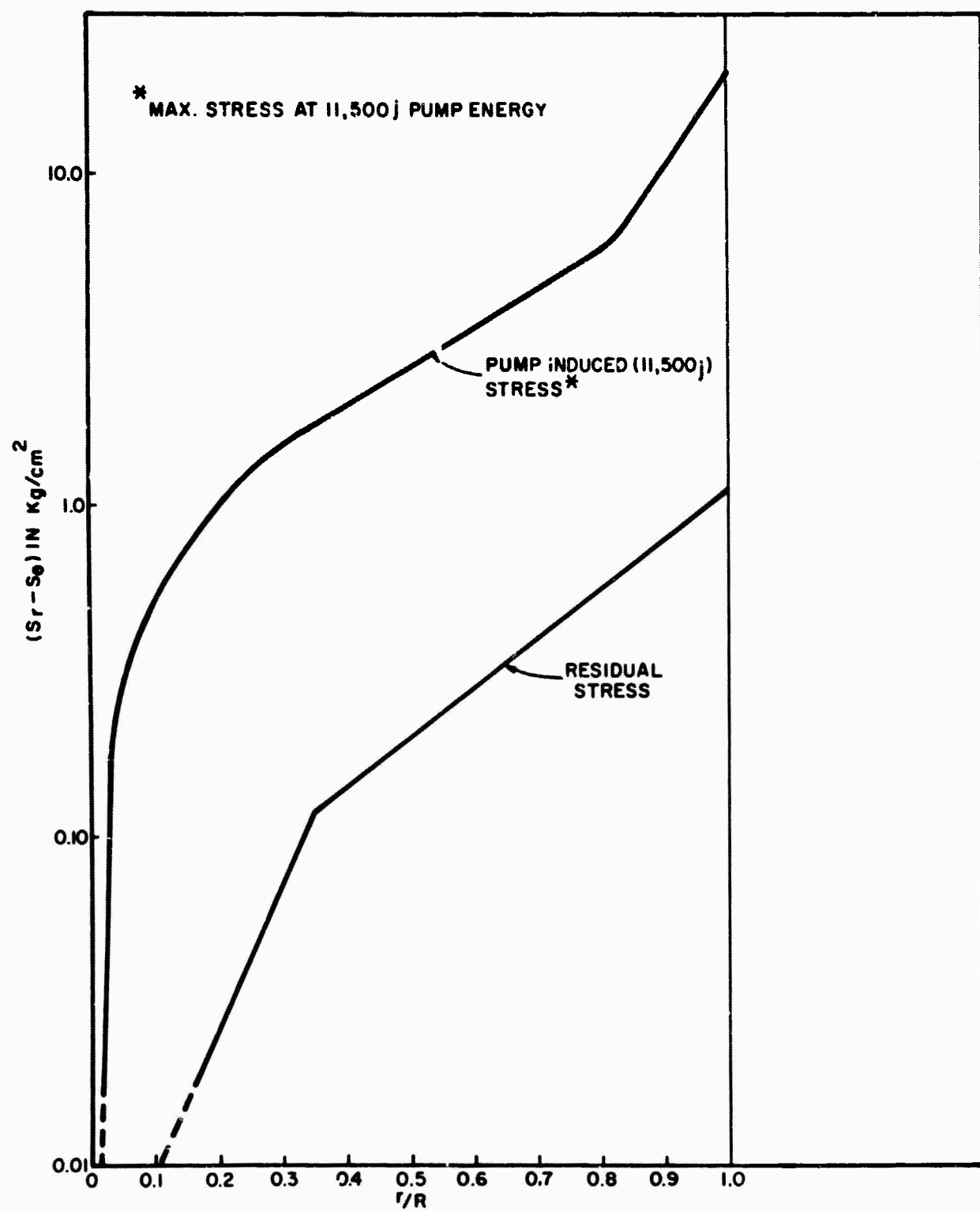


Figure 1-14. Comparison Between Residual and Pump Induced Stress in Rod AO-2

energy of 11,500 joules. Within experimental error (not shown in figure 1-13) there was no change in the stress phase angle between $t = 684$ microseconds and $t = 1600$ microseconds. The mean value of the data, however, indicated that the stress phase angle decreased slightly after 800 μ seconds.

To illustrate the degree of stress induced by the pump in rod AO-2 at 11,500 joules, the stress ($S_r - S_o$) before the pump, and at its peak value during the pump, was calculated from the data and equation (A.3)*. This is shown in figure 1-14. As can be seen from this curve, the pump-induced stress is better than an order of magnitude greater than the residual stress.

The undoped laser rod AO-3 was also tested for birefringence during the pump cycle. Although no quantitative data was extracted from the photographs, there was little qualitative difference between the birefringence patterns for rods AO-2 and AO-3.

4. Change in Length and Refractive Index

The experimental technique used in this part of the work allowed us to determine not only the change in physical length, but also the degree of physical distortion in the flatness of the rod ends and the change in refractive index.²

The laser rod was aligned with the He-Ne Beam, as in figure 1-15, so that the ends of the rod formed an interferometer. End B of the laser rod was imaged on a target in front of a photomultiplier tube. Directly in front of the photocathode surface was a .05-inch diameter pinhole.** The position of the target and P. M. tube was changed to establish a value of r/R and data was taken at each position. The movement of fringes past the pinhole was recorded during the pumping cycle for the "rod-end" interferometer. By using the data obtained with the "rod-end" and Mach-Zehnder interferometers, the change in length $\{\Delta l(t)\}$ and change in index $\{\Delta n(t)\}$ for the laser rod could be calculated as follows.

Consider the diagram of a Mach-Zehnder interferometer shown in figure 1-16. The phase differential between paths $L_1 + L_2$ and $L_3 + L_4$ prior to the pump cycle is given by:

$$(1.7) \quad \delta \phi_1 = \frac{2\pi}{\lambda} \left[\left\{ (x_1 + x_2) + l_o n_o + L_2 \right\} - (L_3 + L_4) \right]$$

However,

$$(1.8) \quad x_1 + x_2 + l_o = L_1.$$

*Appendix A

**Pinhole much smaller than fringe width

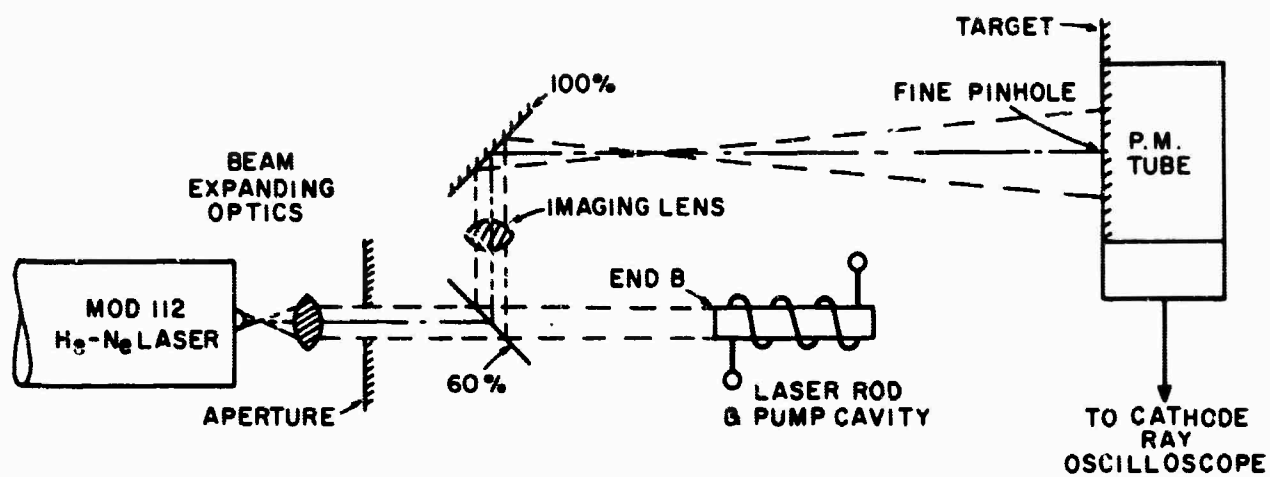


Figure 1-15. Experimental Diagram: "Rod End" Interferometer

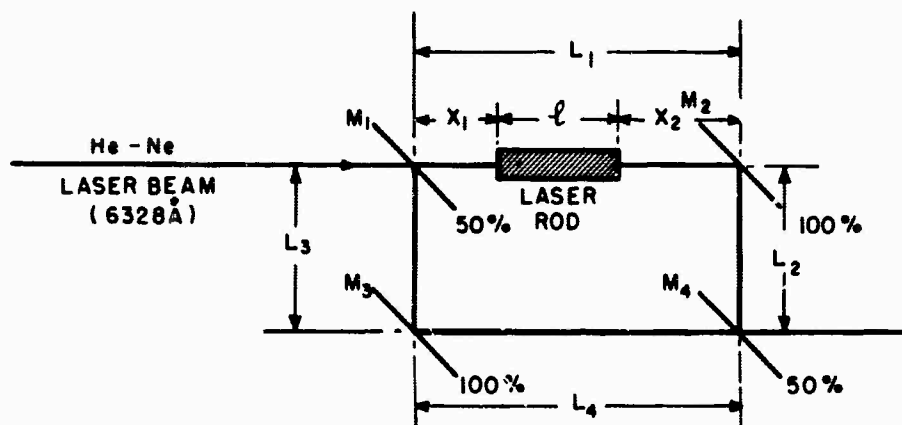


Figure 1-16. Mach-Zehnder Interferometer

Thus:

$$(1.9) \quad \delta \phi_1 = \frac{2\pi}{\lambda} \left[l_0(n_0-1) + (L_1+L_2) - (L_3+L_4) \right]$$

During the pump, equation (1.7) is modified such that

$$(1.10) \quad \delta \phi_2 = \frac{2\pi}{\lambda} \left[x_1' + x_2' + \{l_0 + \Delta l(t)\} \{n_0 + \Delta n(t)\} + L_2 - (L_3+L_4) \right]$$

Again,

$$(1.11) \quad x_1' + x_2' + [l_0 + \Delta l(t)] = L_1.$$

Thus:

$$(1.12) \quad \delta \phi_2 = \frac{2\pi}{\lambda} \left[\{l_0 + \Delta l(t)\} \{n_0 + \Delta n(t) - 1\} + (L_1+L_2) - (L_3+L_4) \right]$$

The difference between equations (1.9) and (1.12) gives the actual phase variations observed during the pump cycle. Thus,

$$(1.13) \quad \Delta \phi_1(t) = \frac{2\pi}{\lambda} \left[\Delta n(t) \{l_0 + \Delta l(t)\} + \Delta l(t) \{n_0 - 1\} \right]$$

Since $l_0 \gg \Delta l(t)$, equation (1.13) becomes

$$(1.14) \quad \Delta \phi_1(t) = \frac{2\pi}{\lambda} \left[l_0 \Delta n(t) + (n_0 - 1) \Delta l(t) \right].$$

Next, consider the "rod-end" interferometer as shown in figure 1-17. Prior to pumping, the phase difference between rays traversing the path OA \rightarrow AO and those reflected directly from M_1 is given by:

$$(1.15) \quad \delta \phi_3 = \frac{4\pi}{\lambda} (l_0 n_0).$$

During the pump cycle the phase difference is given by

$$(1.16) \quad \delta \phi_4(t) = \frac{4\pi}{\lambda} \{l_0 + \Delta l(t)\} \{n_0 + \Delta n(t)\}.$$

Again, $l_0 \gg \Delta l(t)$, and the observed phase change during pumping is given by the difference

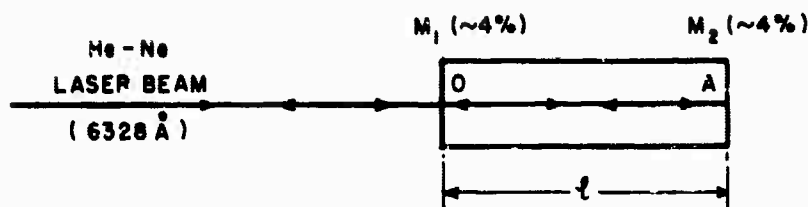


Figure 1-17. "Rod - End" Interferometer

between (1.15) and (1.16). This phase change is

$$(1.17) \quad \Delta \phi_2(t) = \frac{4\pi}{\lambda} \left[l_0 \Delta n(t) + n_0 \Delta l(t) \right].$$

Equations (1.14) and (1.17) can be used to solve for $\Delta n(t)$ and $\Delta l(t)$.

These solutions are:

$$(1.18) \quad \Delta l(t) = \frac{\lambda}{4\pi} \left[\frac{1}{2} \phi_2(t) - \phi_1(t) \right],$$

$$(1.19) \quad \Delta n(t) = \frac{\lambda}{4\pi l_0} \left[n_0 \Delta \phi_1(t) - \frac{1}{2}(n_0 - 1) \Delta \phi_2(t) \right].$$

Thus, by recording $\Delta \phi_1(t)$ and $\Delta \phi_2(t)$ at a fixed value of r/R , the change in physical length and refractive index can be determined.

Figure 1-18 shows the phase change obtained at $r/R = 0$ for the Mach-Zehnder and "rod-end" interferometers at 6400, 8800, and 11,500 joules pump energy. In spite of the large number of fringes recorded for the "rod-end" interferometer, the data was found to be extremely reproducible from shot to shot. Figure 1-19 shows $\Delta l(t)$ as obtained from this data, while figure 1-20 shows $\Delta n(t)$.

The value of $\Delta l(t)$ was also obtained at 11,500 joules for $r/R = .44$ and $r/R = .72$. This was done to determine whether any physical distortions to the ends of the laser rod occurred during the pump cycle. A plot of $\Delta l(t)$ at $r/R = 0$, $.44$, and $.72$ is shown in figure 1-21. Within experimental error there was no change in end flatness from $r/R = 0$ to $r/R = .72$ up to $t = 1.1$ milliseconds. After $t = 1.1$ ms there is still no distortion between $r/R = 0$ and $r/R = .44$, but distortion definitely does exist between $r/R = .44$ and $r/R = .72$. At 1.6 ms this distortion in end flatness has increased (between $r/R = 0$ and $.72$) to approximately $1/4 \lambda$ per end. Ignoring all internal refractive index gradients, this distortion alone will cause the laser rod to act like a negative lens.

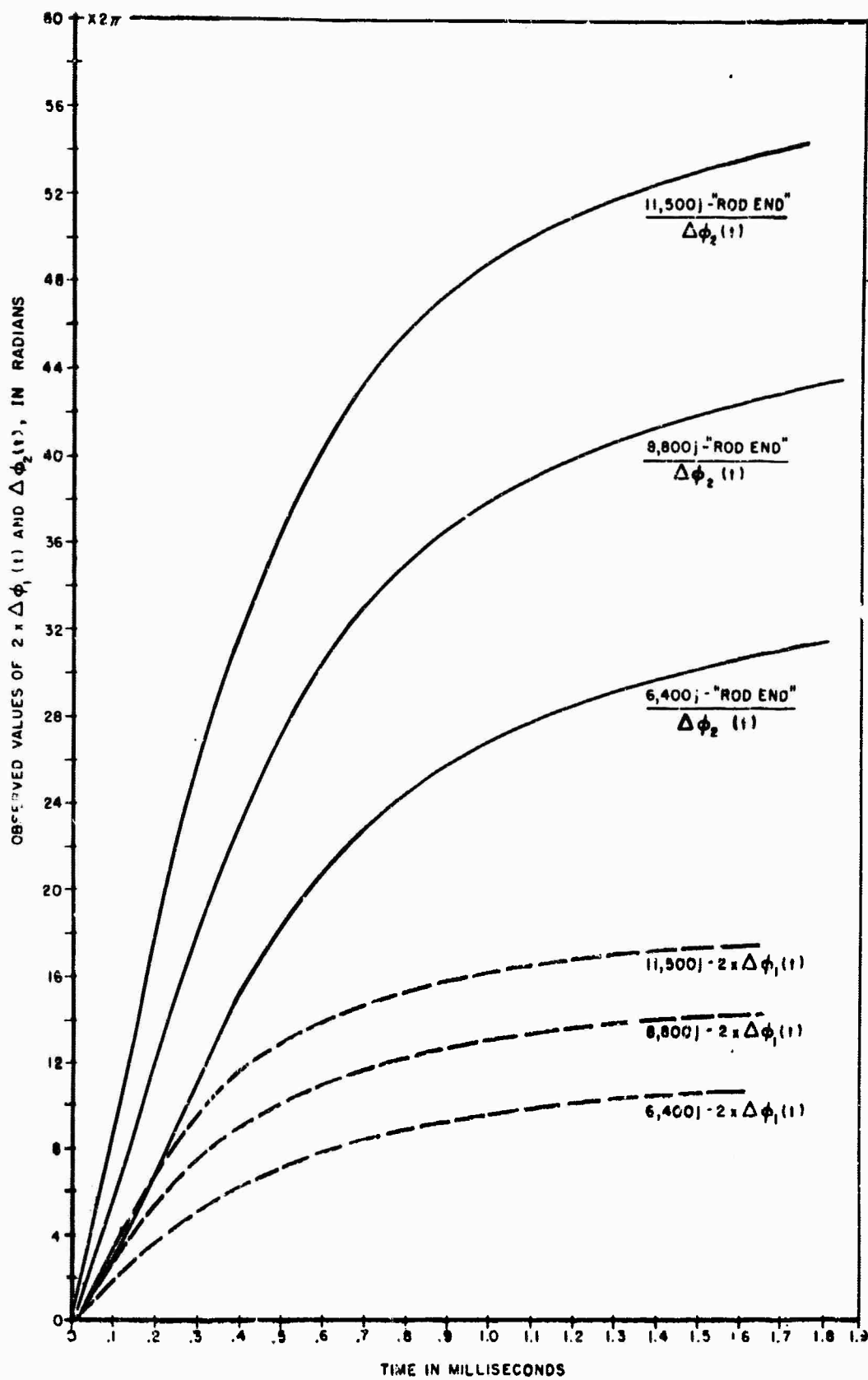


Figure 1-18. $2 \times \Delta_1\theta(t)$ and $\Delta\theta_2(t)$ vs. Time at $r/R = 0$, for "Rod-End" and Mach-Zehnder Interferometer at 6400, 8800, and 11,500 joule Pump Energies

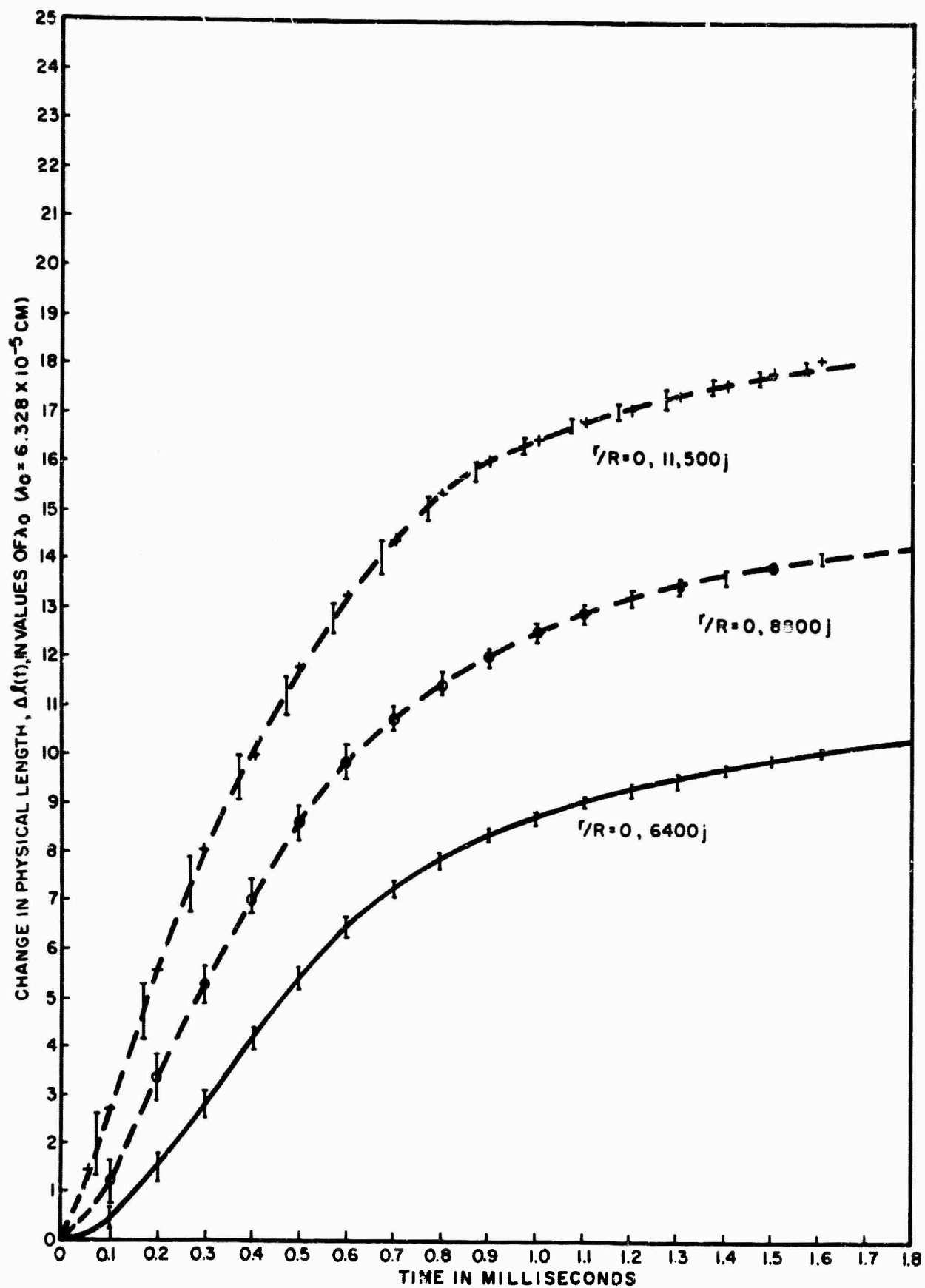


Figure 1-19. Change in Physical Length for Rod AO-2 vs Time at 6400, 8800, and 11,500j Pump Energies

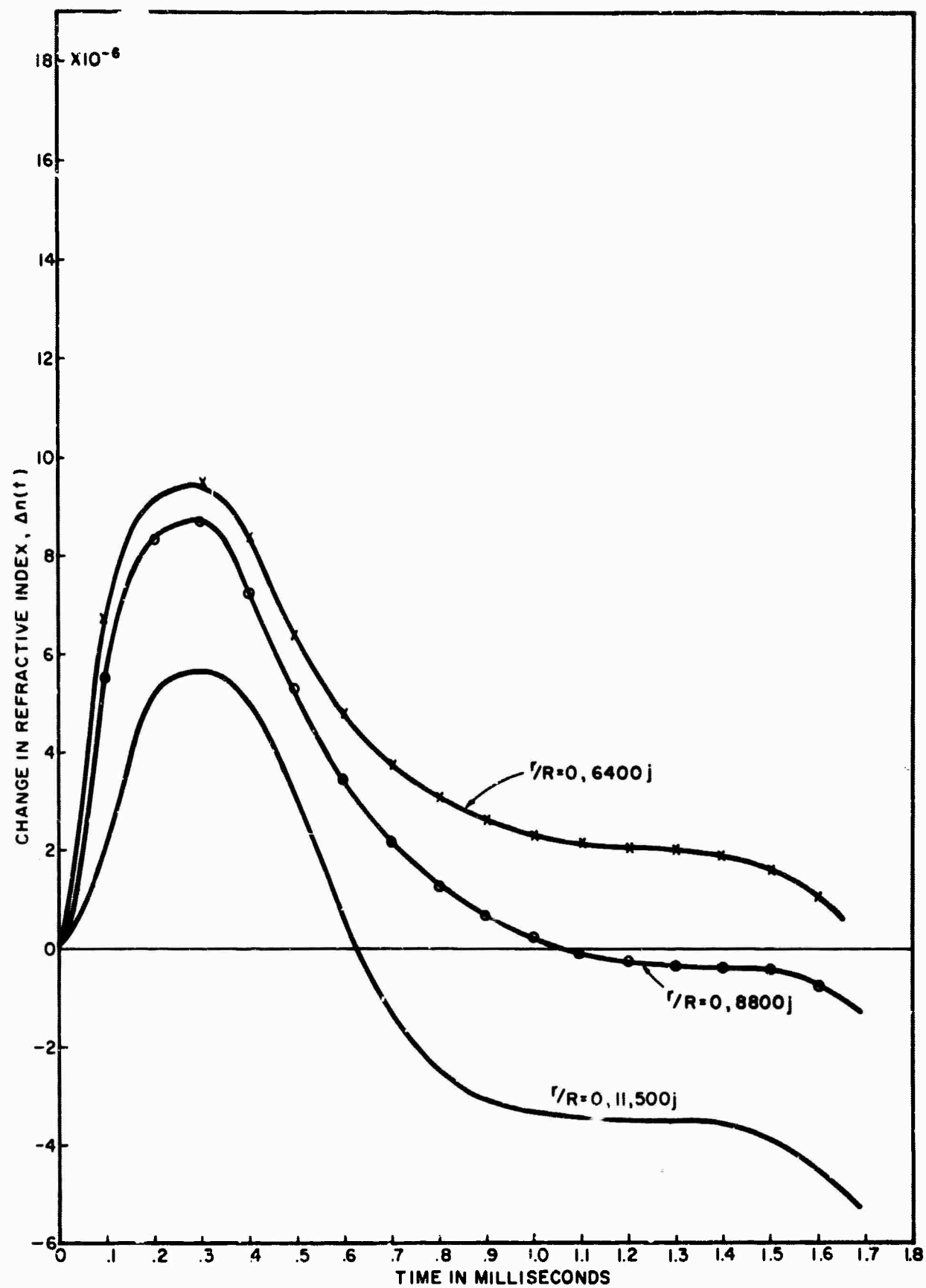


Figure 1-20. Refractive Index Change (experimental Error not shown) vs Time for AOLux Rod AO-2 at $r/R=0$, and 6400, 8900, 11,500j Pump Energies

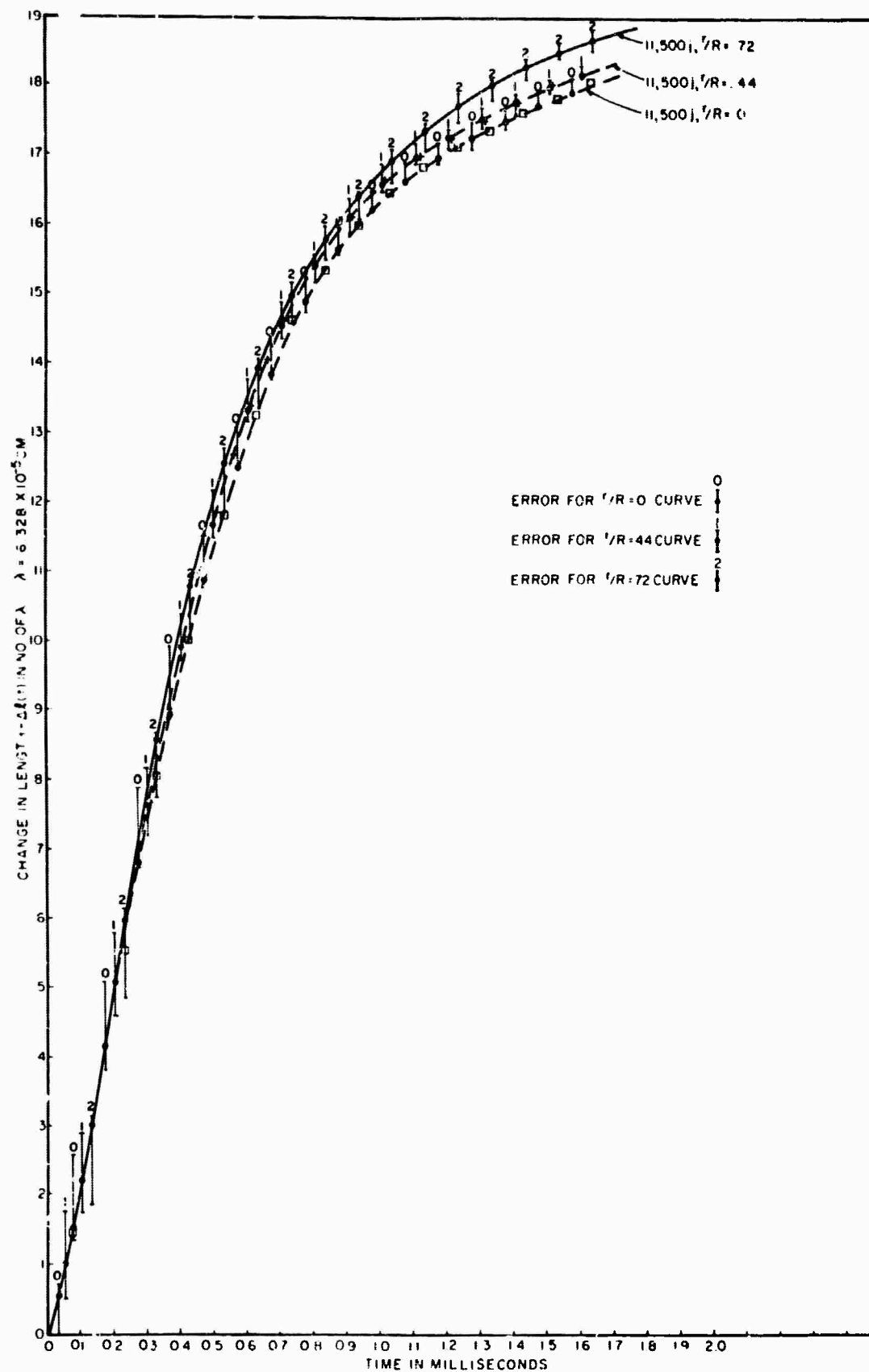


Figure 1-21. Change in Physical Length for Rod AO-2 at 11,500j Pump Energy and for $r/R = 0$, $r/R = .44$, $F/R = .72$

5. Thermocouple Temperature Rise Determination

To obtain an experimental check on the calculated temperature rise of the laser rod, a thermocouple was used to measure the temperature rise after the pump cycle was terminated. A .1 inch diameter hole .5 inch deep was drilled in the center of the end of rod AO-1. A thermocouple was inserted into this hole and contacted the glass. Initially, a low thermal mass thermocouple, manufactured by RdF Corporation, was placed in the laser rod. It was hoped that accurate temperature rise data could be obtained at least after 10 milliseconds. Unfortunately, the thin (.0003 inch thick) RdF thermocouple evaporated when exposed to the pump radiation. A new thermocouple was constructed, from .01" diameter chromel-alumel wire, and tested. This unit withstood repeated flashes at 11,500 joules. The time after the flash that was required to obtain the temperature rise in the rod was approximately 20 seconds with this new unit. The time of 20 seconds might at first seem too long for meaningful data to be obtained. However, for glass with its low thermal conductivity, the temperature rise recorded at 20 seconds should be a reasonable approximation to the equalized temperature rise in the rod.

Consider an infinite length cylinder at a uniform temperature T_0 . If the temperature at the outside surface is suddenly increased and held at a temperature T_1 , a certain length of time will be required for the cylinder to assume a uniform temperature. By defining a time constant τ_t as the time required for the temperature at the center of the rod to rise to 63% of its final value, the value of τ_t is given by³

$$(1.20) \quad \tau_t = .26 \frac{\gamma c R^2}{K_c}$$

where γ is the density, c the specific heat, K_c the thermal conductivity, and R the radius of the cylinder. For rod AO-2 and AO-1 the value of τ_t is 12 seconds. Although the idealized case illustrated above is not strictly true for an optically pumped laser rod, particularly since the outside of the rod is not constrained at a fixed temperature, the value of the rod temperature 20 seconds after the flash should be a close approximation to the equalized temperature rise in the rod induced by the pump. Additional experimental verification of this assumption is found in the fact that the temperature rise recorded by the thermocouple remained constant within 1°C from 15 seconds to at least 1 minute after the flash.

Correlation between the equalized rod temperature and that calculated theoretically from birefringence and change in physical length data can be obtained by integrating under the calculated temperature distribution curve at the end of the pump cycle (1600 microseconds) to obtain the total heat absorbed by the rod. This heat deposited uniformly in the laser rod

should result in approximately the same temperature rise as measured by the thermocouple. It is to be expected that the temperature measured by the thermocouple may be slightly higher than that predicted by the heat content of the rod at the end of the pump cycle. This additional temperature rise occurs by absorption of heat from the hot flash lamp and other components within the cavity after the flash. The temperature rise measured by the thermocouple as a function of pump energy is shown in figure 1-22.

6. Small Diameter Light Beam Deflection

The theory to be presented in Section II predicts the refraction suffered by a light ray within the rod. To determine the validity of this prediction, an experiment was set up to measure the deflection of a small diameter light beam for various values of r/R . The experimental arrangement is shown in figure 1-23.

After passing the probe beam through the laser rod at a fixed value of r/R , the far field pattern of the probe beam was photographed by the high-speed camera. The angle the probe beam makes after emerging from the rod with the direction of the probe beam before it enters the rod is converted to a translational movement of the far field image in the focal plane of the camera. Figure 1-24 shows this angle of the probe beam as a function of time, recorded for rod AO-2 at 11,500 joules pump. The angle of the probe beam was always zero for $r/R = 0$. In addition, as r/R was increased, the probe beam angle increased in the direction of bending the probe beam away from the rod axis. Both of these characteristics are in quantitative agreement with the theory as will be shown in Section III.

7. Mach-Zehnder Optical Path Length Variation with Nonex Sheath

All quantitative measurements of thermal-optic distortion were made with a Pyrex sheath surrounding the laser rod. During the course of these measurements it was found that the large optical path length gradients across the rod diameter were largely caused by absorption of pump radiation by the glass host. It has been postulated that absorption of U. V. radiation, passing through the Pyrex sheath, is responsible. It was also shown that if the host absorption could be eliminated, the resulting optical path gradients would be substantially reduced. To confirm this the frosted pyrex sheath was replaced by a frosted Nonex sheath (Corning Code No. 7720 glass). The short wavelength cutoff of Nonex is much closer to the visible than that of standard Pyrex and was expected to decrease the amount of energy absorbed by the host.

Unfortunately, direct comparison of the effects of the two glasses could not be made. This was due to the fact that the standard size of the Nonex in stock was different from the pyrex. The pyrex tube had a .06" wall thickness with a .98" i. d. while the Nonex had a .09"

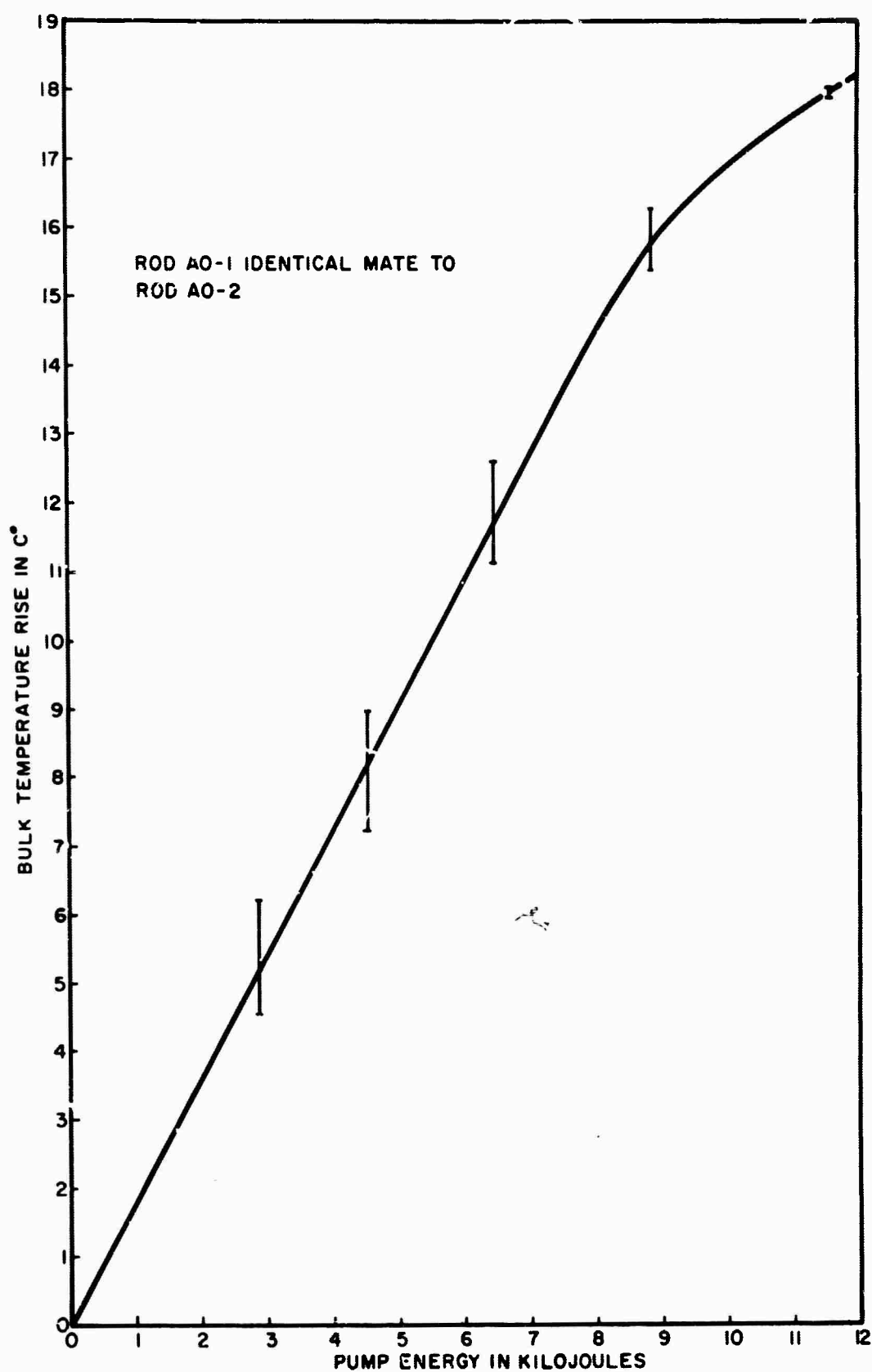


Figure 1-22. Bulk Temperature Rise in Rod AO-1* as a Function of Pump Energy

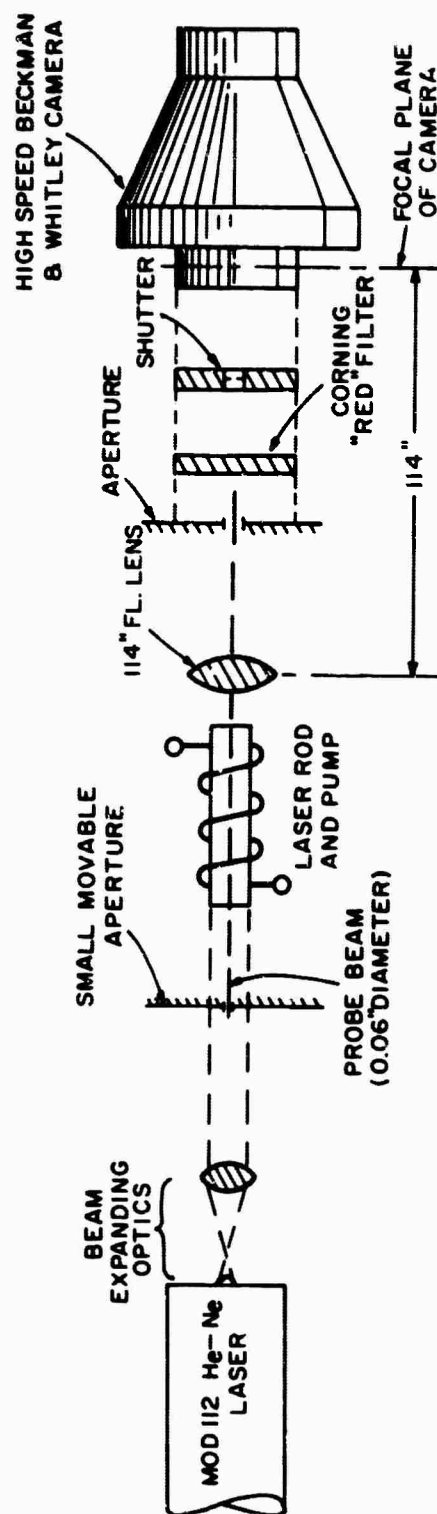


Figure 1-23. Experimental Diagram: Measurement of Light Beam Deflection

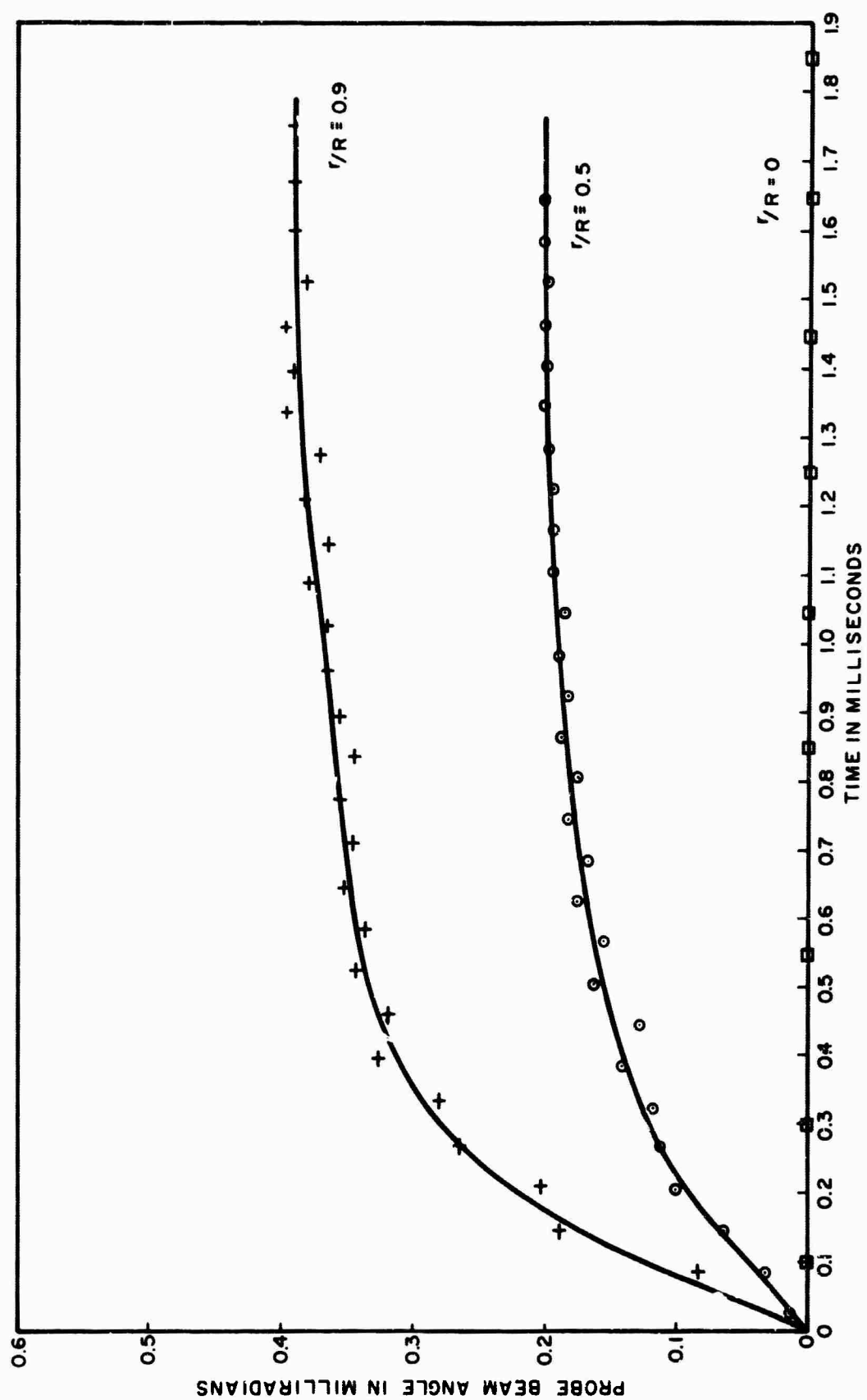


Figure 1-24. Plot of Probe Beam Angle vs. Time for Rod AO-2 at 11,500 Joules Pump Energy

wall thickness with a .84" i. d. Pictures were obtained of the optical path distortion with the Nonex sheath at a pump energy of 11,500 joules. By comparing these with those in figure 1-3(c) it was found that the optical path length gradients were less for the Nonex sheath.

8. Measurement of α_n

The term α_n^* is defined as $\frac{1}{n_0} \frac{\Delta n}{\Delta T}$, where n_0 is the refractive index of the glass and $\frac{\Delta n}{\Delta T}$ is the total change in the index due to uniform temperature rise. It was found necessary to measure α_n since its value at 6328 Å was not available. The value of α_n was determined by uniformly increasing the temperature of the laser rod over a range ΔT , determining the change in optical path length which occurred, and subtracting the effect of rod expansion from the observed path length change.

The experimental approach was to place a thermocouple in contact with the surface of rod AO-2. The rod was then wrapped with a layer of asbestos cloth leaving the ends exposed. Approximately twenty windings of nichrome wire were wound around the inner layer of cloth and covered by a second wrapping of asbestos cloth. This thermally insulated assembly was placed in a cardboard container, considerably larger than the rod, which was located in one arm of a Mach-Zehnder interferometer. As the temperature of the rod changed, the fringe shift at the center of the rod was counted by means of a photomultiplier connected to a recorder. The experimental arrangement is illustrated in figure 1-25. The rod was first allowed to stabilize at room temperature. Then, current was applied to the nichrome winding, and the rod allowed to stabilize at its final temperature. The value of $\frac{\Delta n}{\Delta T}$ was then calculated from

$$(24) \quad \frac{\Delta n}{\Delta T} = \frac{N \lambda}{l_0 \Delta T} - (n_0 - 1) \alpha$$

where N was the number of fringes which passed the center of the rod, λ the He-Ne wavelength, l_0 the length of the rod, ΔT the temperature rise, n_0 the refractive index, and α the expansion coefficient. The range of ΔT was held to approximately 20° C for each experimental run. The value of α_n at 6328 Å was found to be $-1.25 \pm .66 \times 10^{-6}$ per °C. Most of the uncertainty in this figure arises from the uncertainty in the value of α . (See Appendix F.)

*See Section II

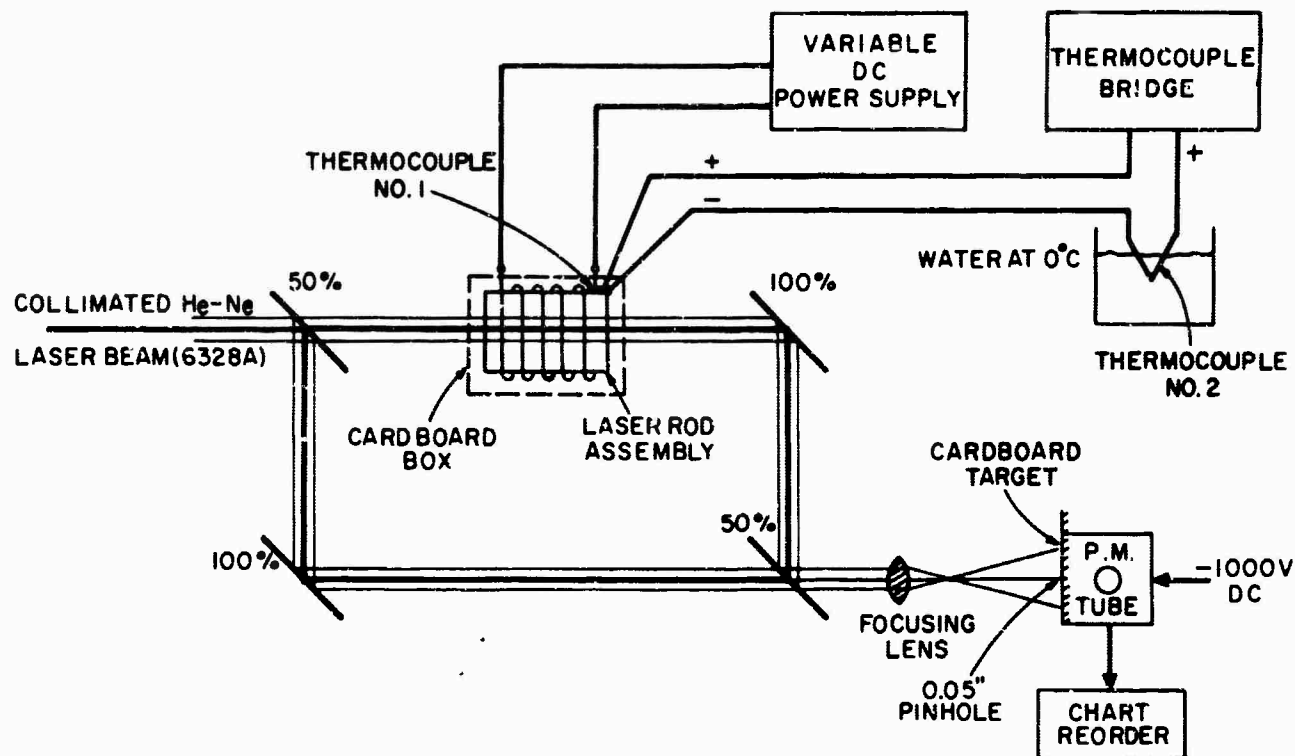


Figure 1-25. Experimental Diagram: Measurement of α_n

9. Conclusions

The most important results obtained from the experiments described in this section are in the form of reproducible data which could be used to obtain correlation between theory and experiment. This will be done in Section III.

There are, however, important observations which give a better qualitative understanding of the optical properties of American Optical AOlux glass laser rods when exposed to an intense pumping source. For clarity, these will be listed below in outline form as they refer to each experiment.

- 1) Operating Range of Laser Rod - Rod AO-2 exhibited considerable gain at 11,500 joules pump energy.
- 2) Total Phase Angle Change
 - a) The total phase angle change at the center of the rod increased at a rate proportional to the total pump energy deposited in the rod up to the time of observation.
 - b) The relative phase angle across the rod diameter is primarily due to host absorption.
- 3) Birefringence Measurements
 - a) Within experimental error the pump-induced stress phase angle reached a steady

state approximately 700 microseconds after the start of the pump cycle.

- b) The pump-induced stress differential ($S_p - S_0$) was better than an order of magnitude greater than the residual stress differential.
- 4) Change in Physical Length and Refractive Index - Physical distortion to the flatness of the rod ends (dishing) is evident for times greater than 1 millisecond, and for values of r/R greater than .5.
- 5) Thermocouple Temperature Rise Determination - Equalized temperature rise in the laser rod was approximately 18°C at 11,500 joules pump energy, 16° at 8,000 joules, and 12°C at 6400 joules.
- 6) Small Diameter Probe Beam Deflection
- a) There was no deflection of the probe beam when passed through the center of the rod ($r/R = 0$). As the probe was moved in the direction of increasing r/R , probe beam angle increased to a maximum value (for 11,500 joules input) of .4 milliradian at $r/R = .90$ and $t = 1600$ microseconds.
- b) The probe beam was bent away from the axis of the rod as was predicted by the Mach-Zehnder interferometer fringe patterns. These show that the optical path length increases as r increases.
- 7) Measurement of α_n - The measured value of α_n at 6328 Å was $1.25 \pm .66 \times 10^{-6} \text{ } ^\circ\text{C}^{-1}$.

D. REFERENCES - SECTION I

1. Born & Wolf, Principles of Optics, Pergamon Press (1959), pg. 258
2. A. Y. Cabezas, L. G. Komai, and R. P. Treat, Appl. Optics, Vol. 5, No. 4, April, 1966, pg. 647
3. H. S. Carslaw & J. C. Jaeger, Conduction of Heat in Solids, Oxford University Press (1959), pg. 200

II. THEORETICAL CONSIDERATIONS

A. INTRODUCTION

Thermal optical distortion in isotropic laser materials such as glass stems from temperature gradients which arise as a result of energy dissipated as heat in the material.^{1, 2, 3, 4} Two separate types of optical distortions arise from such temperature gradients. The first is caused by a non-zero index of refraction change with temperature of the material. The second is caused by a change in index of refraction of the material with stress which in turn arises from temperature gradients within the material. Both of these effects are important in most glasses. The neglect of the stress optical effect in American Optical 3835 glass (AOlux) leads, for example, to the prediction that a glass rod of this material will act as a positive lens when the temperature increases from the center of the rod outward while, in fact, it acts as a negative lens.

In the following analysis the distortion suffered by an initially plane wave in passing through a glass rod of radius R and length L will be considered for the case where the temperature of the rod is a function only of the radial coordinate r and the time t . This will be done by obtaining the equation for the ray trajectories (or paths) by requiring that Fermat's principle be satisfied and then computing the optical path length along these ray paths. These results will then be used to predict the results of a Mach-Zehnder interferometer experiment, a birefringence experiment, and the refraction suffered by a small diameter light beam in passing through the rod. The latter will lead to the formulation of an expression for an average beam divergence angle for laser amplifiers.

In Section III of this report, it will be demonstrated that this theoretical description is in quantitative agreement with the experimental results described in the first section.

B. RAY TRAJECTORIES

Suppose a plane wave traveling parallel to the axis of a rod of length L and radius R falls on one end of the rod as shown in figure 2-1. We define light rays in the usual way⁵ as the orthogonal trajectories to the geometrical wave-fronts. For clarity, the wave-fronts have been omitted within the rod. We first ask what are the equations of these trajectories. Consider a ray which enters the rod at point P_0 at a radial distance from the axis of the

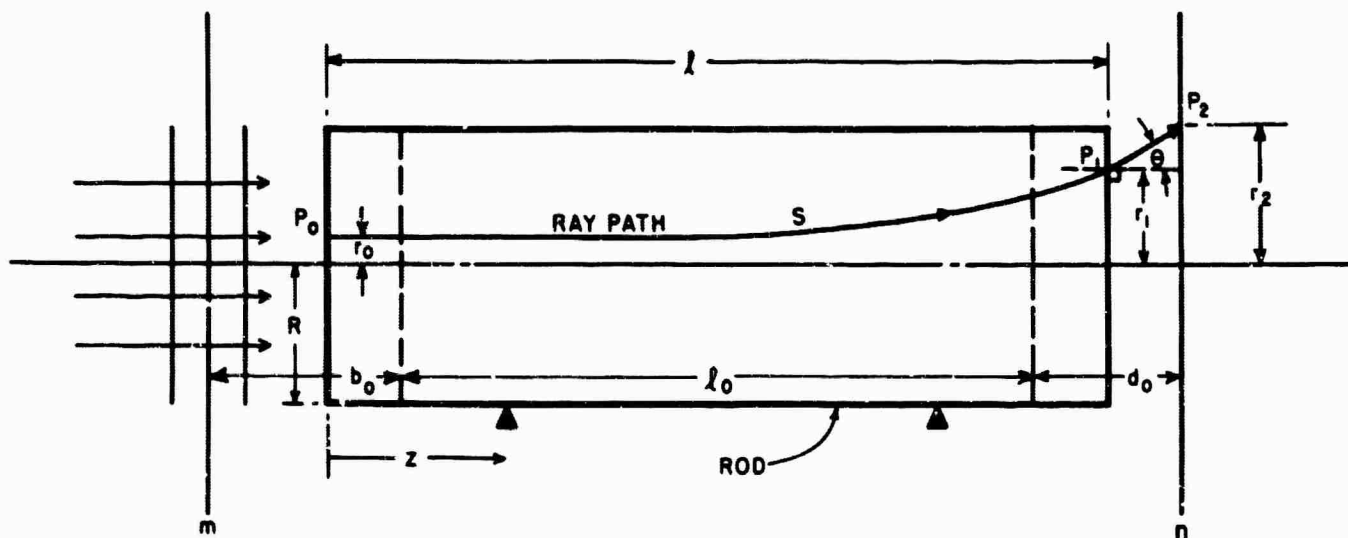


Figure 2-1. Ray Path Geometry

rod $r = r_0$, travels through the rod and emerges from the rod at point P_1 at radius r_1 and at angle θ with respect to the normal to the rod at P_1 as shown.

The optical path length S along this ray between P_0 and P_1 is

$$(II.1) \quad S = \int_0^{z_1} n(r) \sqrt{1 + r'^2} \, dz$$

where $n(r)$ is the index of refraction at r , and the prime denotes differentiation once with respect to z . Fermat's principle⁶ now requires that S be a minimum (i.e., that a solution be found for the variational problem $\delta S = 0$). The mathematical formulation for this problem is well known. In our case the solution is the solution to Euler's differential equation

$$(II.2) \quad \frac{\partial F}{\partial r} - \frac{d}{dz} \left(\frac{\partial F}{\partial r'} \right) = 0$$

where F is $n(r) \sqrt{1 + r'^2}$. Using this function for F we obtain from equation (II. 2)

$$(II.3) \quad (1 + r'^2)^2 \frac{dn(r)}{dr} - n(r) (1 + r'^2) r'' + n(r) r'^2 r'' = 0$$

Now let $r' \equiv p$ and $\frac{d^2 r}{dz^2} \equiv r'' = p \frac{dp}{dr}$. We then find from (II. 3)

$$(II. 4) \quad n(r) p \frac{dp}{dr} - (1 + p^2)^2 \frac{dn(r)}{dr} = 0$$

Integrating once yields

$$(II. 5) \quad -1/2 \frac{1}{(1 + p^2)} = \ln [C_1 n(r)]$$

where C_1 is a constant and must be determined by the boundary condition that $dr/dz = p$ is zero at $r = r_0$. The C_1 is found from equation (II. 5) to be

$$(II. 6) \quad C_1 = \frac{1}{n(r_0) \sqrt{e}}$$

From (II. 5) and (II. 6) we find that the slope of the ray is

$$(II. 7) \quad \frac{dr}{dz} = \pm \sqrt{\frac{-\ln \left[\frac{n(r)}{n(r_0)} \right]}{\ln \left[\frac{n(r)}{n(r_0) \sqrt{e}} \right]}}$$

where the positive sign in front of the square root is used when $dn(r)/dr \geq 0$, and the negative sign when $dn(r)/dr < 0$.*

To obtain the equation for the ray path, equation (II. 7) must be integrated.

Rearranging and integrating we have

$$(II. 8) \quad \pm \int \sqrt{\frac{1}{2 \ln \left[\frac{n(r)}{n(r_0)} \right]} - 1} dr = z + C_2$$

where C_2 is a constant to be evaluated by the boundary condition that when $z = 0$, $r = r_0$.

Before the left-hand side of (II. 8) can be evaluated we must assume an explicit function for $n(r)/n(r_0)$ over only the range of values of r covered by the ray which enters at $r = r_0$. We choose the function to be

$$(II. 9) \quad n(r)/n(r_0) = e^{a(r-r_0)}$$

where a is chosen to be $\dot{n}(r_0)/n(r_0)$ and where the dot denotes differentiation once by r . This choice of a makes the first two terms of the power series expansion of $e^{a(r-r_0)}$ identical with the first two terms of the power series expansion of $n(r)/n(r_0)$ about r_0 . The use of equation (II. 9) will be justified so long as the range of values of r covered by a ray which enters the rod at r_0 and leaves at r_1 is smaller than the range of r for which the exponential is a good

* Here $n(r)$ is assumed to be either monotonically increasing or decreasing throughout the range r_0 to r_1 inclusive.

fit to $n(r)/n(r_0)$. This condition is satisfied even under the most intense pumping conditions of AOLux rods described in this report because of the small values of $r_1 - r_0$ and the slowly varying character of $n(r)$. Although this condition should always be checked before the theory is applied, it is expected to hold in all cases for glass rods where the optical pumping conditions are such that the temperature depends only on the radial coordinate and the pumping is fairly uniform.

Inserting (II.9) into (II.8), integrating and evaluating C_2 to be zero by the boundary condition, yields

$$(II.10) \quad \pm \frac{1}{2a} \left\{ \sqrt{2a(r-r_0)} \sqrt{1-2a(r-r_0)} + \sin^{-1} \sqrt{2a(r-r_0)} \right\} = z$$

as the required equation for the ray path. We note that since for glass the index change is 10^{-5} or less per degree temperature change, we have

$$(II.11) \quad 2a(r-r_0) \approx \frac{2}{n} \frac{\Delta n}{\Delta r} \Delta r < 10^{-4}$$

for all practicable pumping conditions of glass rods. In view of (II.11) we may write an approximate form of (II.10) which will be adequate for our purposes:

$$(II.12) \quad r - r_0 = \frac{az^2}{2}.$$

C. OPTICAL PATH LENGTH

Now that the equation for the ray path through the material is known, we are in a position to evaluate the optical path length S . This is given by equation (II.1) provided that the integration is carried out along the ray path. We therefore rewrite equation (II.1) using equations (II.5) and (II.6). The result is

$$(II.13) \quad S = \int_{r_0}^{r_1} \frac{n(r) dr}{\sqrt{2 \ln [n(r)/n(r_0)]}}$$

where r_1 is the value of r at P_1 in figure 2-1. With the aid of equation (II.9) and the variable change

$$(II.14) \quad y^2 = 2a(r-r_0)$$

equation (II. 13) may be written as

$$(II. 15) \quad S = \frac{\sqrt{2} \, n(r_o)}{a} \int_0^{\sqrt{a(r_1-r_o)}} e^{y^2} dy$$

or

$$(II. 16) \quad S = \frac{n(r_o) \sqrt{2a(r_1-r_o)}}{a} \left[1 + 1/3 a(r_1-r_o) + \text{terms of order } \{a(r_1-r_o)\}^2 \right].$$

Using equation (II. 12) and noting that $z_1 \equiv \ell \equiv \ell_o (1 + \epsilon_{zz})$ where ℓ_o is the length of the rod before pumping begins and ϵ_{zz} is the strain in the z direction, equation (II. 16) becomes

$$(II. 17) \quad S = n(r_o) \ell_o (1 + \epsilon_{zz}) \left\{ 1 + 1/6 \left[\frac{\dot{n}(r_o) \ell_o}{n(r_o)} \right]^2 \right\}$$

where the terms of higher order in (II. 16) have been dropped. If we require S to be correct to $\lambda/10$ we may calculate the largest value of ℓ_o for which the last term in (II. 17) may be neglected. The condition is

$$(II. 18) \quad n(r_o) \ell_o (1/6) \left[\frac{\dot{n}(r_o) \ell_o}{n(r_o)} \right]^2 = \frac{\lambda}{10}$$

A typical value of $\dot{n}(r_o)$ which we obtained experimentally in pumping AOLux glass rods is $5 \times 10^{-5} \text{ cm}^{-1}$. We find the value of ℓ_o from (II. 18) with $n(r_o) = 1.5$ and $\lambda = 6.3 \times 10^{-5} \text{ cm}$ to be about 28 cm. Therefore under these conditions, the last term in (II. 17) is important in determining S for rods longer than 28 cm. The last term arises from the fact that the ray paths through the rod are not straight lines. If straight lines are assumed for the ray paths⁷, only the first term in (II. 17) appears. The inclusion of Fermat's principle in the theory is therefore important in computing optical path length differences between different rays through the rod at least under some conditions. In addition, the refraction suffered by a pencil of rays in traversing even the 3-inch long rods used for this report cannot be predicted by considering only straight rays. In fact, as will be shown later in this section, the slope of the ray already given in general terms by equation (II. 7) will lead to an equation for the average beam-divergence angle to be expected for glass-laser amplifiers.

D. MACH-ZEHNDER ANALYSIS

In figure 2-1, the optical path length at radius r_2 between plane m and n before the material is heated, i. e., at time $t = 0$, is

$$(II. 19) \quad P(r_2, 0) = b_0 + n_0 l_0 + d_0$$

where n_0 is the initial index of refraction of the material. At some time t after the heating begins, the path length is

$$(II. 20) \quad P(r_2, t) = S + b_0 - \epsilon_{zz} l_0/2 + (d_0 - \epsilon_{zz} l_0/2)/\cos \theta$$

The change in path length $\Delta P(r, t)$ which exists at time t is therefore

$$(II. 21) \quad \Delta P(r_2, t) = S - n_0 l_0 - l_0 \epsilon_{zz} (1 + \sec \theta)/2 - d_0 (1 - \sec \theta).$$

We now assume that the temperature rise, T , of the rod is a function only of the radial coordinate r and the time t . We set $T = 0$ at $t = 0$. For an isotropic material with no externally applied stresses the stress-strain relations under these conditions are⁸

$$(II. 22) \quad \sigma_{rr}(r, t) = \beta \left[\frac{1}{R^2} \int_0^R T(r, t) r \, dr - \frac{1}{r^2} \int_0^r T(r, t) r \, dr \right]$$

$$(II. 23) \quad \sigma_{\theta\theta}(r, t) = \beta \left[\frac{1}{R^2} \int_0^R T(r, t) r \, dr + \frac{1}{r^2} \int_0^r T(r, t) r \, dr - T(r, t) \right]$$

$$(II. 24) \quad \sigma_{zz}(r, t) = \beta \left[\frac{2}{R^2} \int_0^R T(r, t) r \, dr - T(r, t) \right]$$

$$(II. 25) \quad \epsilon_{zz}(r, t) = (2\alpha/R^2) \int_0^R T(r, t) r \, dr$$

where $\beta = \alpha E / (1 - \nu)$, α is the linear thermal expansion coefficient, E Young's modulus, and ν Poisson's ratio. These equations give the correct stress-strain values for a temperature $T(r, t)$ which is changing slowly enough so that in a time interval equal to the characteristic mechanical time $t_M = d/v_e$ it changes by an amount which is small compared to the total temperature rise at the beginning of the interval.^{9, 10} Here d is a

characteristic dimension of the material and v_e the longitudinal sound wave velocity. Since v_e for glass is about 6×10^5 cm/sec, t_M is about 10^{-6} seconds for 3/8-inch diameter rods. For the pumping conditions employed in this report, the rod temperature rises about 15°C in 10^{-3} second or only about 0.015°C in 10^{-6} seconds. We expect therefore that after about the first 10μ seconds after the beginning of the pump pulse equations (II. 22) through (II. 25) should be valid for the experimental conditions studied in this report.

The indices of refraction for light polarized perpendicular and parallel to the direction of stress are in general different. The propagation of light in a rod stressed as in equations (II. 22) through (II. 25) must therefore be described by the indices of refraction at a given radius r and time t . The index for light polarized parallel to the radial direction $n_r(r, t)$ and that for light polarized perpendicular to this, i. e., parallel to the θ direction $n_\theta(r, t)$ may be written as

$$(II. 26) \quad n_r(r, t) = n_0 + \left. \frac{dn}{dT} T \right|_r$$

$$(II. 27) \quad n_\theta(r, t) = n_0 + \left. \frac{dn}{dT} T \right|_\theta$$

where

$$(II. 28) \quad \left. \frac{dn}{dT} T \right|_r = \left. \frac{\partial n}{\partial T} T \right|_{\sigma=0} + \left. \frac{\partial n}{\partial \sigma_{//}} \sigma_{rr} \right|_{T=0} + \left. \frac{\partial n}{\partial \sigma_{\perp}} (\sigma_{\theta\theta} + \sigma_{zz}) \right|_{T=0}$$

and

$$(II. 29) \quad \left. \frac{dn}{dT} T \right|_\theta = \left. \frac{\partial n}{\partial T} T \right|_{\sigma=0} + \left. \frac{\partial n}{\partial \sigma_{//}} \sigma_{\theta\theta} \right|_{T=0} + \left. \frac{\partial n}{\partial \sigma_{\perp}} (\sigma_{rr} + \sigma_{zz}) \right|_{T=0}$$

and where the temperature rise $T = T(r, t)$ is assumed small compared to the temperature of the rod at $t = 0$. Here $\left. \frac{\partial n}{\partial T} \right|_{\sigma=0}$ is defined as the change in index with respect to temperature at constant stress equal to zero, $\left. \frac{\partial n}{\partial \sigma_{//}} \right|_{T=0}$ as the change in index with respect to a change in stress at constant temperature where the change in stress is directed parallel to the direction of polarization, and $\left. \frac{\partial n}{\partial \sigma_{\perp}} \right|_{T=0}$ as the change in index with respect to a change in stress at constant temperature where the change in stress is directed perpendicular to the direction of polarization. Using the definitions

$$(II. 30) \quad \left. \frac{\partial n}{\partial T} \right|_{\sigma=0} \equiv n_0 \alpha_n$$

$$(II. 31) \quad \left. \frac{\partial n}{\partial \sigma_{||}} \right|_{T=0} = -B_{||}$$

$$(II. 32) \quad \left. \frac{\partial n}{\partial \sigma_{\perp}} \right|_{T=0} = -B_{\perp}$$

and equations (II. 22), (II. 23), and (II. 24), the indices may be written as

$$(II. 33) \quad n_r(r, t) = n_o + [n_o \alpha_n + 2B_{\perp} \beta] T(r, t) + \beta(B_{||} - B_{\perp}) \frac{1}{r^2} \int_0^r T(r, t) r dr$$

$$- \beta(3B_{\perp} + B_{||}) \frac{1}{R^2} \int_0^R T(r, t) r dr$$

$$(II. 34) \quad n_{\theta}(r, t) = n_o + [n_o \alpha_n + \beta(B_{||} + B_{\perp})] T(r, t) + \beta(B_{\perp} - B_{||}) \frac{1}{r^2} \int_0^r T(r, t) r dr$$

$$- \beta(3B_{\perp} + B_{||}) \frac{1}{R^2} \int_0^R T(r, t) r dr$$

This result was first obtained by Quell⁷.

With the determination of the two refractive indices given by equations (II. 33) and (II. 34), we are now in a position to develop equation (II. 21) for both directions of polarization. We note first that the tangent to the ray at P_1 in figure 2-1 inside the rod has slope $\left. \frac{dr}{dz} \right|_{r=r_1} = \gamma(r_1, t)$. For the radial polarization we have $\theta \equiv \theta_r(r_{1r}, t)$ and

$$(II. 35) \quad n_r(r_{1r}, t) \sin \gamma_r(r_{1r}, t) = n_{air} \sin \theta_r(r_{1r}, t)$$

where r_1 for radial polarization becomes $r_{1r} \equiv r_{1r}(r_o, t)$. Using equations (II. 7), (II. 9), and (II. 12) and setting $n_{air} = 1$, for small angles equation (II. 35) becomes

$$(II. 36) \quad \theta_r(r_{1r}, t) = \gamma_o \dot{n}_r(r_o, t) .$$

Expanding the sec θ for small angles, equation (II. 21) becomes with the aid of (II. 36) and (II. 17)

$$(II. 37) \quad \Delta P_r(r_{2r}, t) = \ell_0 \left\{ (n_0 - 1) \epsilon_{zz} + n_r(r_0, t) - n_0 + \frac{\ell_0^2}{6n_0} \left[1 + 3n_0 d_0 / \ell_0 \right] \dot{n}_r^2(r_0, t) \right\}.$$

From figure 2-1, r_2 the radius of the ray at P_2 is

$$(II. 38) \quad r_2 = r_0 + r_1 - r_0 + (d_0 - \epsilon_{zz}/2) \tan \theta.$$

For the radial polarization, r_2 is defined as $r_{2r} \equiv r_{2r}(r_0, t)$. We have with the aid of equations (II. 36 and (II. 12)

$$(II. 39) \quad r_{2r}(r_0, t) = r_c + \left[\frac{\ell_0}{2n_0} + d_0 \right] \ell_0 \dot{n}_r(r_0, t).$$

For light polarized in the θ direction equations (II. 36), (II. 37) and (II. 39) become

$$(II. 40) \quad \theta(r_{1\theta}, t) = \ell_0 \dot{n}_\theta(r_0, t),$$

$$(II. 41) \quad \Delta P_\theta(r_{2\theta}, t) = \ell_0 \left\{ (n_0 - 1) \epsilon_{zz} + n_\theta(r_0, t) - n_0 + \frac{\ell_0^2}{6n_0} \left[1 + 3n_0 d_0 / \ell_0 \right] \dot{n}_\theta^2(r_0, t) \right\}$$

and

$$(II. 42) \quad r_{2\theta}(r_0, t) = r_0 + \left[\frac{\ell_0}{2n_0} + d_0 \right] \ell_0 \dot{n}_\theta(r_0, t).$$

E. BIREFRINGENCE EXPERIMENT ANALYSIS

If we wish to know the difference in path length between radially and tangentially polarized rays at the point P_1 in figure 2-1, we cannot simply subtract equation (II. 41) from equation (II. 37). The reason for this is that if both rays enter the rod at the same point at radius r_0 they leave the rod at different radii r_{1r} and $r_{1\theta}$ given by equations (II. 39) and (II. 42) respectively (d_0 set equal to zero). Therefore, to find the path length difference at point $r_{1\theta}$ between radially and tangentially polarized rays, $\Delta P_{r\theta}(r_{1\theta}, t)$, we must compute the path length difference between a radially polarized ray which enters the rod at $r = r_m$ and emerges at $r = r_{1\theta}$ and a tangentially polarized ray which enters at $r = r_0$ and emerges at $r = r_{1\theta}$. That is, we must find

$$(II. 43) \quad \Delta P_{r\theta}(r_{1\theta}, t) = \Delta P_r(r_{1\theta}, t) - \Delta P_\theta(r_{1\theta}, t).$$

We have

$$(II.44) \quad \Delta P_r(r_{1\theta}, t) \approx \Delta P_r(r_{1r}, t) - \left\{ \frac{c}{dr} \Delta P_r(r, t) \right\} \bigg|_{r=r_{1r}} \Delta r_{1r\theta}$$

where

$$(II.45) \quad \Delta r_{1r\theta} \equiv r_{1r} - r_{1\theta} = \frac{l_o^2}{2n_o} [\dot{n}_r(r_o, t) - \dot{n}_\theta(r_o, t)].$$

Inserting (II.44) and (II.45) into (II.43) and using equations (II.37) and (II.41) with d_o set equal to zero yields

$$(II.46) \quad \Delta P_{r\theta}(r_{1\theta}, t) = l_o \left\{ n_r(r_o, t) - n_\theta(r_o, t) + \frac{l_o^2}{8n_o} [\dot{n}_r^2(r_o, t) - \dot{n}_\theta^2(r_o, t)] \right. \\ \left. - \frac{l_o^2}{2n_o} \ddot{n}_r(r_o, t) \left[1 + \frac{l_o^2}{3} \ddot{n}_r(r_o, t) \right] [\dot{n}_r(r_o, t) - \dot{n}_\theta(r_o, t)] \right\}$$

where the double dot denotes differentiation twice with respect to r and where from (II.42)

$$(II.47) \quad r_{1\theta} \equiv r_{1\theta}(r_o, t) = r_o + \frac{l_o^2}{2n_o} \dot{n}_\theta(r_o, t).$$

F. SMALL DIAMETER BEAM REFRACTION AND AMPLIFIER BEAM DIVERGENCE ANGLE

Equation (II.36) gives the angle at which a radially polarized ray emerges from the rod (see figure 2-1). In the next section we use this equation to calculate the angle at which a radially polarized beam 1.5mm in diameter emerges from the rod. We find good agreement with experiment. It seems reasonable therefore to use equation (II.36) to compute an average beam divergence angle $\bar{\theta}_r(r, t)$ for a radially polarized beam of diameter $2r$ on propagating once through a rod. The beam is assumed to be concentric with the longitudinal rod axis. We have

$$(II.48) \quad \bar{\theta}_r(r, t) = \frac{\int_0^r 2\pi r_o \theta_r(r_{1r}, t) G_r(r_o, t) I_r(r_o, t) dr_o}{\int_0^r 2\pi r_o G_r(r_o, t) I_r(r_o, t) dr_o}$$

where $G_r(r_o, t)$ is the single pass rod gain at r_o and t , and $I_r(r_o, t)$ the intensity of the input beam at r_o . Using equation (II. 36) we have

$$(II. 49) \quad \bar{\theta}_r(r, t) = \frac{\lambda_o \int_0^r r_o \dot{n}_r(r_o, t) G_r(r_o, t) I_r(r_o, t) dr_o}{\int_0^r r_o G_r(r_o, t) I_r(r_o, t) dr_o}$$

A similar equation holds for $\bar{\theta}_\theta(r, t)$ and is obtained from (II. 49) by replacing the subscript r by θ . It should be noted that equation (II. 49) neglects diffraction effects and therefore holds only when $\bar{\theta}_r(r, t) \gg \frac{\lambda}{2r}$, i.e., only when the beam divergence is considerably larger than expected from diffraction effects alone.

G. CONCLUSIONS

Inclusion of ray path geometry, in the derivation of the basic equations which predict the effects of thermo-optic distortion, not only increases the range of applicability of the theory but also leads to results which are not obtainable when only straight ray paths are considered. The deflection of a small diameter probe beam and an average beam divergence angle for laser amplifiers can be calculated directly when ray paths are included. In addition, for long laser rods and under certain experimental conditions for short rods, consideration of ray paths is absolutely necessary to predict the effects of thermal-optic distortion.

H. REFERENCES

1. H. Welling & C.J. Bickart, J. Opt. Soc. of America, Vol 56, No. 5, May 1966, pg.611
2. A.P. Veduta, A.M. Leontovich, & V.N. Smorchkov, Soviet Physics JETP, Vol. 21, No. 1, July 1965, pg.59
3. A.E. Blume & K.F. Tittel, Appl. Opt., Vol. 3, No. 4, April 1964, pg.527
4. S.P. Sims, A. Stein, & C. Roth, Appl. Opt., Vol. 5, No. 4, April 1966, pg. 621
5. M. Born & E. Wolf, Principles of Optics, The Macmillan Co., New York, (1964), pg.114
6. Reference 5, Pg.128
7. F.W. Quell, Jr., Appl. Opt., Vol.5, 1966, pg. 633

8. B.A. Boley & J.H. Weiner, Theory of Thermal Stresses, John Wiley & Sons, Inc. (1960), Sec. 9-10

9. Reference 1

10. Reference 8, pg. 51

III. COMPARISON OF THEORY WITH EXPERIMENT

A. INTRODUCTION

This section will be concerned with a quantitative comparison of the theoretical predictions of Section II with the experimental results presented in Section I. This comparison will be divided into two major parts. The first part will discuss only the radial dependence of the parameters. The second part will compare the experimental and theoretical results only at the center of the rod.

It will be seen that the agreement between theory and experiment for the radial dependence of the parameters is within experimental error. However, when the experimental value of the absolute magnitude of the change in index of refraction along the center of the rod is compared to the value expected from the theory in Section II, agreement does not exist within experimental error.

This discrepancy has led to an important new term which must be added to equations II. 33 and II. 34 for the change in refractive index. This term arises from the existence of an excited neodymium ion population. The theoretical and experimental evidence for the existence of this term is discussed.

B. COMPARISON OF THEORY WITH EXPERIMENT: RADIAL DEPENDENCE

To see if the theory can be correlated with experiment, we first find the temperature $T(r, t)$ by using the data given in figure 1-19 for the change in length $\Delta l(t)$ and the data given in figure 1-13 for the stress phase angle $\delta(r, \pi/4)$. The temperature is given by ¹

$$(III. 1) \quad T(r, t) = \frac{1}{B} F(r, t) - \frac{2}{BR^2} \int_0^R F(r, t) r dr + \frac{\Delta l(t)}{\alpha l_0}$$

where

$$(III. 2) \quad F(r, t) \equiv \Delta P_{r\theta}(r, t) + 2 \int_0^r \frac{\Delta P_{r\theta}(r, t) dr}{r}$$

and

$$(III.3) \quad B \equiv \frac{\alpha E \ell_0}{1-\gamma} \left[B_1 - B_{II} \right].$$

The path length difference between the radially and tangentially polarized components, $\Delta P_{r\theta}(r, t)$, is of course $\lambda/2\pi$ times the stress phase angle. We note that in the derivation of equation III.1, the rays through the rod have been considered to be straight lines. This is a good approximation for path length differences measured in the birefringence experiment since the rod length used in our experiments was only 3 inches (See the discussion following equation II.18 in Section II.). $T(r, t)$, as calculated from III.1, is shown in figure 3-1 for rod at 11,500 joules pump energy.

bulk temperature rise* can be obtained from the value of $T(r, t)$ at the end of the pump cycle (assuming no additional heat flows into or out of the rod after this time). The amount of heat deposited in the laser rod is given by

$$(III.4) \quad Q(t) = 2\pi \ell_0 C \gamma \int_0^R T(r, t) r dr$$

where $Q(t)$ is the heat deposited, C the specific heat, and γ the density. Since the bulk temperature rise is defined as that temperature the rod would assume if $Q(t)$ calories were deposited uniformly in the rod at the end of the pump pulse ($t \cong 1600$ microseconds), the bulk temperature rise (T_B) is given by

$$(III.5) \quad T_B = \frac{2}{R^2} \int_0^R T(r, 1600) r dr.$$

T_B was calculated to be $16.8 \pm 1.9^\circ\text{C}$ for rod AO-2 at 11,500 joules pump energy.** The temperature rise recorded by the thermocouple measurements in Section I.C.5 for the same experimented conditions was 18°C .

According to the theory presented in Section II, once the temperature is known all other parameters may be calculated. We proceed therefore to use the results shown in figure 3-1 to compute the change in refractive index $n_r(r, t) - n_0$, the probe beam angle $\theta_r(r, t)$, and the relative phase angle $\delta_r(r, t) - \delta_r(0, t)$. We then compare these results with the experimentally determined values given in Section I.

*See Section I.C.5

**Includes spread in experimental data for $\delta(r, \pi/4)$ and $\Delta \ell(t)$ plus spread in material constants (see Appendix F).

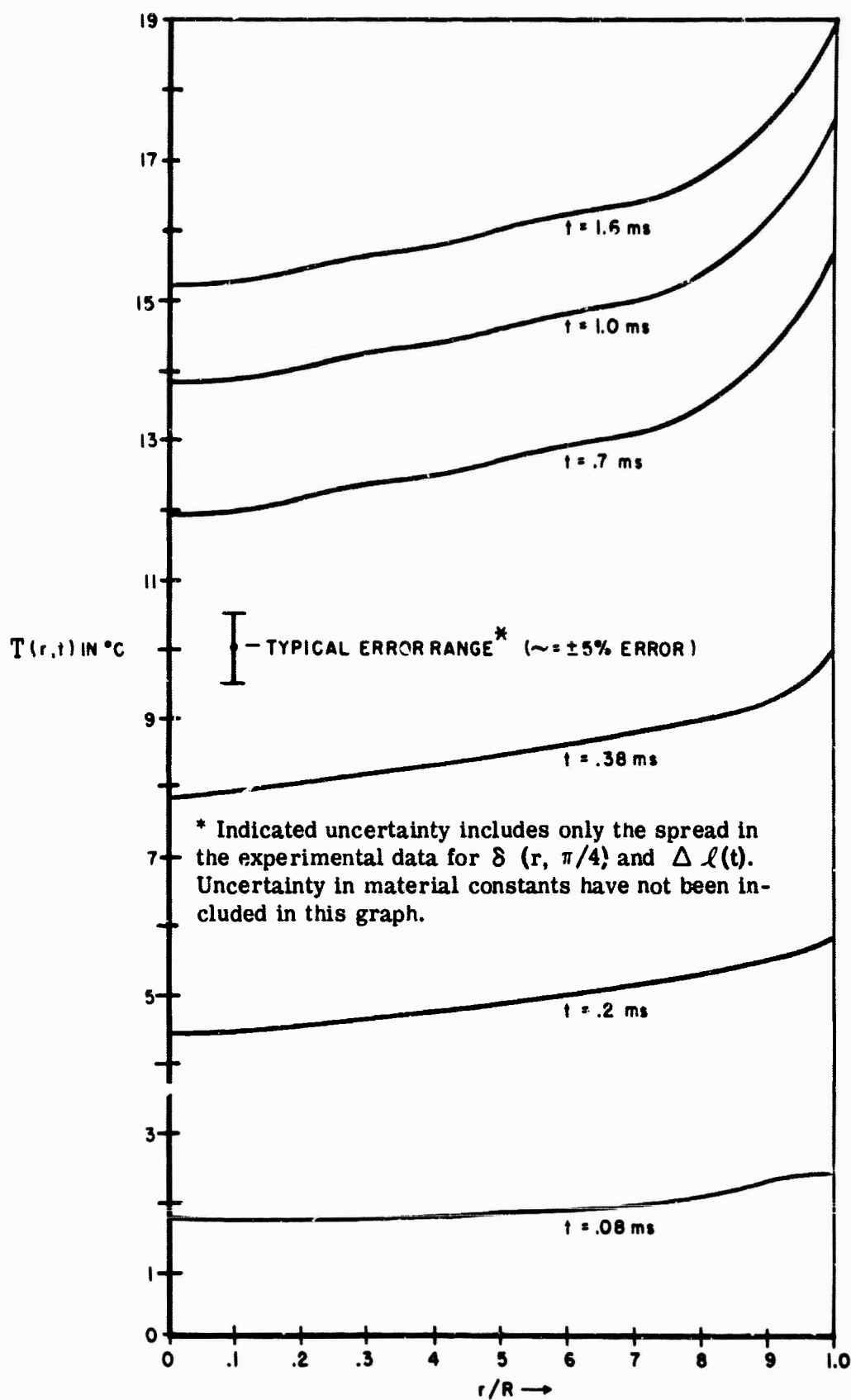


Figure 3-1. Calculated Value of the Temperature Rise, $T(r,t)$ for Rod AO-2 at 11,500j Pump Energy

Using equation II. 33 with $n_o \alpha_n = -2.14 \times 10^{-6}/^\circ\text{C}$, we find the results shown in figure 3-2 for the change in refractive index for radially polarized radiation at two representative times. We note first of all that the index change at the center of the rod shown in figure 3-2 does not agree with the measured values given in figure 1-20 of Section I. We shall return to discuss this discrepancy in the last part of the present section. We shall assume for the present, however, that the radial dependence of the refractive index given in figure 3-2 [i. e., $n_r(r, t) - n_r(o, t)$] is correct.

From figure 3-2 we may determine the value of $n_r(r, t)$ at $r/R = 0.5$ and 0.9 . Using these values and equation II. 36, with $r \equiv r_o \approx r_{lr}$ and $\mathcal{L}_o = 7.62$ cm, we may compute the angle $\theta_r(r, t)$. The calculated results are shown in figure 3-3 compared to the measured values found in Section I, figure 1-24. We see that good agreement exists between experiment and theory and that the rod acts like a negative lens.

Finally, with the aid of equations II. 25 and II. 37, we compute the relative phase angle $\delta_r(r, t) - \delta_r(o, t) = \frac{2\pi}{\lambda} [\Delta P_r(r, t) - \Delta P_r(o, t)]$, again at two representative times. In these computations, we have set d_o equal to zero in equation II. 37 to correspond to the fact that the camera used in the Mach-Zehnder experiment was focused on the end of the glass rod. In addition, we have again assumed $r \equiv r_o \approx r_{lr}$. The results of these computations are compared in figures 3-4 and 3-5 to the experimentally measured values given in Section I (figure 1-4). Again, the theoretically computed values agree with the experimentally determined values within the experimental error.

We have seen in this first part of Section III, therefore, that if the stress phase angle and change in physical length experiments are used to determine the temperature, then this temperature and the theory of Section II successfully predicts the radial dependence of the remaining experimental results. The magnitude of the change in refractive index at the center of the rod does not, however, agree with experiment. We consider now this discrepancy.

C. REFRACTIVE INDEX CHANGE DUE TO EXCITED NEODYMIUM ION POPULATION

Consider first a direct comparison between the experimentally determined refractive index change at $r = o$ and that calculated from equation II. 33 and the temperature rise data of figure 3-1. Both quantities as a function of time are shown in figure 3-6. Curve A in this figure is that curve which when added to $n_r(o, t) - n_o$ yields the experimentally

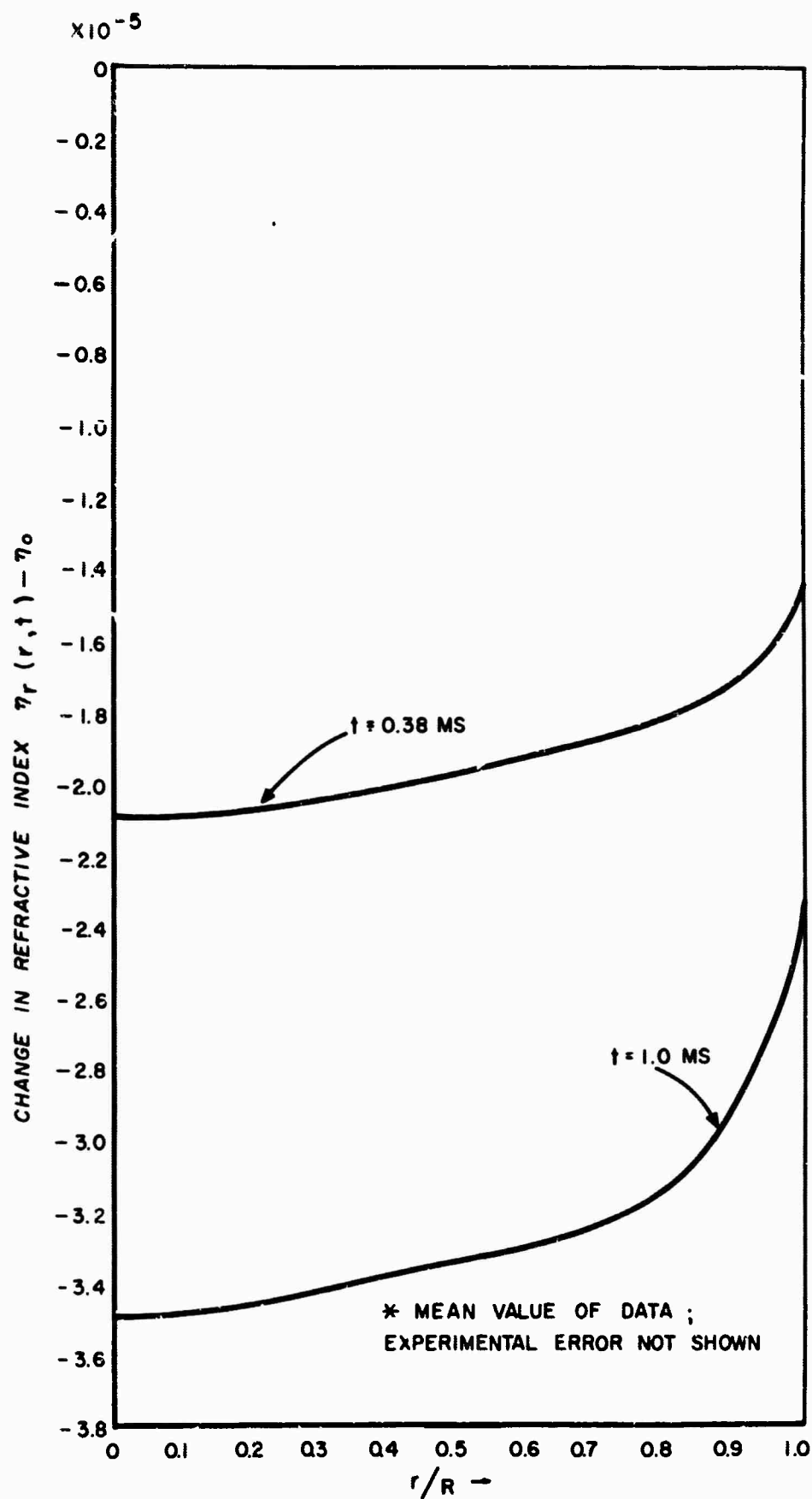


Figure 3-2. Calculated Change in Refractive Index* vs. r/R for Radially Polarized Radiation (Roç AO-2 at 11, 500j Pump Energy)

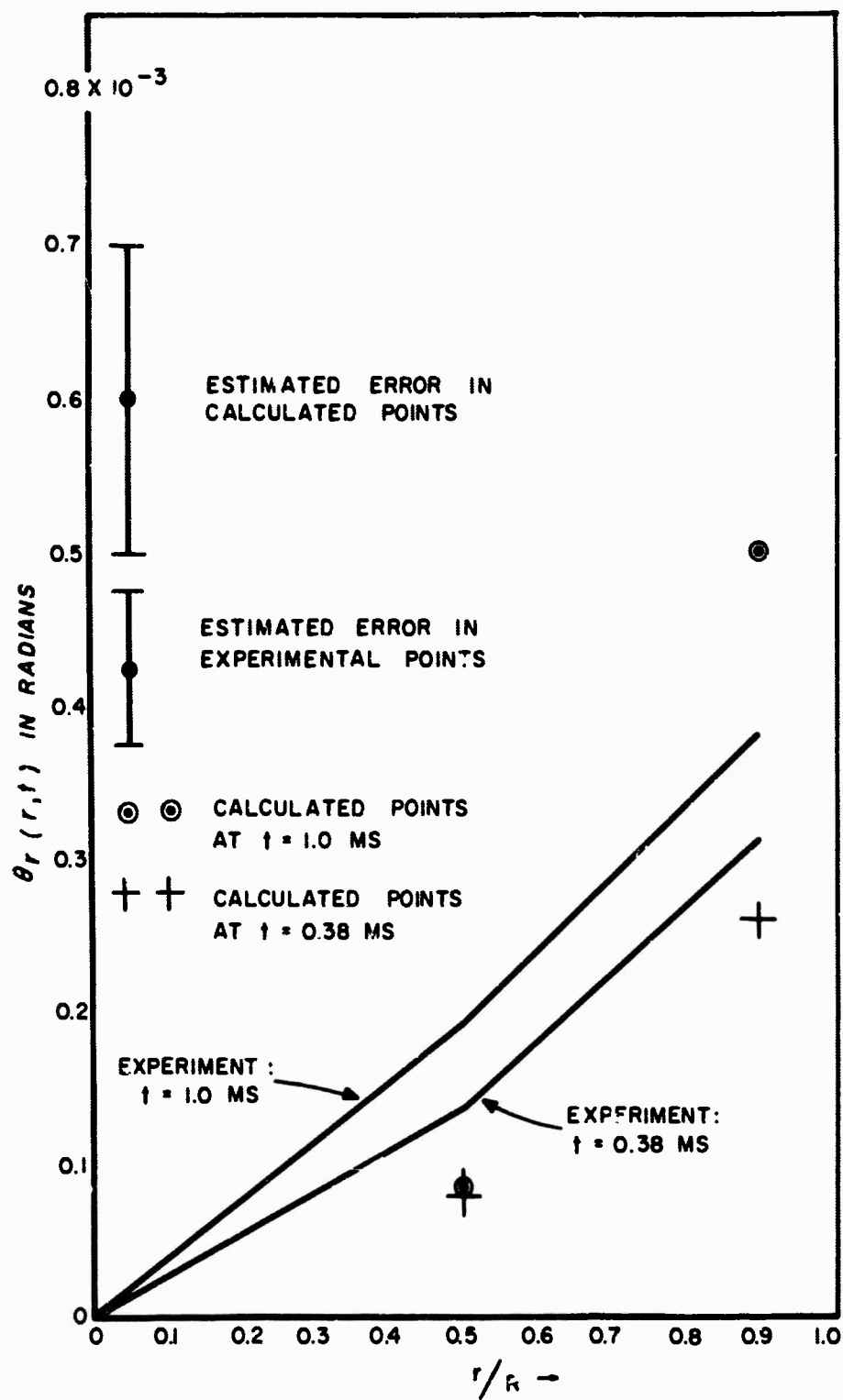


Figure 3-3. Calculated and Experimental Probe Beam Angle $\theta_r(r,t)$, for Rod AO-2 at 11,500j Pump Energy

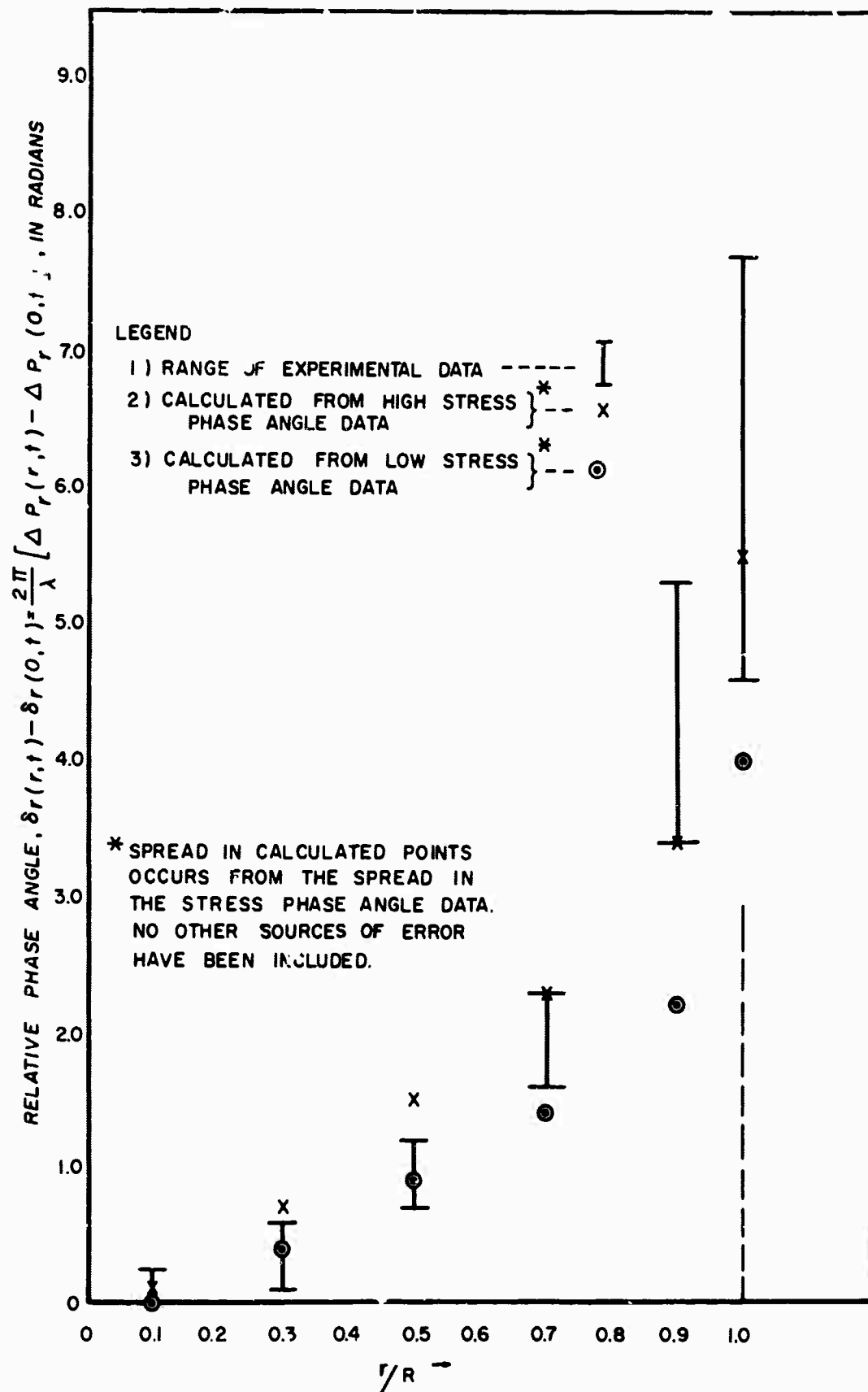


Figure 3-4. Calculated and Experimental Relative Phase Angle for Radially Polarized Radiation vs. r/R at $t = .38$ ms for Rod AO-2 at 11,500 j Pump Energy

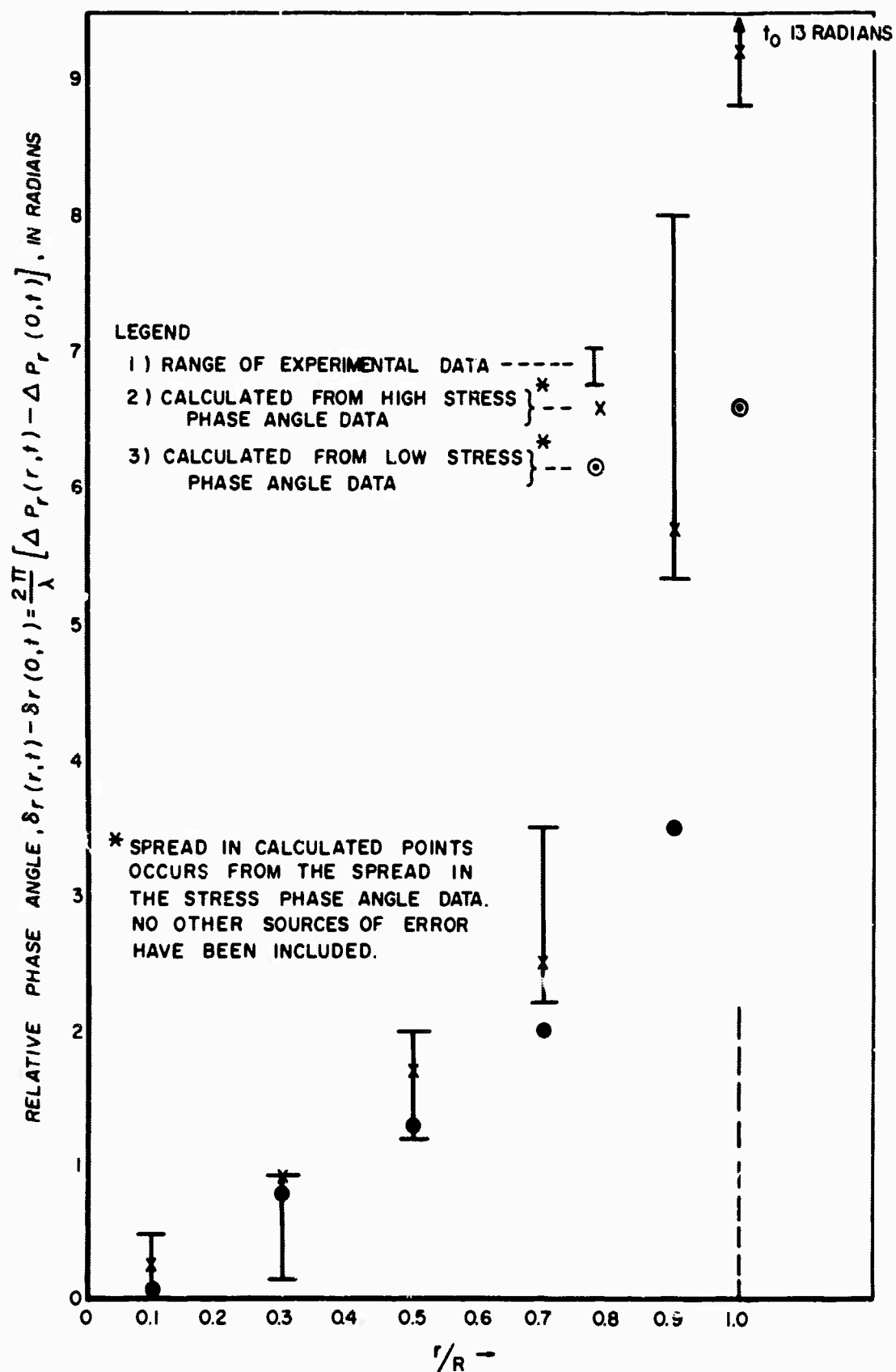


Figure 3-5. Calculated and Experimental Relative Phase Angle for Radially Polarized Radiation vs r/R at $t = 1.0$ ms for Rod AO-2 at 11,500j Pump Energy

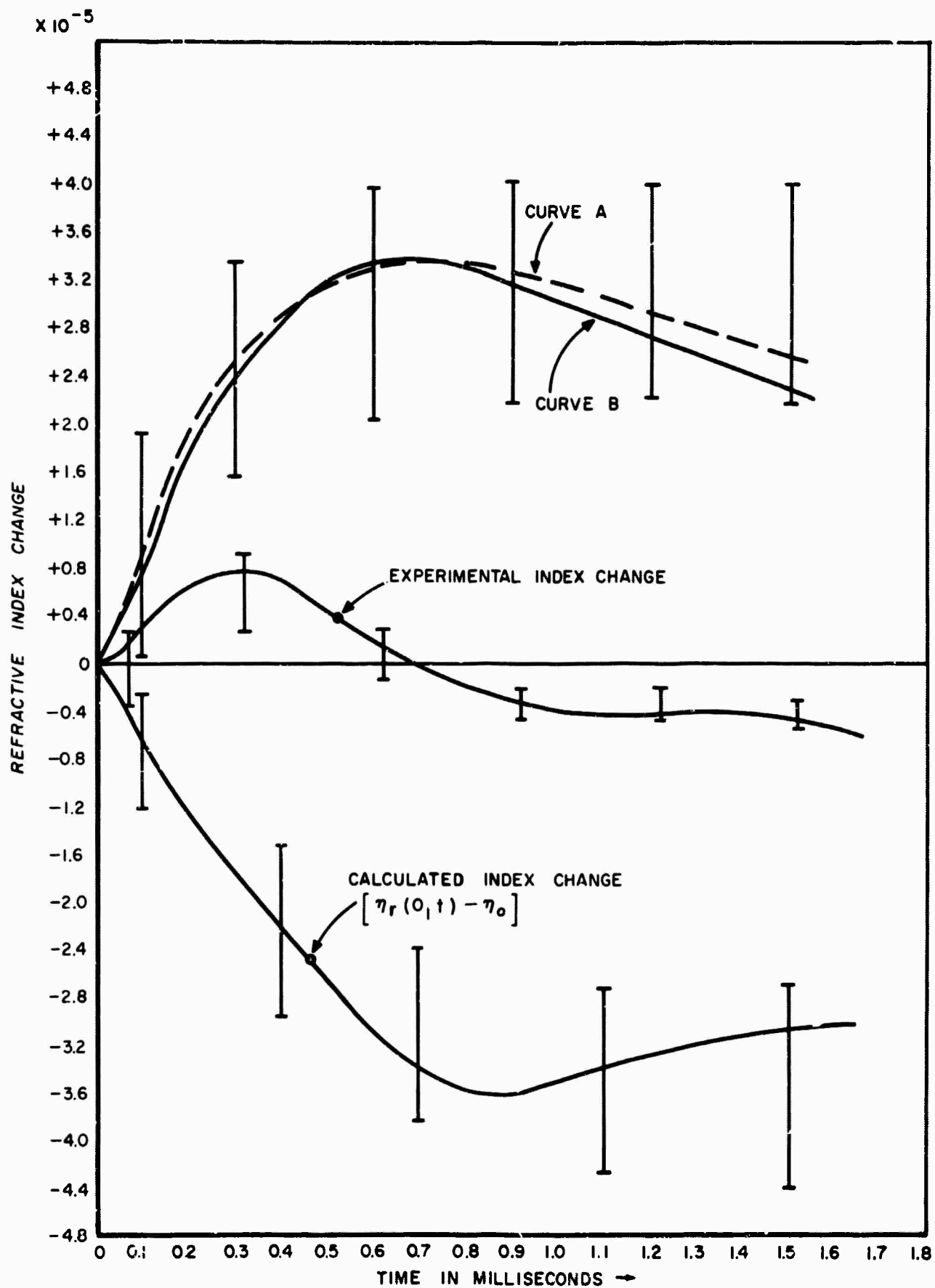


Figure 3-6. Refractive Index Change at r/R_0 vs. Time for Rod AO-2 at 11,500 Pump Energy

determined curve. Any proposed mechanism to account for Curve A must, therefore, have the same time behavior, approximately the same magnitude, and in addition be essentially independent of radius. The latter requirement is implied by the successful calculation of the angle $\theta_r(r, t)$ and the relative phase angle described in the first part of this section.

The only mechanism we have found which satisfies all three requirements arises from a change in the polarizability of the neodymium ion when it is excited to the metastable $^4F_{3/2}$ level. In order to gain a relation which describes the expected index of refraction change with excited neodymium ion population, we first note the well known relation²

$$(III.4) \quad n^2 - 1 = 4\pi\alpha N$$

provided $n-1 \ll 1$. Here n is the index of refraction, α the polarizability of the atom, and N the number of atoms per unit volume. Let the concentration of neodymium ions in the ground $^4I_{9/2}$ level at a given time t be $N_1(t)$ while the number in the excited $^4F_{3/2}$ level be $N_3(t)$. Then assume the total concentration N to be³

$$(III.5) \quad N = N_1(t) + N_3(t).$$

Now if the polarizability of the neodymium ion is α_1 in the ground level and α_3 in the metastable level, it is easy to show that the change in index of refraction $\Delta n(N_3)$ which arises as a result of a finite excited state population $N_3(t)$ is

$$(III.6) \quad \Delta n(N_3) = 2\pi(\alpha_3 - \alpha_1)N_3(t)$$

The electronic polarizability at angular frequency ω is given by⁴

$$(III.7) \quad \alpha = \frac{e^2}{m} \sum_j \frac{f_{ij}}{\omega_{ij}^2 - \omega^2}$$

where e , m , f_{ij} and ω_{ij} are respectively the electric charge, mass of the electron, oscillator strength for a transition from state i to state j , and the energy difference $E_j - E_i$ between states j and i divided by \hbar . The difference $\alpha_3 - \alpha_1$ may therefore be written as

$$(III.8) \quad \alpha_3 - \alpha_1 = \frac{e^2}{m} \left\{ \sum_j \frac{f_{3j}}{\omega_{3j}^2 - \omega^2} - \sum_l \frac{f_{1l}}{\omega_{1l}^2 - \omega^2} \right\}$$

where \sum_j runs over all of the excited states of Nd^{+3} and \sum_l runs over the ground state and all excited states except the metastable state. Because of the small oscillator strengths for $4f \rightarrow 4f$ transitions compared to those for the allowed $4f \rightarrow 5d$ transitions and because of

the much larger number of $4f \rightarrow 5d$ transitions compared to $4f \rightarrow 4f$ transitions⁵, the important contribution to the polarizability difference $\alpha_3 - \alpha_1$, arises from $4f \rightarrow 5d$ transitions. We therefore neglect the contributions to $\alpha_3 - \alpha_1$ from all transitions except $4f \rightarrow 5d$. We further replace the 5d band by one state at ω_1/\hbar above the ground state and assume that the oscillator strength f_1 to this 5d state is the same from either level 3 or level 1. This should be a good approximation since these are all allowed $4f \rightarrow 5d$ transitions. Equation III.8 then becomes

$$(III. 9) \quad \alpha_3 - \alpha_1 = \frac{e^2 f_1}{m} \left\{ \frac{1}{\omega_3^2 - \omega^2} - \frac{1}{\omega_1^2 - \omega^2} \right\}$$

where $\omega_3 \equiv \omega_1 - \omega_{13}$ and where ω_{13}/\hbar is the energy of the excited level 3 above the ground level 1.

We next calculate an effective value of $e^2 f_1/m$ in front of equation III. 9. The refractive index of the unpumped rod changes by $\Delta n = -6 \times 10^{-3}$ at frequency ω_s (corresponding to the sodium D line) when the concentration of Nd^{+3} ions is changed from $N^1 = 1 \times 10^{20} \text{ cm}^{-3}$ to $N^{11} = 6 \times 10^{20} \text{ cm}^{-3}$ ⁽⁶⁾. Since

$$(III. 10) \quad \Delta n = 2\pi \alpha_1 (N^1 - N^{11}),$$

we have

$$(III. 11) \quad \alpha_1 = \frac{\Delta n}{2\pi (N^1 - N^{11})} = \frac{e^2}{m} \frac{f_1}{\omega_1^2 - \omega_s^2}$$

Using equation III. 11 and replacing ω_3 by $\omega_1 - \omega_{13}$, equation III. 9 may be written as

$$(III. 12) \quad \alpha_3 - \alpha_1 = \frac{\Delta n \omega_{13} (\omega_1^2 - \omega_s^2) (2\omega_1 - \omega_{13})}{2\pi (N^1 - N^{11}) (\omega_1^2 - 2\omega_1 \omega_{13} + \omega_{13}^2 - \omega^2) (\omega_1^2 - \omega^2)}.$$

Inserting the appropriate values in this equation yields $\alpha_3 - \alpha_1 = 0.8 \times 10^{-24} \text{ cm}^3$.

The refractive index change then becomes

$$(III. 13) \quad \Delta n(N_3) = 2\pi (\alpha_3 - \alpha_1) N_3 = 5 \times 10^{-24} N_3(t).$$

The required peak value of $\Delta n(N_3)$ is shown in figure 3-6 (curve A) to be approximately 3.6×10^{-5} . From equation III. 13 this would imply a value of $N_{3 \text{ max}}$ of $7 \times 10^{18} \text{ cm}^{-3}$. This is a reasonable approximate value for $N_{3 \text{ max}}$ at this pump energy since it falls between the upper and lower bounds for N_3 which may be estimated from the following

threshold considerations. First, let us consider the upper bound for N_3 . As will be discussed shortly, we have observed the 1.06μ radiation along the axis of the rod during the pump period with no reflectors on the rod (except of course the Fresnel reflection at each end). No laser action is observed. Therefore $N_{3 \text{ max}}$ must be lower than the minimum population $N_{3\mu}$ required for laser threshold under these conditions. The minimum population inversion ΔN required for laser threshold with the Fresnel reflectivities of the ends $r_1 = r_2 = .04$ is⁷

$$(III. 14) \quad \Delta N = N_{3\mu} - \frac{g_2}{g_1} N_2 = 2\pi^2 C \frac{n_o^2 \tau \Delta\lambda \{ -\ln [r_1 r_2] \}}{\lambda_o^4 \rho_o}$$

where τ is the lifetime of level 3 due to spontaneous emission of radiation by a transition between levels 3 and 2, λ is the wave length in vacuum at the peak of the Lorentzian spontaneous emission line with a full width at half-height of $\Delta\lambda$, and C is the speed of light. Using constants supplied by the American Optical Corporation,* we find $\Delta N = 1.3 \times 10^{19} \text{ cm}^{-3}$. Since we may take N_2 to be zero, $N_{3\mu} = 1.3 \times 10^{19} \text{ cm}^{-3}$. Now let us consider the lower bound for N_3 . We may safely take this to be the population inversion $N_{3\lambda}$ obtained at 1650j pump energy. This is the pump energy necessary to achieve laser operation with $r_1 = .99$ and $r_2 = .70$ (see section C.1, figure 1-2. The value of $N_{3\lambda}$ obtained from equation III. 14 with the above values of r_1 and r_2 is $0.7 \times 10^{18} \text{ cm}^{-3}$.

It has been shown theoretically that the magnitude of $\Delta n (N_3)$ can account for curve A, figure 3-6. Next, it is necessary to show that the temporal variation of $N_3(t)$ falls within the experimental error limits imposed on the same curve.

Consider a simplified two energy level model to estimate the time dependence of $N_3(t)$. The rate equation for this system can be written in this form⁸

$$(III. 15) \quad \dot{N}_3 = -\dot{N}_1 = P(t) N_1(t) - \frac{1}{\tau_{32}} N_3(t) - W(t) N_3(t)$$

where $P(t)$ is a pumping function, τ_{32} is the measured florescent time constant of the $^4F_{3/2}$ metastable level, and $W(t)$ is a function accounting for stimulated emission. Substituting $N_o = N_1(t) + N_3(t)$ into III. 15 yields

$$(III. 16) \quad \frac{dN_3}{dt} = P(t) [N_o - N_3(t)] - N_3(t) \left[\frac{1}{\tau_{32}} + W(t) \right]$$

*See Appendix F

For laser rod AO-2, $N_0 = 4.6 \times 10^{20}$ ions/cc, and the maximum value of $N_3(t)$ can be assumed from the previous threshold calculation to be less than 1.3×10^{19} /cc. Thus, the approximation can be made that $N_3(t) \ll N_0$. Equation III. 16 then has the solution

$$(III. 17) \quad N_3(t) = e^{-\gamma(t)} N_0 \int_0^t e^{\gamma(t)} P(t) dt$$

where

$$(III. 18) \quad \gamma(t) = \int_0^t W(t) dt + t/\tau_{32}.$$

The function $P(t)$ can be assumed to be proportional to the pump intensity (See figure 1-1). The function $W(t)$ has yet to be determined.

An experiment was set up in the laboratory to determine the time variation of $W(t)$ by observing the axial emission of radiation at 1.06μ (11, 500 joules pump energy) from the laser rod. This experiment is diagramed in figure 3-7. By means of a series of tests it

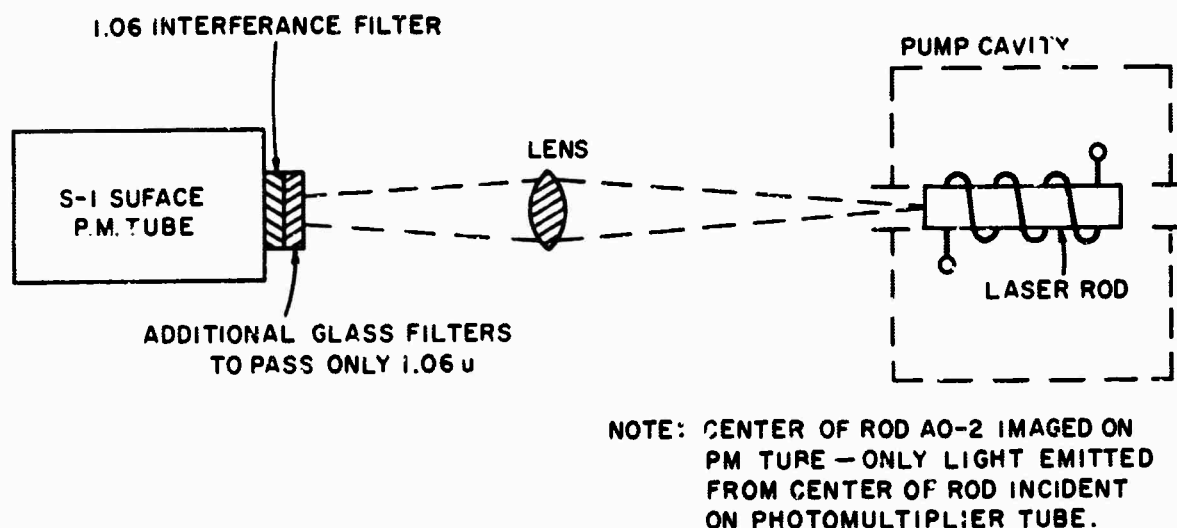


Figure 3-7. Experimental Diagram: Measure of Temporal Variation in $W(t)$

was determined that almost all of the radiation observed (light sum curve) was due to stimulated emission. Therefore, the temporal variation of the light sum curve measured in this experiment is that of $W(t)$. Normalized curves of $W(t)$ and $P(t)$ are shown in figure 3-8.

Using figure 3-8 and equations III. 17 and III. 18 with parameters $W(t)_{\text{peak}} = 100 \text{ sec}^{-1}$, $P(t)_{\text{peak}} = 50 \text{ sec}^{-1}$, $N_3(t)$ may be determined with a peak value of $6.3 \times 10^{18} \text{ cm}^{-3}$. Using this curve for $N_3(t)$ and equation III. 13, curve B shown in figure 3-6 has been drawn.

D. CONCLUSION

It is now clear that within experimental error a new term can legitimately be added to equations II. 33 and II. 34, and that it has the form given in equation III. 13.

This result is extremely important since it illustrates that pump induced optical distortions in Nd^{+3} doped glasses are not solely determined by temperature and temperature gradients, but are strongly influenced by the magnitude and distribution of inversion within the laser rod.

The addition of this new term to the refractive index equations modifies the theory in Section II only to the extent of changing equations II. 33 and II. 34.

Adding this term equally to the radial and tangential refractive index has no effect on the determination of $T(r, t)$ from the stress phase angle and change in physical length data. It does, however, effect the calculation of $\delta_r(r, t) - \delta_r(0, t)$, and $\theta_r(r, t)$ as carried out in section III. B. Since the radial dependence calculations in Section III. B were completed without the addition of the term $\Delta n [N_3(t)]$, and reasonable correlation was still obtained, one must conclude that the radial dependence of $N_3(t)$ was not very great in our experiments. This is consistent with the fact that the total phase angle change due to the neodymium ions, shown in figure 1-9, is a constant within about ten percent across the rod diameter.

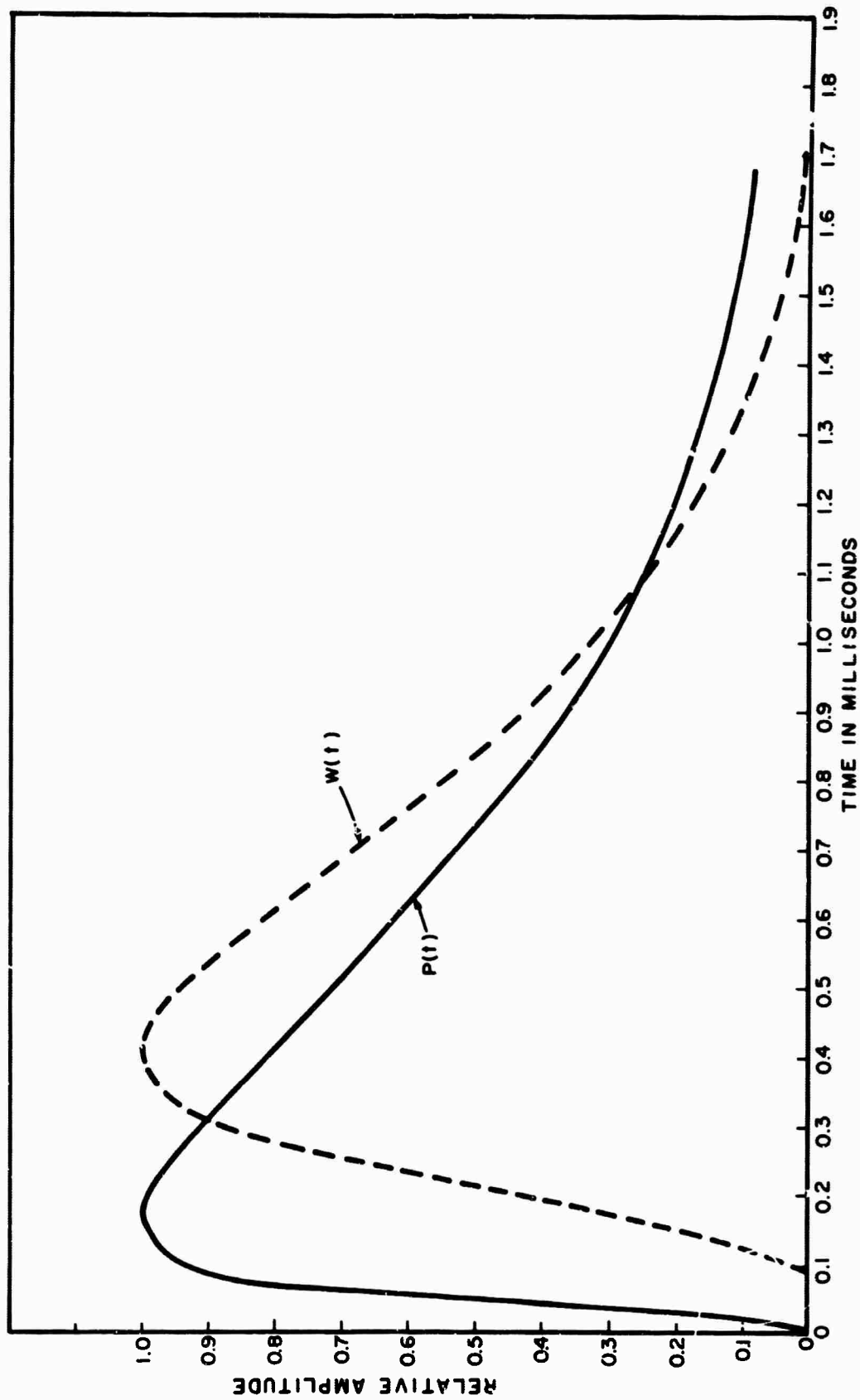


Figure 3-8. Temporal Variation of $P(t)$ and $W(t)$ for Rod AO-2 at 11,500j Pump Energy

E. REFERENCES

1. First Semi-Annual Report, "Thermal Optic Distortion", Contract NONr-4874(00), pgs. 2-4 & 2-5.
2. M. Born & E. Wolf, Principles of Optics, Pergamon Press (1959), pg. 95.
3. E. Snitzer, "Neodymium Glass Laser", Presented at 3rd International Symposium on Quantum Electronics, February 1963, Paris, France.
4. C. Kittel, Introduction to Solid State Physics, John Wiley & Sons, Inc. (1957) pg. 166.
5. G.H. Dieke and H.M. Crosswhite, Appl. Opt. 2, 675 (1963).
6. Data Sheet on Rare Earth Laser Glass Rods issued by the Eastman Kodak Company (October 1962).
7. E.P. Riedel, Westinghouse Research Report 62-112-259-R1, pg. 5 (1962).
8. K. Shimoda, Proceedings of the Symposium on Optical Masers, New York, 1963, Polytechnic Press, Brooklyn, New York, pg. 95.

IV. SUMMARY

The present report is a theoretical and experimental study of optical distortions induced in neodymium-doped glass by pump radiation. The report is divided into three major sections. The first and second sections describe respectively the experimental and theoretical work while the third section is used to quantitatively compare the results of the first two sections.

The aim of the experimental work presented in the first section is to obtain quantitative data which can be used to check the theory. Before this could be done, however, two separate experimental investigations had to be performed. The first of these consisted of a study of the static optical distortions present in the 3" long rods. It was shown that for some rods, these static distortions were so large and of such low symmetry as to prevent their use for obtaining quantitative data. The results of this study led to the selection of rods which possessed static distortions small enough to be ignored in the dynamic experiments. The second investigation consisted of obtaining radially symmetric optical distortions throughout the dynamic period. This was achieved by using a helical lamp, a frosted glass tube between the rod and lamp, and a specially designed rod holder. This was a critical part of the experimental work since it appears that the only tractable theoretical description of the index of refraction is based on the assumption of a radial temperature distribution within the rod. Once these two preliminary investigations were completed, the data to be used in checking the theory was obtained. Measurements were made of the optical path length as a function of radius, time, and polarization and the change in physical length as a function of time and radius. In addition, the index of refraction along the rod axis as a function of time was measured, as was the refraction, as a function of time and radius, of a small diameter probe beam passing through the rod.

In Section II, Fermat's principle is used for the first time in the analysis of the dynamic optical problem to gain expressions for the slope and trajectories of the rays through the material for a plane wave input. These results are then used to predict ray refraction, beam divergence, and optical path length through the material as a function of radius, time, and polarization. Effects associated with the fact that the rods are not very long compared to their diameter have been ignored.

In the third section, the experimental and theoretical results are compared in two parts. In the first part, the change in the measured parameters with the radial coordinate is compared to the theoretical predictions. This is done by first using the measurements of

the optical path length difference between the radially and tangentially polarized components and the change in physical length of the rod to determine the temperature of the rod as a function of time and radius. This temperature is then inserted into the theoretical expression for the optical path length change and for the refraction angle of radially polarized radiation. Good agreement is found for the variation in the measured and calculated parameters with radius.

In the second part of the third section, the correlation between experiment and theory is considered only along the axis of the rod. It is first observed that the measured refractive index change does not agree with the theory. However, this discrepancy can be removed by the addition of a new term to the expression for the change in index of refraction. This term is proportional to the population of neodymium ions in the metastable $^4F_{3/2}$ level and takes into account the fact that the polarizability of the neodymium ion is different in the $^4F_{3/2}$ level than in the ground level. The importance of this new term cannot be overemphasized since it implies that even if a glass is "athermalized", large optical distortions can arise as a result of a non-uniform population inversion.

V. RECOMMENDATIONS FOR FUTURE WORK

Further investigation of the refractive index change due to the population of neodymium ions in the $^4F_{3/2}$ level is needed. Index of refraction measurements at 6328\AA similar to those made in this report should be made along with a measurement of population in the $^4F_{3/2}$ level. A satisfactory quantitative check of this index term at 6328\AA would complete a successful description of optical phenomena in glass rods at this wavelength.

To quantitatively understand the far field pattern obtained with a given input wave to the glass amplifier, measurements similar to those made in this report should be made at 1.06μ in conjunction with a determination of gain and excited level population. Due consideration should again be given to dispersion phenomena. This study should first be conducted with the same 3-inch rods used in the present report. After a satisfactory understanding is achieved with these short rods, similar work should be done using long rods; again with due attention directed toward the achievement of the critical requirement of low static stress and radially symmetric dynamic distortions. Perhaps the best way to achieve uniform pumping for long rods at high energies is to employ a coaxial lamp¹ developed at the Westinghouse Research Laboratories.

The successful conclusion of the above work would place one in a favorable position to consider the problem of quantitatively describing the output of a glass oscillator. Whether or not this complex problem can be treated in such a way as to yield a description which will be of use from a practical point of view is, however, not clear at the present time.

¹ J. P. Lesnick and C. H. Church, IEEE, J. of Quantum Electronics, Vol. QE-2, Pg. 16, 1966.

APPENDIX A
EFFECTS OF RESIDUAL STRESS

APPENDIX A

EFFECTS OF RESIDUAL STRESS

To qualitatively determine the effect of residual stress in glass laser rods, several types of laser rods were analyzed in a plane polariscope. A diagram of the polariscope is shown in figure A-1.

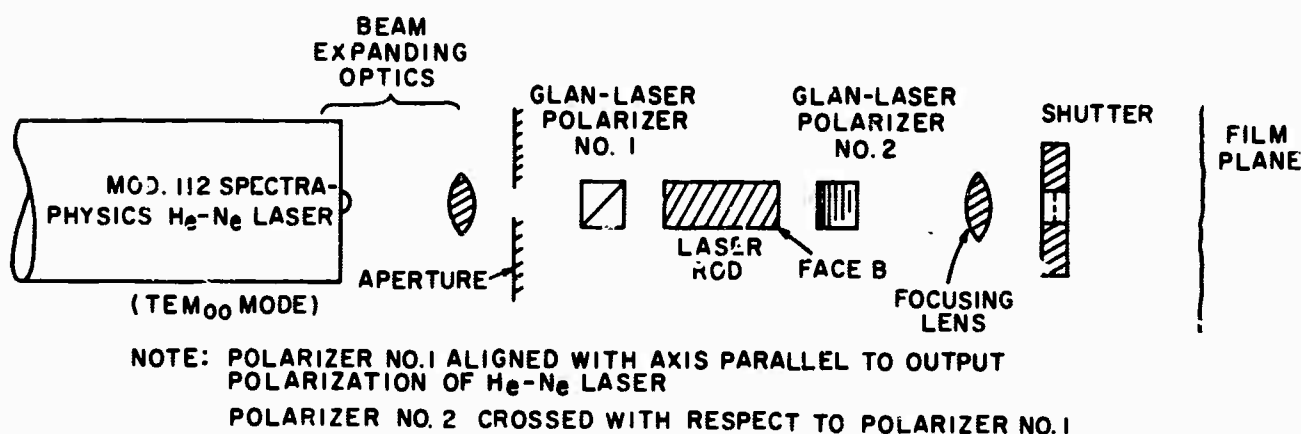


Figure A-1. Polariscope Diagram

The pattern recorded on the film plane is the pattern of the light transmitted through the second polarizer as it exists at face B of the laser rod. Several pictures were taken as the rod was rotated approximately 45° between each picture. By rotating the rod all regions which possess residual stress could be observed. Most rods tested did not possess radial symmetry of residual stress; and for these quantitative data was not obtained. For those which did possess radial symmetry, the difference between the radial and tangential stress vectors was calculated. Several of the rods tested in the polariscope were also placed in the pumping cavity and inserted into one arm of a Mach-Zehnder Interferometer. A diagram of the experimental arrangement is shown in figure A-2. The interferometer was initially adjusted so that the entire field covering the laser rod was uniform. The focusing lens served to image end B of the laser rod on the film plane of the high-speed framing camera. Photographs of the pump-induced optical distortion in the laser rod were recorded during the pump cycle, and were compared with the previously obtained residual stress patterns.

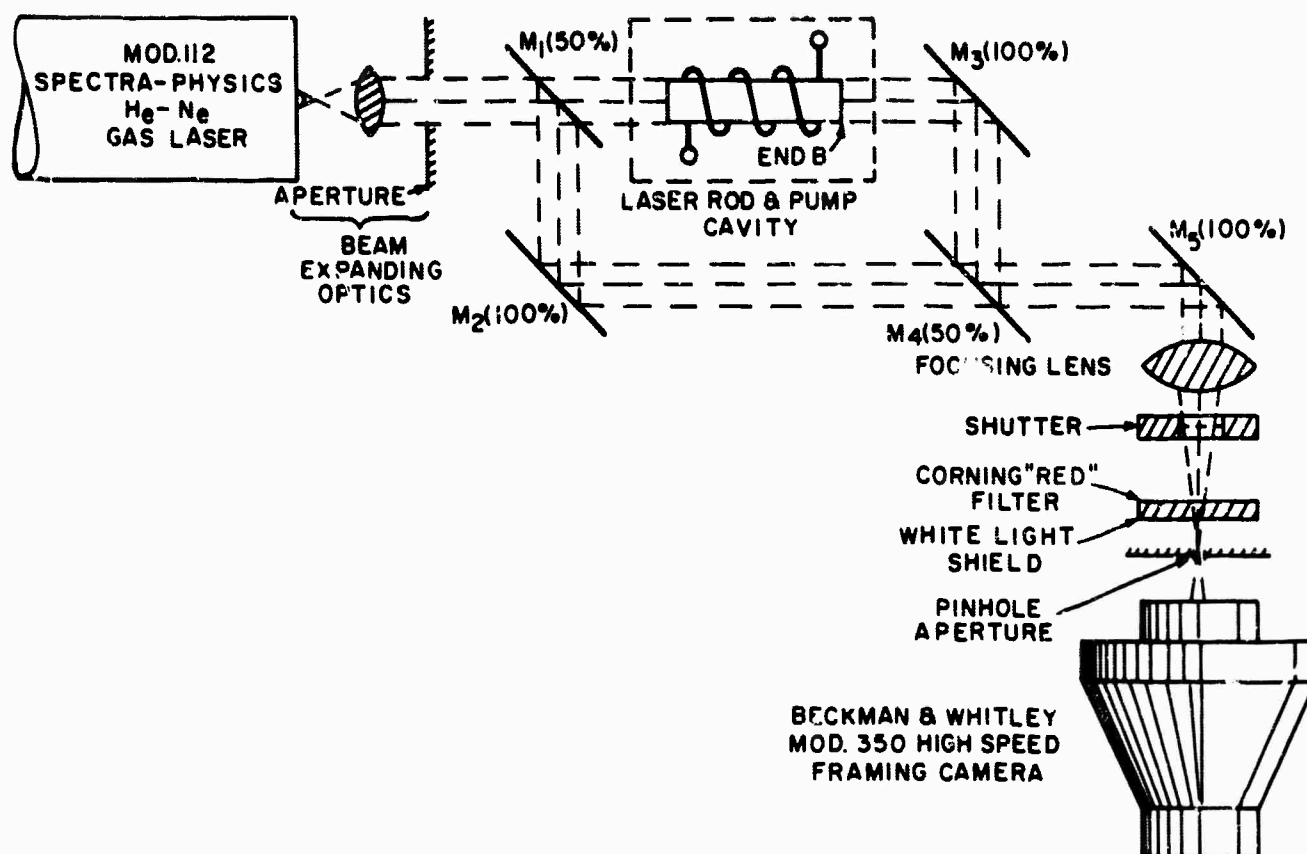


Figure A-2. Mach-Zehnder Experiment

Table A-I shows the laser rods tested in the polariscope, while figure A-3 shows the pictorial results of these tests. The ruby rod tests are included for comparison purposes. It is interesting to note that of all the rods tested, the 6-inch long P. P. G. rod appeared to have the least residual stress. The stress present was different from that observed in all of the other glass rods in that it appeared to be principally aligned in one direction across the rod diameter.

The three Kodak rods showed varying degrees of stress but exhibited similar stress patterns. Common to all Kodak rods was the concentration of stress near the outer surface of the rod coupled with large stress gradients. Rod K-2 originally had a polished surface while rods K-1 and K-3 had frosted surfaces. The most probable reason for the high stress near the surface of the Kodak rods seems to be that surface stresses were introduced when the rods received their frosted surfaces at the factory.

The first American Optical laser rods tested in the polariscope were the clad rods AO-4, AO-5, and the undoped rod AO-3. The clad rods were taken from the same melt. It was found that the clad rods possessed extremely high residual stress. In addition, the stress in the clad rods appeared to be equal in magnitude to that observed in a Linde 0° ruby.



Rod K-1

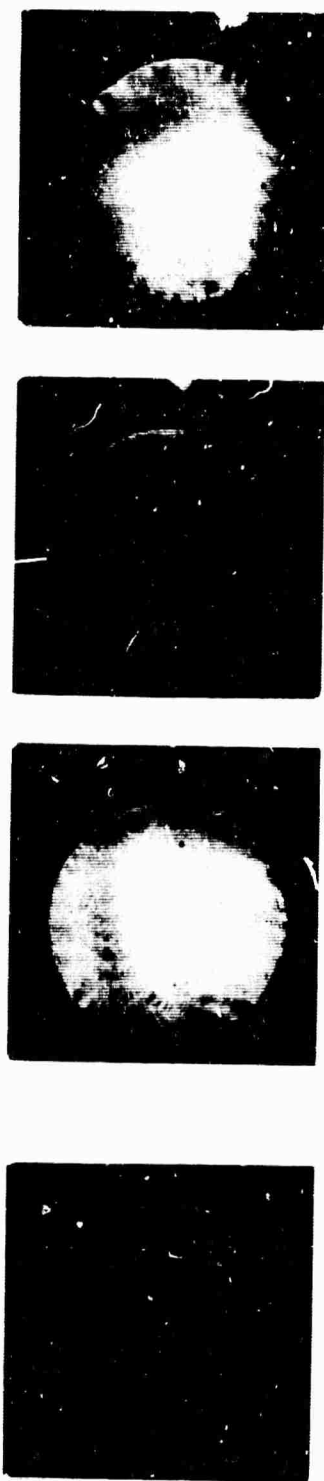


Rod K-2

Figure A-3a. Polariscope Patterns

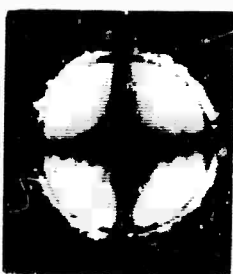


Rod K-3

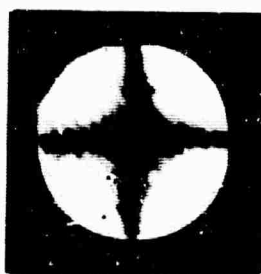


Rod PPG-1

Figure A-3b. Polariscope Patterns



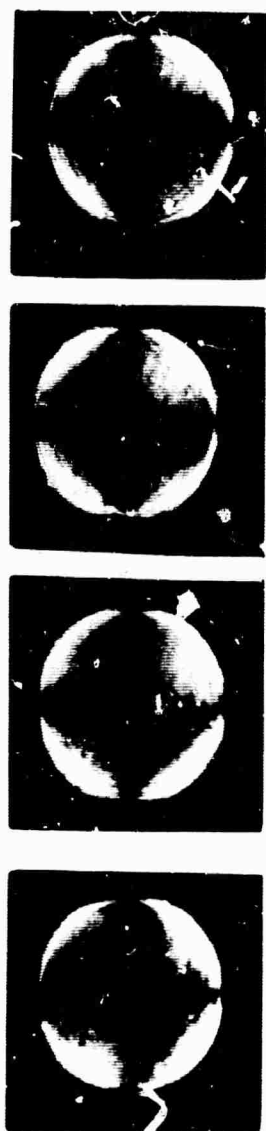
Rod AO-1



Rod AO-2



Figure A-3c. Polariscope Patterns



Rod AO-3



Rod AO-4

Figure A-3d. Polariscope Patterns



Rod L-1



C axis // to polarization (\updownarrow)



C axis at 45° to polarization (\updownarrow)

Rod L-2

Figure A-3e. Polariscope Tests

Polarization (\updownarrow)
⊥ to C axis



Polarization (\updownarrow)
|| to C axis

Rod L-3

1
C axis parallel // to
polarization (\updownarrow)



2
C axis 45° to
polarization (\updownarrow)



Rod L-4



Rod M-1

Figure A-3f. Polariscope Patterns

TABLE A-1. LASER RODS TESTED

ROD DESIGNATION	MANUFACTURER	COMMENTS
K-1*	Kodak	} Type ND-10 Kodak Laser Glass Used on Contract Nonr-3922(00) (See Appendix C.)
K-2**	Kodak	
K-3*	Kodak	
P. P. G. -1*	Pittsburgh Plate Glass	Experimental Rod 3/8 x 6 inches obtained from Westinghouse Research Laboratories
AO-1*	American Optical	} Specially Annealed Laser Rods (See Appendices D and E.)
AO-2*	American Optical	
AO-3* ("control")	American Optical	Undoped glass host (See Appendix D.)
AO-4**	American Optical	} 1/2 x 3 inch clad laser rods (See Appendix D.)
AO-5**	American Optical	
L-1*	Linde Co.	3/8 x 3 inch, .05%Cr ⁺⁺⁺ , 0° ruby
L-2*	Linde Co.	} 3/8 x 3 inch, .05%Cr ⁺⁺⁺ 60° ruby
L-3*	Linde Co.	
L-4*	Linde Co.	
M-1**	Muller Co.	3/8 x 3 inch, .05%Cr ⁺⁺⁺ , 0° ruby

*frosted surface finish

**polished surface finish

Rod AO-3 ("control" rod) is apparently a typical example of the residual stress to be found in unclad 3/8 x 3 inch Alux laser rods.

Under the criteria that the rods to be used to obtain quantitative data have either small or radially symmetric residual stress, it was obvious that rods AO-1 and AO-2 were the only rods which satisfied one of these requirements. Rods AO-1 and AO-2 were specially prepared by American Optical for this contract; the details of their preparation are given in Appendix E.

Since rods AO-1 and AO-2 possessed radially symmetric residual stress, the value of the difference between the radial and tangential stress components ($S_r - S_\theta$) could be determined. Assuming that the stress present is uniform along the length of the laser rod, the phase angle between the radial and tangential polarization components passing through the rod is given in cylindrical coordinates by:¹

¹E. V. Condon & H. Odishaw, Handbook of Physics, McGraw-Hill (1958), pg. 3-86

$$(A.1) \quad \delta(r, \theta) = \cos^{-1} \left[1 - \frac{I_t(r, \theta)}{I_i(r, \theta)} \frac{2}{\sin^2 2\theta} \right]$$

where $I_t(r, \theta)$ is intensity transmitted with polarizers crossed,
 $I_i(r, \theta)$ is intensity transmitted with polarizers uncrossed, and
 θ is azimuthal angle between the first polarizer axis and r along
 which $\delta(r, \theta)$ is being determined.

The relation between the stress, refractive index, and stress optic coefficients is given by:¹

$$(A.2) \quad S_r - S_\theta = \left[\frac{n_r - n_\theta}{B_\perp - B_\parallel} \right]$$

where subscript r represents the radial direction,

θ is the tangential direction, and

$B_\perp - B_\parallel$ is the difference between the stress optic coefficients.

If the length of the rod is L_0 and the wavelength λ , the difference in phase between the radial and tangential components is given by $\frac{2\pi L_0}{\lambda} (n_r - n_\theta)$; then equations (A.1) and (A.2) can be combined to give:

$$(A.3) \quad \Delta S(r, \theta) = S_r(r, \theta) - S_\theta(r, \theta) \\ = \frac{\lambda}{2\pi L_0 (B_\perp - B_\parallel)} \cos^{-1} \left[1 - \frac{I_t(r, \theta)}{I_i(r, \theta)} \frac{2}{\sin^2 2\theta} \right]$$

A plot of $\Delta S(r, \theta)$ as a function of r for rods AO-1 and AO-2 is shown in figure A-4. Rod AO-2 exhibited a more uniform stress distribution than AO-1; thus it was chosen as the test rod for this contract.

Three glass rods were checked in a Mach-Zehnder Interferometer to determine what correlation existed between residual stress and dynamic optical path length changes during the pump cycle. These were K-1, K-2, and K-3. Figure A-5 is a pictorial comparison between regions of highest residual stress and regions of maximum distortion to the optical path for each rod. Two conclusions may be drawn:

- 1) Those regions of maximum residual stress correspond to those regions of maximum optical path length distortion;
- 2) The greater the residual stress, the greater is the optical path length distortion.

It is interesting to note that for radially symmetric stress as in rod AO-2 there were no optical path distortions traceable to residual stress. This is not to say that radial residual stress has no effect on the optical path length through the rod during the pump cycle, but

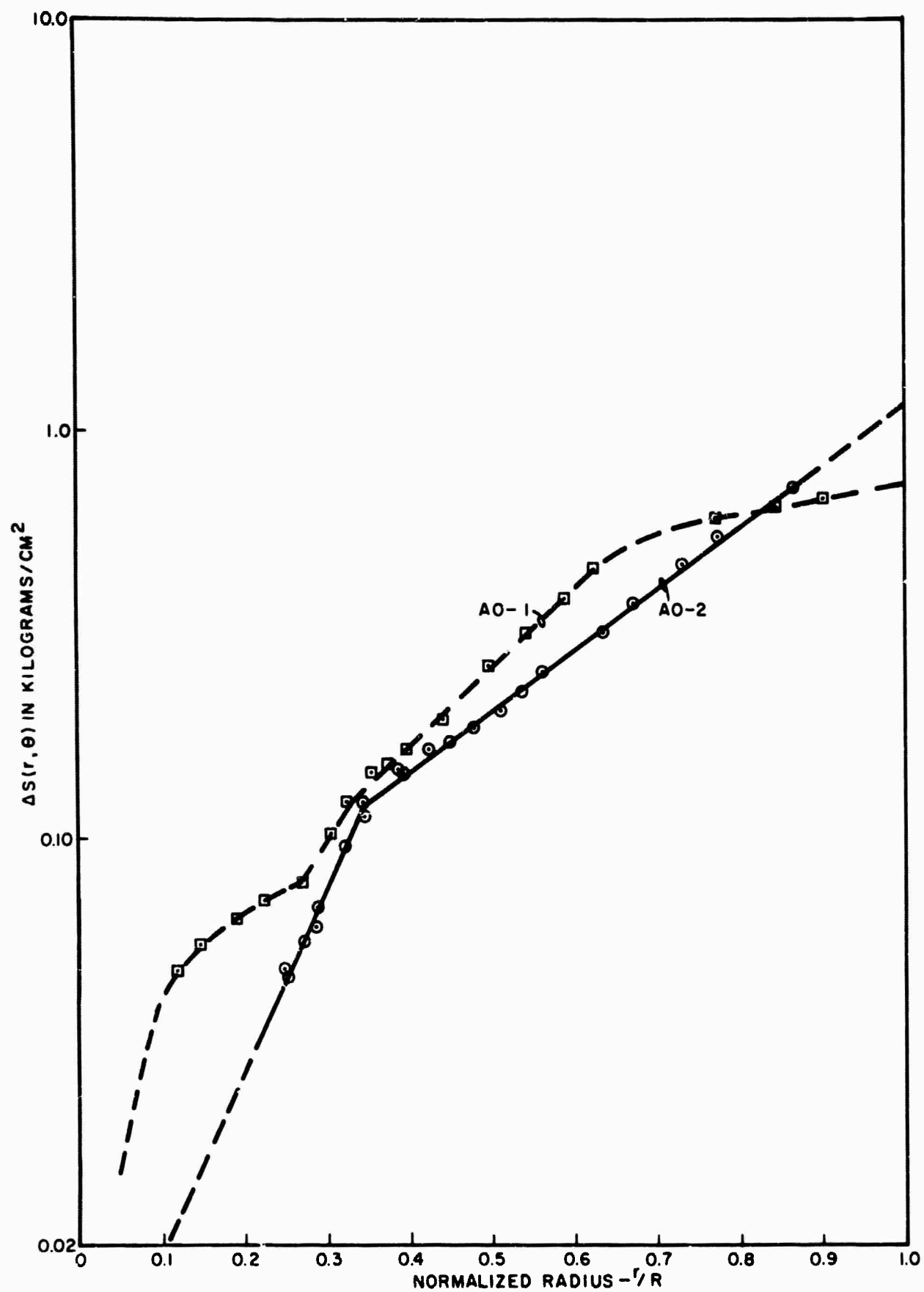
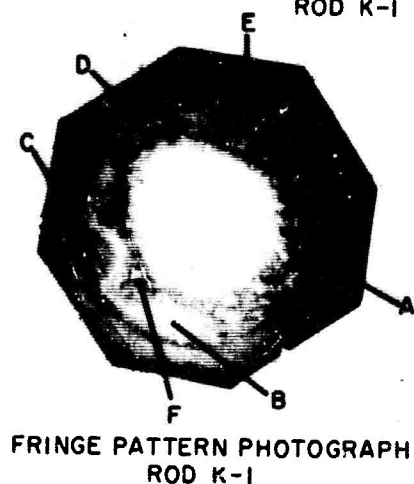
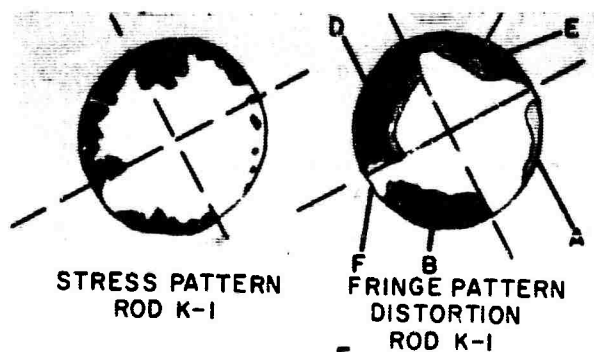


Figure A-4. Plot of $\Delta S(r, \theta)$ vs. r/R for AOlux Rods AO-1 and AO-2



NOTE: REGION MARKED C IS
BURNED SPOT ON
ANTI-REFLECTION COATING

Figure A-5a.

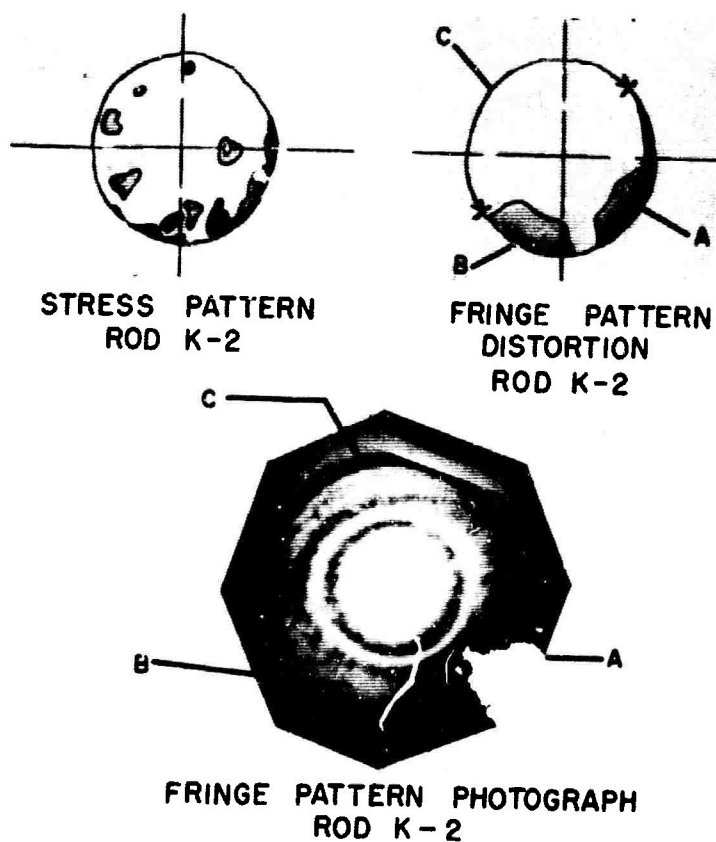


Figure A-5b.

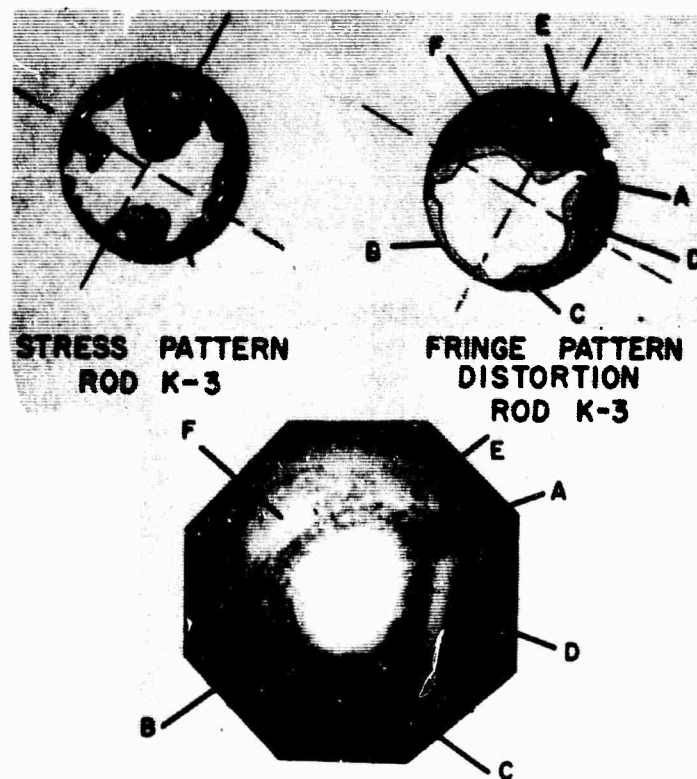


Figure A-5c.

that the effect is not identifiable when the optical gradients induced by the pump are also radially symmetric.

In addition to the Mach-Zehnder measurements, rod K-1 was placed in a plane polariscope and the pump-induced birefringence recorded by a high-speed framing camera. As in the case of the optical path length measurements, the birefringence pattern of rod K-1 was distorted in those regions of maximum residual stress. The birefringence pattern obtained is illustrated in figure A-6.



Figure A-6. Dynamic Birefringence in Rod K-1

In conclusion, there seems to be little doubt as to the effect residual stress has on the optical quality of a glass laser rod during the pumping period and that the resulting perturbations to the optical path length are quite important. This is particularly true when it is necessary to extract quantitative information from physical measurements of pump-induced birefringence and optical path length variations.

APPENDIX B

LASER ROD SUPPORT

APPENDIX B

LASER ROD SUPPORT

It has been found that the design of a laser rod support is quite important if it is necessary to observe only those distortions in the optical quality of a laser rod which are induced by direct absorption of pump radiation. Several support geometries were tested during the course of this contract, the object being to eliminate distortions to the laser rod optical quality which were directly traceable to the rod supports. After various supports were tested, the knowledge gained was used to design a support which introduced no observable distortions.

The first laser rod support tested was of all-brass construction, as illustrated in figure B-1. The Mach-Zehnder fringe patterns during the pump cycle were recorded for rod K-3* and were found to possess no radial symmetry. The developments of the distortion in the rod is illustrated in figure B-2a while figure B-2c shows the fringe pattern for rod K-3 in the absence of holder distortion.

Careful observation of the fringe development in figure B-2a indicated that the distortion appeared to originate at the area of contact (see figure B-1) between the brass and the laser rod. It appears that the most probable source of this distortion is that at the brass-glass interface the pump introduces an instantaneous temperature differential between the two materials due to unequal absorption of pump radiation.

The second design employed neoprene rubber O-rings to contact the rod equally around its circumference. The O-rings were recessed and shadowed to protect them from direct pump light irradiation. Figure B-3 shows the holder design, while figure B-2b shows the development of Mach-Zehnder fringes during the pump cycle. When the support was disassembled it was found that the neoprene O-rings had not been shielded from the pump light to as great a degree as had been hoped. The O-rings were badly burned in the region of contact between the O-rings and the laser rod. Again the distortion appeared to originate from the support-glass interface, which included the entire rod circumference.

*At the time of these tests rod A0-1 and A0-2 had not been received from the American Optical Company.

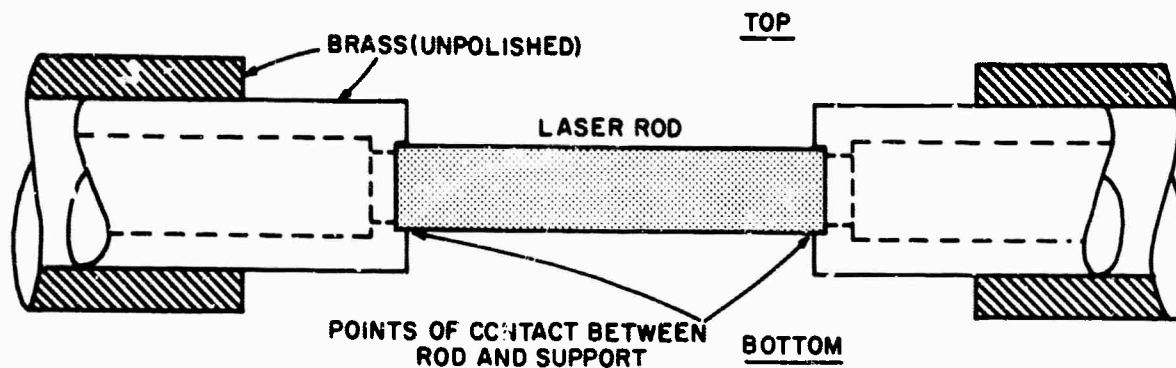


Figure B-1. Brass Laser Rod Support

A third type of holder was designed to take advantage of the small temperature rise experienced by fused quartz when placed in the pump cavity. This low temperature rise was attributed to the broad pass-band of fused quartz to pump radiation, and to the fact that the pyrex sheath removed the bulk of radiation which would have been absorbed by the quartz. Figure B-2c shows the development of the Mach-Zehnder fringe pattern while figure B-4

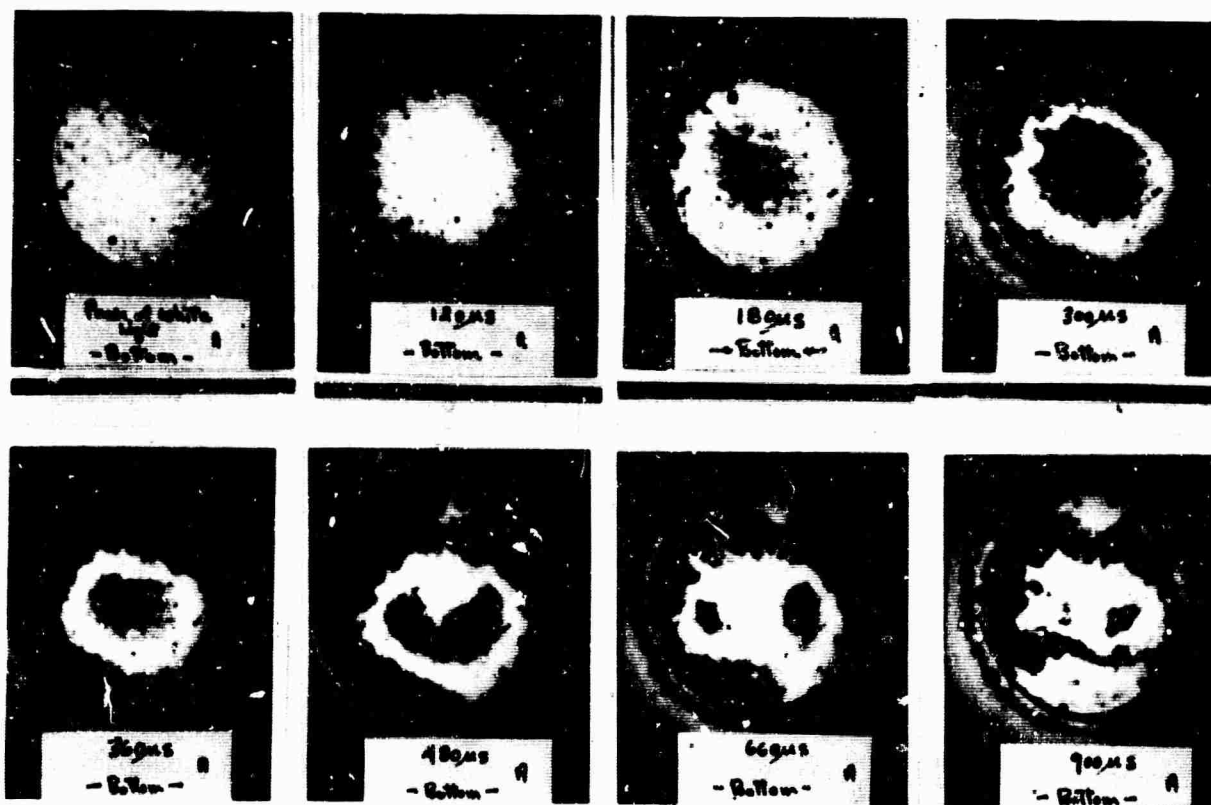


Figure B-2a. Fringe Patterns Obtained with Brass Laser Rod Support

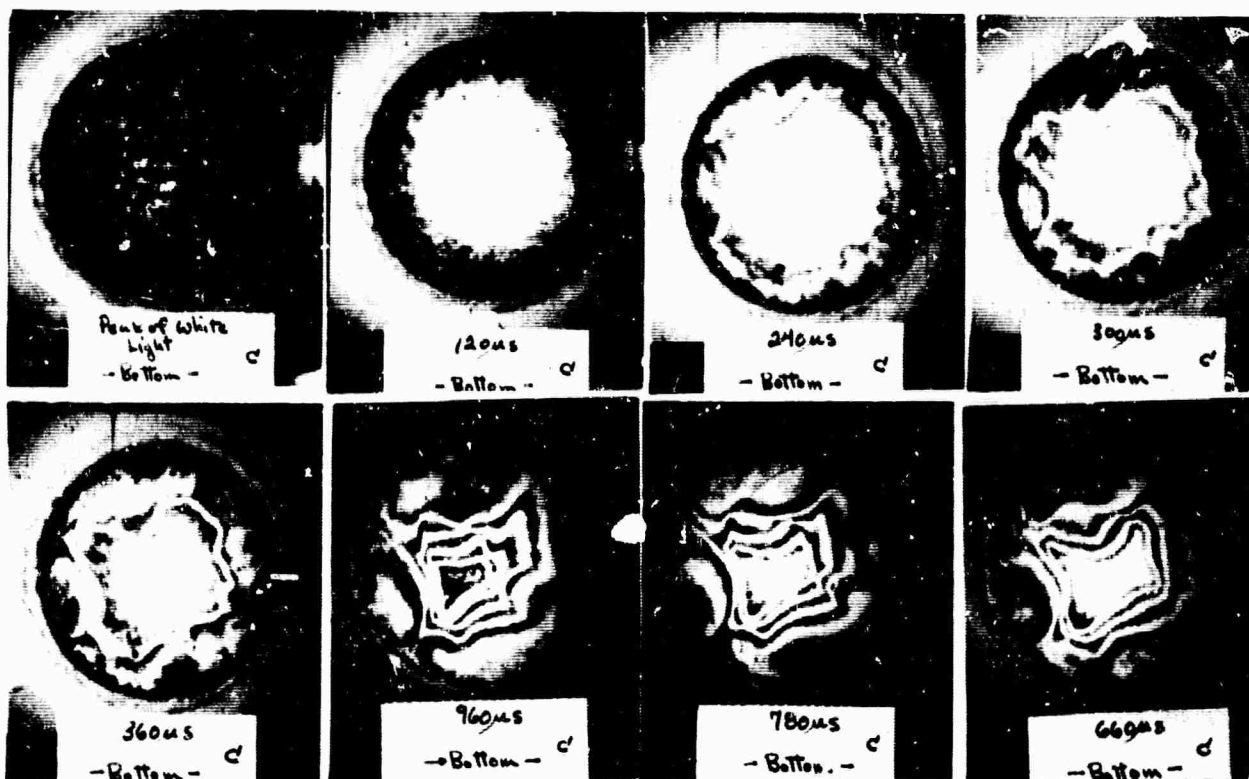


Figure B-2b. Fringe Patterns Obtained with Neoprene O-Ring Laser Rod Support

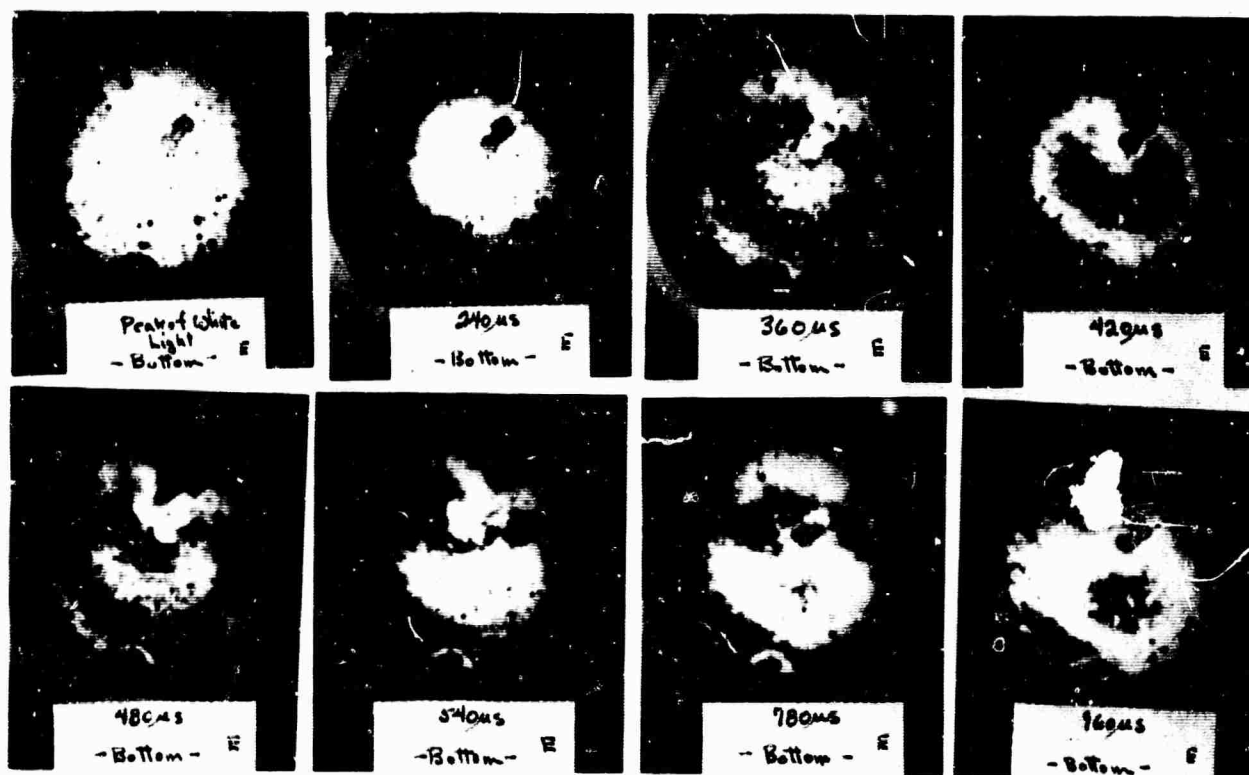


Figure B-2c. Fringe Patterns Obtained with Quartz Laser Rod Support

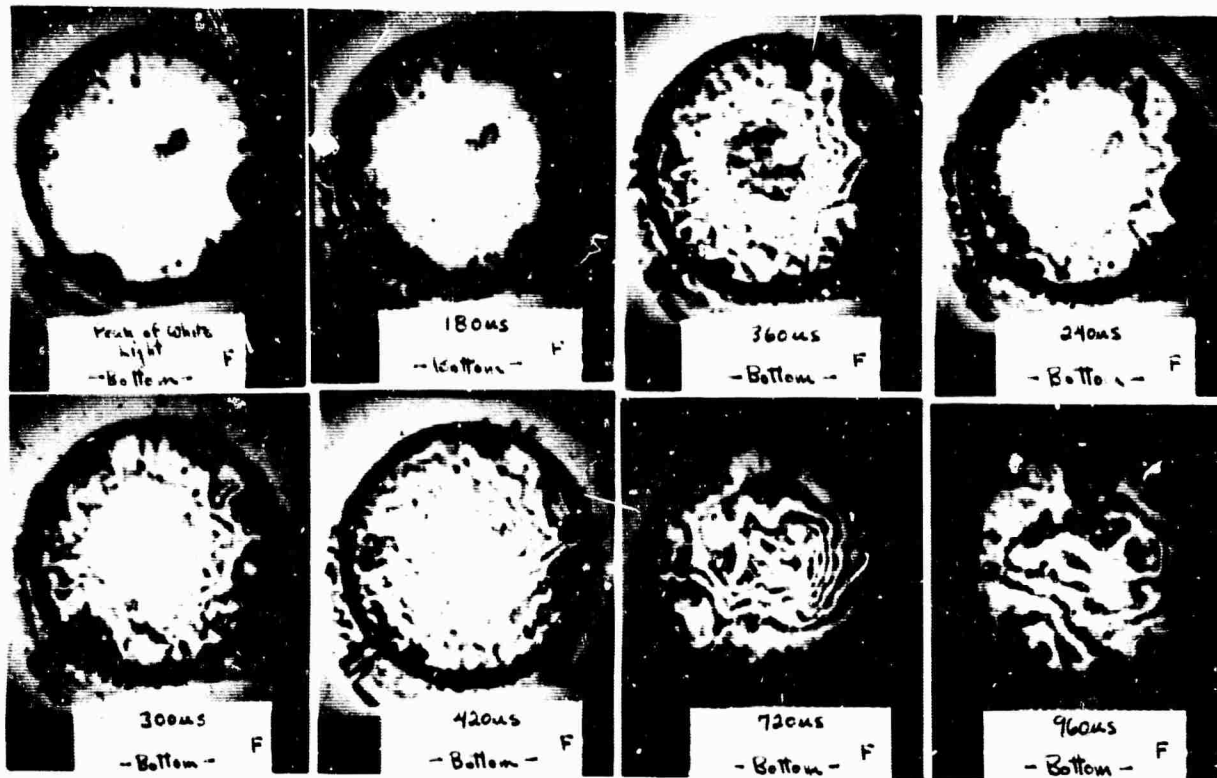


Figure B-2d. Fringe Patterns Obtained with Needle Laser Rod Support

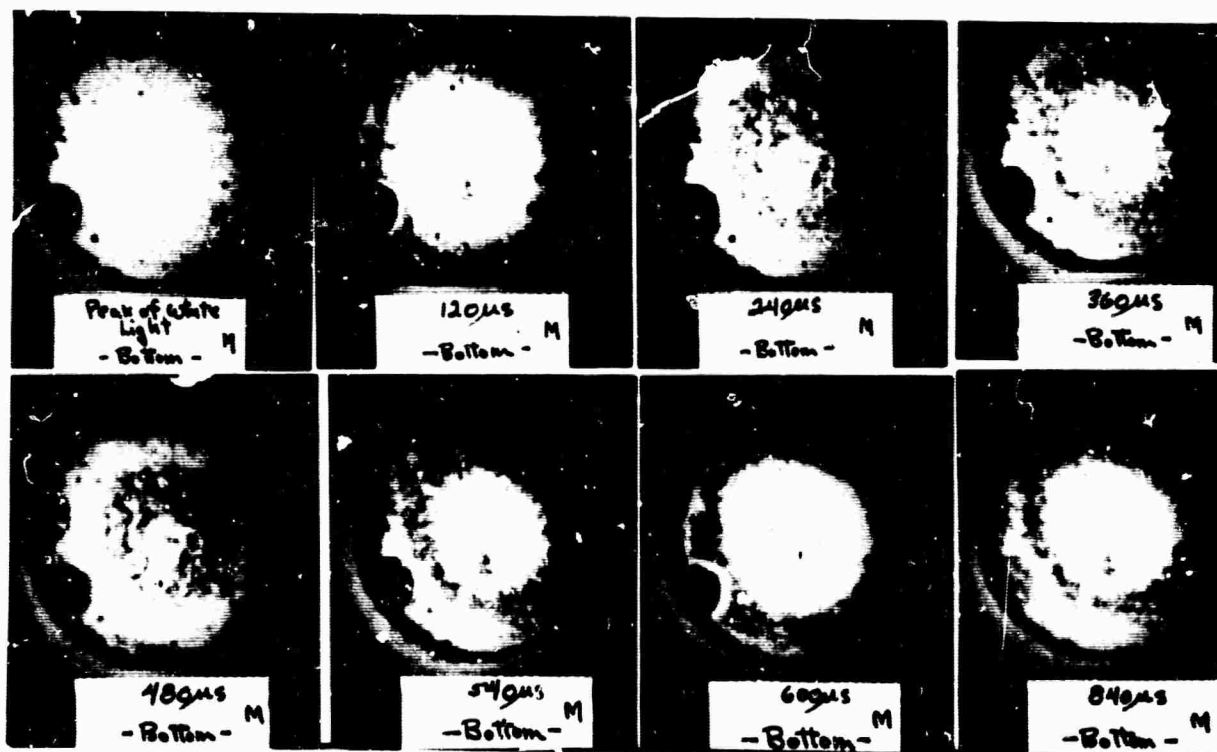


Figure B-2e. Fringe Patterns Obtained with "New Holder" Design Laser Rod Support

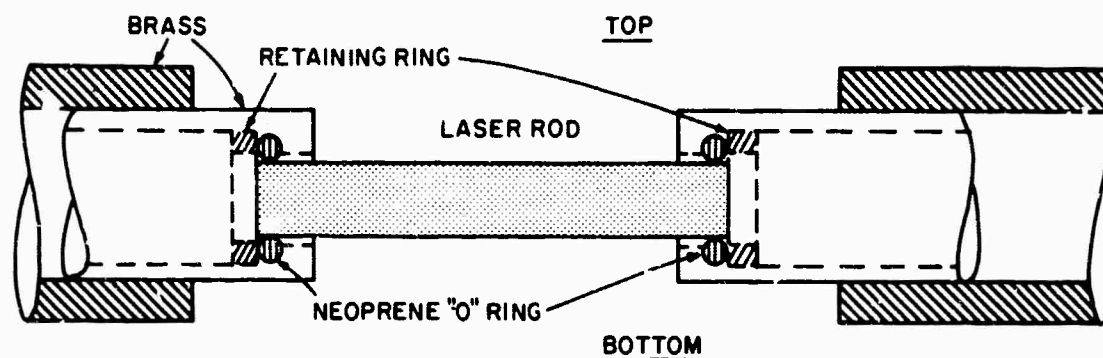


Figure B-3. Neoprene O-Ring Laser Rod Support

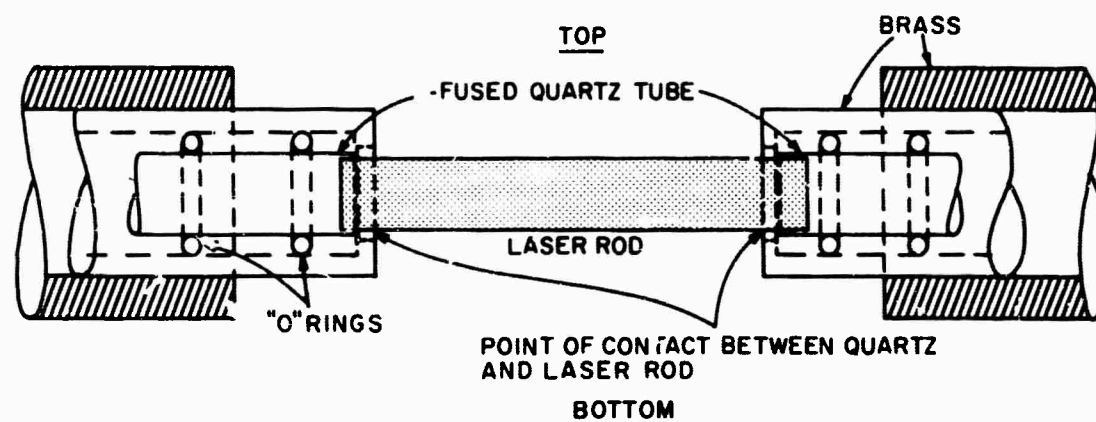


Figure B-4. Quartz Laser Rod Support

shows the holder design. It is interesting to note that the distortion was greatly reduced over that shown in figure B-2b; however, it was not completely eliminated. As before, the distortion appeared to originate from the region of contact between the rod and support.

After analysing the results obtained with the three previously described holders, all holders being characterized by a reasonably large area of contact between the support and rod, it was decided to support the rod on fine polished needle points. This approach led to the observation of optical path distortions which originated from heated air flowing across the face of the laser rod. Figure B-5 shows the support design while figure B-2d shows the development of the fringe pattern. As can be seen in figure B-5, the optical path in front of both ends of the laser rod was shielded from direct irradiation by the pump. In spite of this precaution, large distortion was observed. By means of a series of tests it was determined

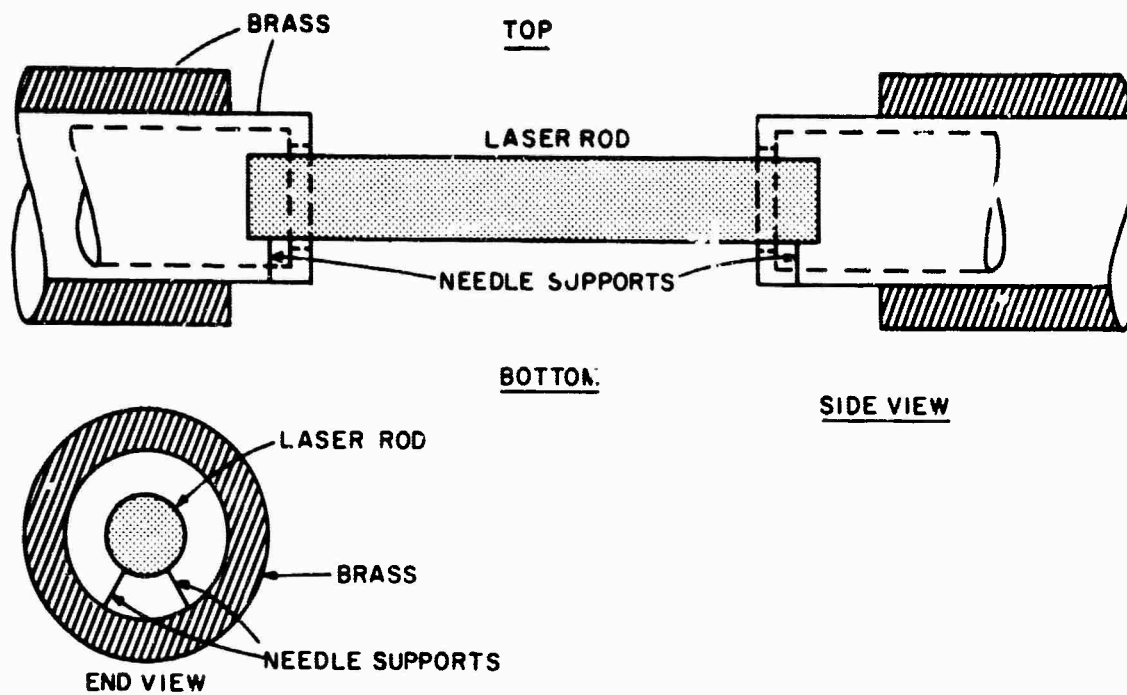


Figure B-5. Needle Laser Rod Support

that the distortions were caused by air being heated at the rod-air interface in the pumping cavity, flowing along the rod surface, and over the ends of the rod. These tests indicated that the air path in front of the laser rod must not only be blocked from direct pump irradiation but also from the air contained in the interior of the pumping cavity.

The final and successful rod support was designed on the basis of the information gained from the previously described experiments. A drawing of the complete design is shown in figure B-6. Figure B-2e shows the Mach-Zehnder fringe development, with holder-induced distortion being conspicuously absent. The only remaining distortion is that which is traceable directly to the residual strain in rod K-3. It was felt that the reason this design was successful in eliminating support distortions was that the Sylgard No. 182* O-rings are transparent and exhibit good thermal stability when partially exposed to pump illumination. Very little absorption of pump radiation takes place with a consequent small rise in temperature of the O-ring. In addition there is little if any alteration of the pump energy distribution in the vicinity of the O-rings. The Aluminum spacers (see figure B-6) were included so that the O-rings could be recessed varying amounts behind the end caps to prevent over-exposure of the O-rings to the pump illumination. For the maximum pump

*Dow Corning Trade Name

energy used throughout this contract, this holder allowed only .2 inch of each end of the rod to be shadowed.

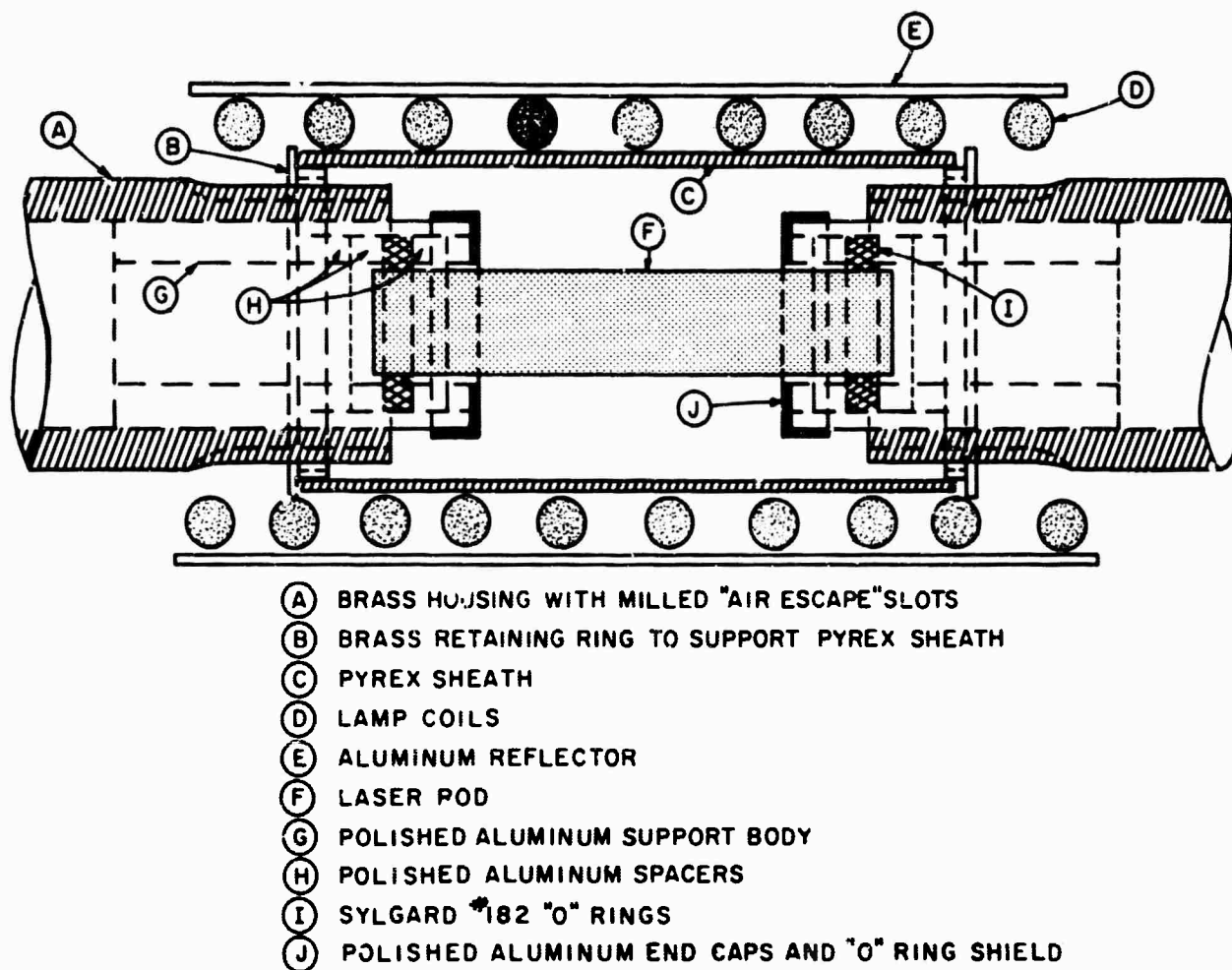


Figure B-6. Final Design of Laser Rod Support

APPENDIX C

PROPERTIES OF EASTMAN KODAK COMPANY
NEODYMIUM GLASS LASER RODS

APPENDIX C

PROPERTIES OF EASTMAN KODAK COMPANY
NEODYMIUM GLASS LASER RODS

A. MATERIAL IDENTIFICATION: Kodak Laser Glass, Type ND-10

B. OPTICAL PROPERTIES:

- | | |
|------------------------|---|
| 1. Glass | Eastman Kodak Rare Earth Optical Glass |
| 2. Doping | 1% and 3% by weight of neodymium oxide |
| 3. Emission Wavelength | 1.06 microns, ± 0.01 micron |
| 4. Line Width | approximately 150 Angstroms |
| 5. Absorption | see attached curve, Figure C-1 |
| 6. Index of Refraction | $N_D = 1.6970$ with 1% doping (ranges as high as 1.7030, depending on the concentration of neodymium) |

$$n_F - n_C = .01241$$

$$n_D - n_{A'} = .00803$$

$$n_e - n_C = .00675$$

$$n_F - n_D = .00874$$

$$n_g - n_F = .00673$$

$$n_h - n_g = .00559$$

7. Index Variation vs. Temperature*

$^{\circ}\text{C}$	$\Delta N_D (X10^{-5})$	$^{\circ}\text{C}$	$\Delta N_D (X10^{-5})$
100	11.8	-60	+1.2
80	8.0	-80	+3.0
60	5.0	-100	+5.2
40	2.7	-120	+7.5
20	1.1	-145	+10.5
0	0.0	-170	+13.3
-20	-0.5	-194	+15.7
-40	0.0		

*F. A. Molby, JOSA, Vol. 39, NO. 7,
July 1949

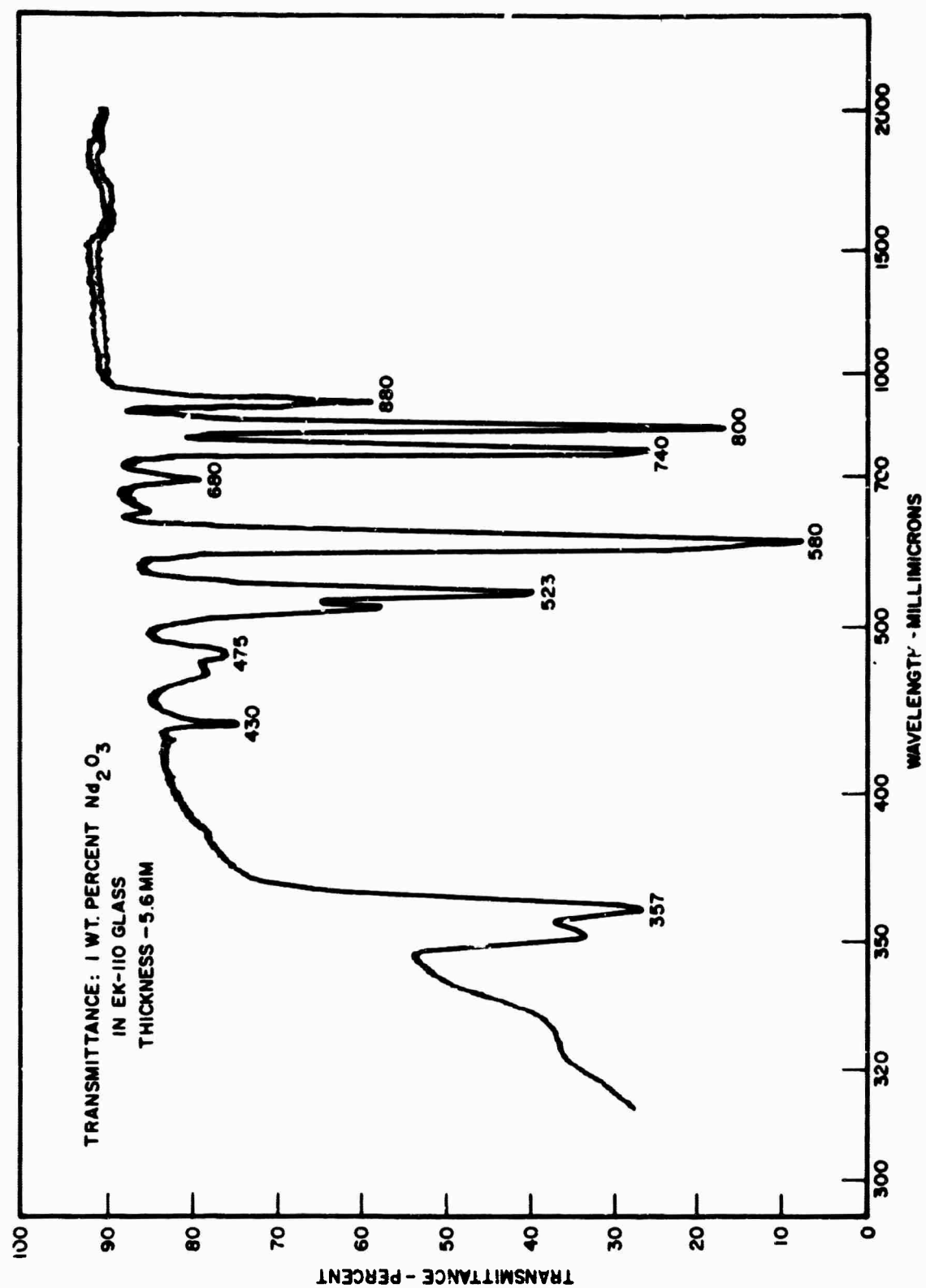


Figure C-1. Absorption Spectra of Kodak ND-10 Laser Glass

C. PHYSICAL PROPERTIES

- | | |
|---|--|
| 1. Specific Gravity | 4.1 gm/cc |
| 2. Coefficient of Expansion | (25°C - 125°C) 6.4×10^{-6} |
| 3. Water Solubility | Stains slightly after 8 hours in standard humidor test (100°F, 90% r.h.) |
| 4. Acid Solubility | Berger Class 5 |
| 5. Littleton Softening Point
($10^{7.6}$ Poise) | 701°C |
| 6. Littleton Anneal Point
($10^{13.0}$ Poise) | 628°C |
| 7. Littleton Strain Point
($10^{14.5}$ Poise) | 610°C |
| 8. Thermal Shock | Rods have been immersed from ambient room temperature into liquid nitrogen. After temperature stabilization, the same rods have been returned to ambient room temperature. No apparent damage has been observed. |
| 9. Thermal Conductivity (1% doping) | |

<u>Temperature</u>	<u>Thermal Conductivity</u> (Cal Sec ⁻¹ Cm ⁻² °C ⁻¹ Cm)
52°C	.0019
69°C	.0021
91°C	.0021
114°C	.0022
138°C	.0023
164°C	.0023
196°C	.0024

10. Modulus of Rupture (1% doping)

<u>Temperature</u>	<u>Modulus of Rupture (psi)</u>
25°C	17,600
100°C	20,500
250°C	18,200

11. Modulus of Elasticity (1% doping)

<u>Temperature</u>	<u>Modulus of Elasticity (psi x 10⁶)</u>
25°C	14.4
100°C	15.0
250°C	16.6

D. END SURFACE COATINGS

1. Either dielectric coatings or anti-reflection coatings can be supplied. Dielectric coatings are optimized performance at 1.07 microns. Because of the low loss coefficient of this glass, special low-absorption dielectric coatings are required. Silver coatings are not recommended.

2. Standard anti-reflection coatings should be applied to rods intended for use with external mirrors.

E. LASER PERFORMANCE

- | | |
|-------------------------------|---|
| 1. Loss Coefficient | 0.16%/cm |
| 2. Efficiency | 0.5 to 2.5%, dependent on rod and flash tube geometry and coupling. |
| 3. Threshold | Threshold is dependent upon many variables, and specific values cannot be stated. Type ND-10 Glass is characterized by low threshold. Figures ranging around 4 joules have been reported. |
| 4. Power Output | Greater than 1 joule per cubic centimeter of glass. |
| 5. Fluorescence Time Constant | Type ND-10 Glass has a fluorescence life-time of about 60 microseconds. |

6. Beam Divergence Output divergence from a Type ND-10 rod, 2" long x 1/4" diameter, has been measured at less than 2 milliradians. This can be reduced with remote external mirrors or external mode selection.
7. Low Temperature Operation Cooling may be desirable to maintain ambient conditions at high repetition rates. However, the fluorescence transition responsible for laser action terminates well above ground state and this laser glass does not require refrigeration for its operation.

F. SPECIFICATIONS AND AVAILABILITY

1. Sizes

Kodak laser rods, finished, are available in sizes up to 3/4" diameter x 30" long.

2. Configurations

- a. Rods can be supplied with flat ends, spherical ends, chisel-tipped internally-reflecting ends, Brewster's angle, or any combination of these.
- b. They are not presently offering clad rods of this material.

3. Standard Size Tolerances

- a. Diameter +.000", -.005"
- b. Length +.000", -.020"

4. Finish Tolerances

- a. End flatness held to 0.1 wave.
- b. End parallelism held to 6 seconds of arc.
- c. The cylindrical surface is normally finished to an optical shine, but can be supplied with a more precise optical polish, or fine ground, on a custom basis.

5. Laser Rod Testing

- a. Every finished laser rod will be optically tested, using a Twyman-Green interferometer with a gas laser source, checking optical homogeneity of the material as well as end flatness and parallelism. With multi-layer dielectric end coatings, this can be done after the rod is coated and at any time during its useful life.**
- b. Every finished rod will be lased before shipment, but with no guarantee on the nature of its performance, since there is so much variation between optical heads and pump systems.**

6. Delivery

- a. Certain smaller rods will be stocked for immediate delivery.**
- b. Special orders and custom configurations can usually be shipped in 30 to 60 days. If a special glass melt is necessary, delivery will be 60 to 90 days.**

(All of the above material is from specifications supplied by Eastman Kodak Company.)

APPENDIX D

PROPERTIES OF AMERICAN OPTICAL AOLUX NEODYMIUM GLASS LASER RODS

BLANK PAGE

GENERAL SPECIFICATIONS

Solid and Clad AOLux Laser Rods

<u>Length</u>	±0.20"
<u>Diameter</u>	±0.005" (up to 1/4" diameter) ±0.010" (up to 20" length) ±0.020" (over 20" length)

End Specification:

<u>Flatness</u>	1/10 wave at 1.06 microns
<u>Perpendicularity</u>	90° ±2 min. to rod axis
<u>Parallelism</u>	10 sec. arc (up to 1/4" diameter) 6 sec. arc (over 1/4" diameter)
<u>Brewster Angle</u> ($\theta_B = 56^\circ 30'$)	$\theta_B \pm 30$ min. arc
<u>Parallelism between Brewster faces</u>	8 min. arc to axis 15 min. to normals
<u>Roof ends centering</u>	±.003" (under 1/4" diameter) ±.005" (1/4" diameter) ±.008" (over 1/4" diameter)

Typical Properties of AOLux

<u>Material</u>	Nom. 5 wt. % Nd_2O_3 in barium crown optical glass $n_D = 1.519$ $V = 56.6$ $n_{1.06} = 1.509$
<u>Physical Properties</u>	Strain point = 450°C Linear Expansion Coeff. (50-300°C.) = $10.3 \times 10^{-6}/^\circ\text{C}$ Density = 2.62 gm/cm ³ Water Solubility 0.053 microns (powder test) Thermal Conductivity = .002 cal/sec/cm/°C. Number Nd ions/cc = 4.6×10^{20}
<u>Laser Properties</u>	Wavelength = 1.06 microns Fluorescent line width: at 1.06 microns = 180 Å at 77°K. at half width = 250 Å at 300°K. Lifetime = 0.57 milliseconds Specific gain/cm/joule stored/cm ³ = .08

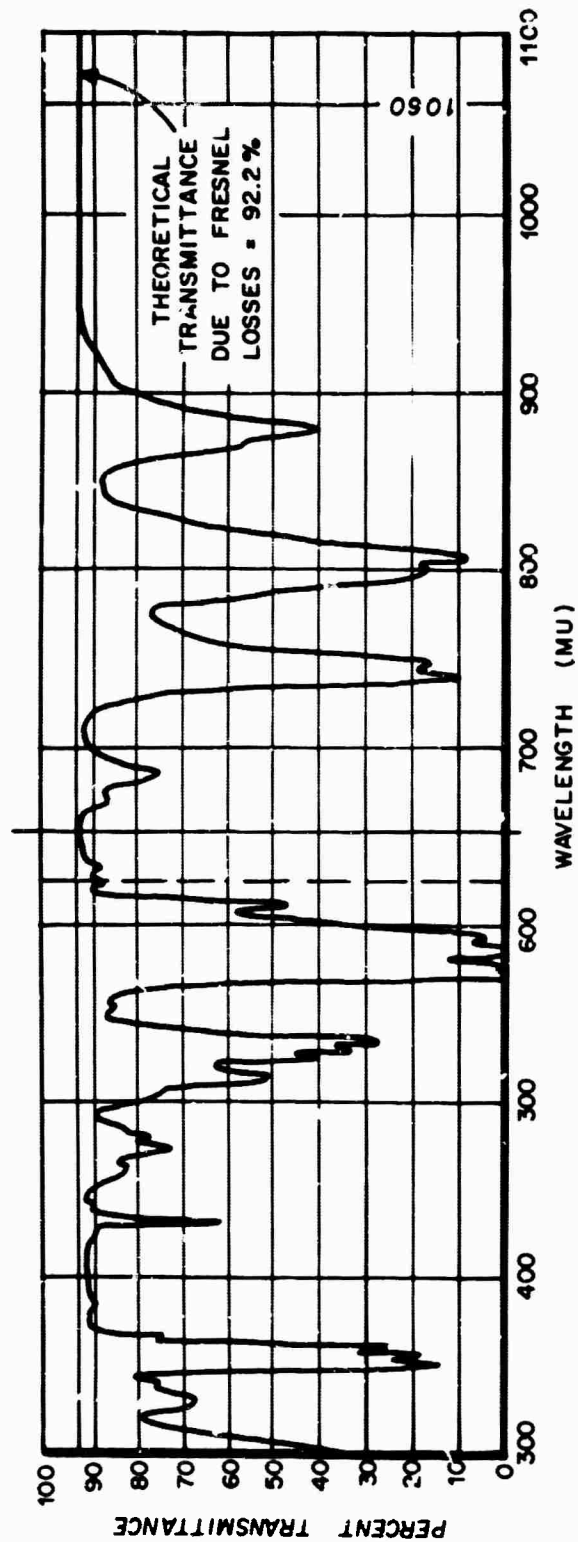


Figure D-1. Absorption Spectrum of AOlux
Sample Thickness: 6.4 mm

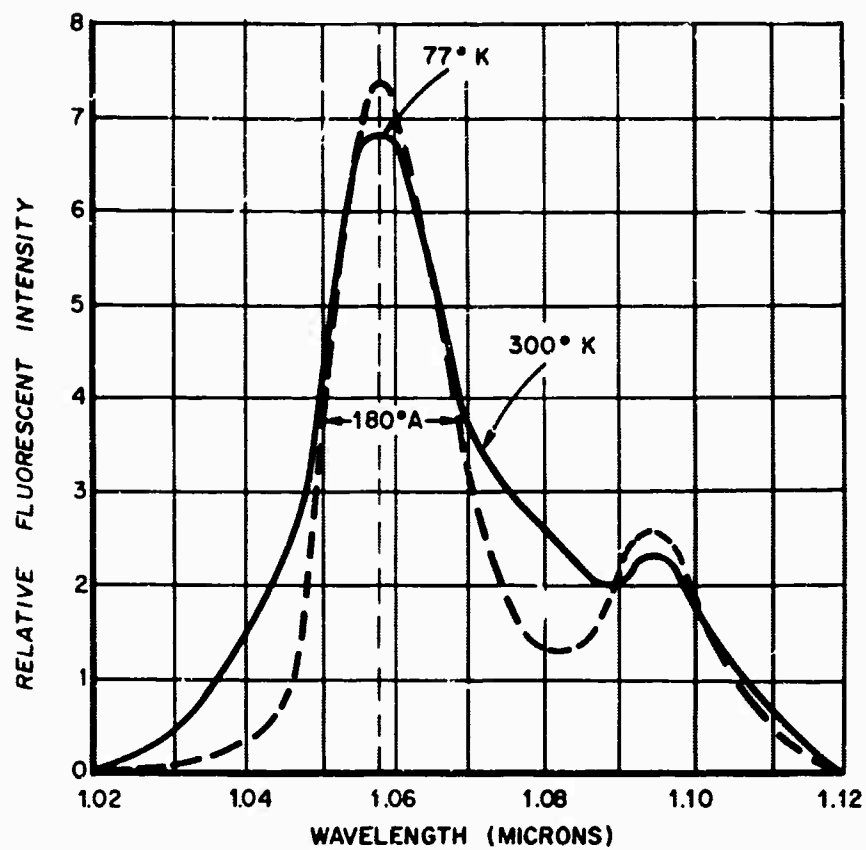


Figure D-2. Fluorescence of AOlux (5% Nd₂O₃)

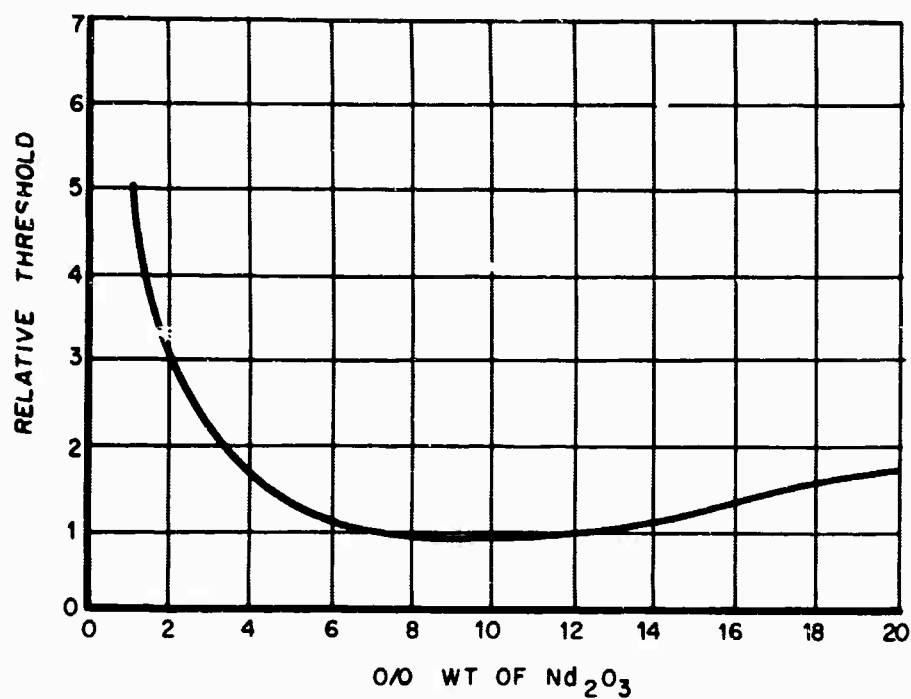


Figure D-3. Relative Threshold vs % Wt of Nd_2O_3

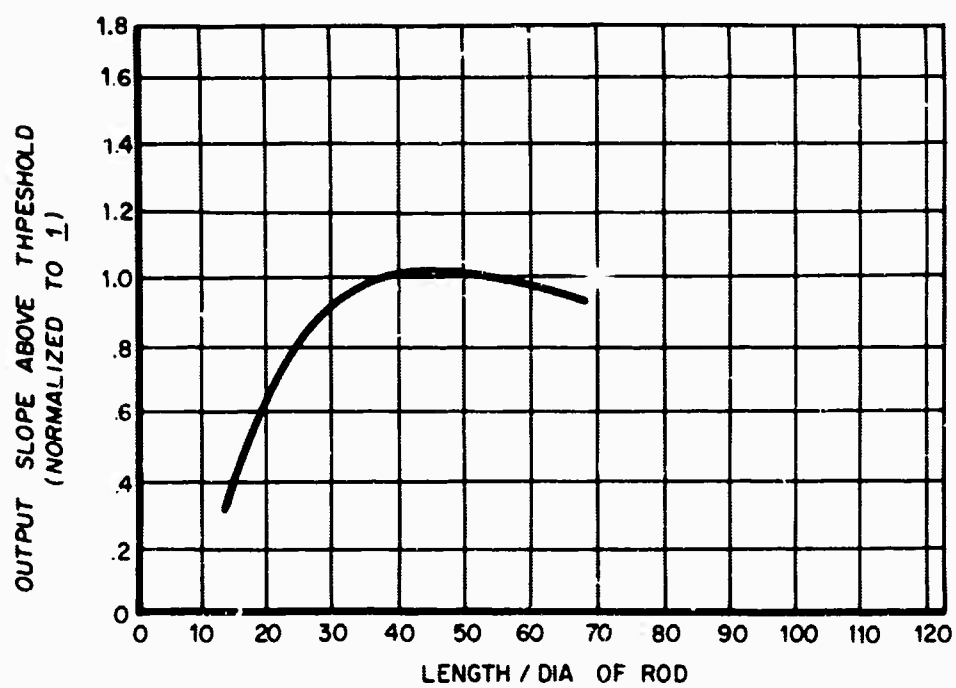


Figure D-4. Output Slope Versus Rod Length/Diameter Ratio

APPENDIX E

ANNEALING PROCEDURE USED FOR RODS AO-1 AND AO-2

APPENDIX E

ANNEALING PROCEDURE USED FOR RODS AO-1 AND AO-2

Processing Steps

After drawing from the melt, the rod temperature was dropped from the annealing point to the strain point at a rate of approximately 1°F per hour.

The rods were fabricated from the rough boule:

- 1) Machined to final dimensions (3/8 x 3")
- 2) Rough ground surface finish applied
- 3) Ends ground and polished to specifications. (See Appendix D.)

The rods were reannealed by holding the rod at the annealing temperature for 20 hours, and dropping the temperature at a rate of .25°F per hour until the strain point was reached.

After final annealing, the flatness of the ends was checked, and the rods were re-polished (not reground) to meet specifications.

American Optical suggested that the laser rods not be anti-reflection coated, since previous experience had shown that strain can be introduced if proper precautions are not taken during the vapor deposition process.

APPENDIX F

PHYSICAL CONSTANTS FOR AOLUX ROD AO-2

APPENDIX F

PHYSICAL CONSTANTS FOR AOLUX ROD AC-2*

- 1) E (Young's Modulus) = $6.98 \times 10^5 \text{ kg/cm}^2$
- 2) ν (Poisson's Ratio) = .225
- 3) $\alpha_n = 1.25 \pm .66 \times 10^{-6}/^\circ\text{C}$
- 4) $n_o = 1.515$ (estimated value at 6328 \AA)
- 5) $B_\perp = 3.5 \pm .6 \times 10^{-7} \text{ cm}^2/\text{kg}$
- 6) $B_\parallel = .42 \pm .13 \times 10^{-7} \text{ cm}^2/\text{kg}$
- 7) α (Expansion Coefficient) = $.905 \pm .05 \times 10^{-5}/^\circ\text{C}$ (at 25°C)
- 8) C (Specific Heat) = $.15 \text{ cal/gm}/^\circ\text{C}$ (at 25°C)
- 9) K_c (Thermal Conductivity) = $.002 \text{ cal/sec/cm}/^\circ\text{C}$
- 10) γ (Density) = 2.63 gm/cm^3
- 11) τ_{31} (Flourescent Time Constant) = $.585 \pm .015 \times 10^{-3}$ seconds
- 12) N_o (Nd^{+3} Ion Density) = $4.6 \times 10^{20}/\text{cc}$
- 13) $n_o \alpha \left[\frac{2P}{V_o} + \frac{q}{V_o} \right] = 5.2 \pm 1.2 \times 10^{-6}/^\circ\text{C}$
- 14) $\left(\frac{J_n}{JT} \right) \rho = 3.3 \pm 1.1 \times 10^{-6}/^\circ\text{C}$
- 15) ℓ_o (Length of Rod) = 7.62 cm
- 16) $R = .476 \text{ cm}$
- 17) $\lambda_o = 1.06 \times 10^{-4} \text{ cm}$
- 18) $\Delta\lambda$ (1.06μ flourescent line $1/2$ width) = $2.5 \times 10^{-6} \text{ cm}$

* (American Optical 3835 glass, 5% Nd^{+3} doping) used during this contract.

DOCUMENT CONTROL DATA - R&D

(Security classification of title, body of abstract and indexing annotation must be entered when the overall report is classified)

1. ORIGINATING ACTIVITY (Corporate author) Westinghouse Electric Corporation		2a. REPORT SECURITY CLASSIFICATION UNCLASSIFIED	
		2b. GROUP Surface Division	
3. REPORT TITLE Thermal Optic Distortion			
4. DESCRIPTIVE NOTES (Type of report and inclusive dates) Final Report, 16 June, 1965 to 1 October, 1966			
5. AUTHOR(S) (Last name, first name, initial) Riedel, E. P., Baldwin, G. D.			
6. REPORT DATE 31 October, 1966	7a. TOTAL NO. OF PAGES 111	7b. NO. OF REFS 21	
8a. CONTRACT OR GRANT NO. NONr-4874(00)	8b. ORIGINATOR'S REPORT NUMBER(S) Final Report		
b. PROJECT NO. ARPA Order No. 306			
c. Project Code 4730	8d. OTHER REPORT NO(S) (Any other numbers that may be assigned this report) MDE 1198		
10. AVAILABILITY/LIMITATION NOTICES By Authority of Office of Naval Research			
11. SUPPLEMENTARY NOTES		12. SPONSORING MILITARY ACTIVITY Office of Naval Research	
<p>13. ABSTRACT The Final Report on Contract Nonr-4874(00) "Thermal Optic Distortion" quantitatively describes the optical distortion in neodymium doped glass which is induced by pump radiation. We have observed optical distortion at 6328A and have found the optical path length dependent on four primary effects:</p> <ol style="list-style-type: none"> 1) Change in physical length 2) Change in refractive index due to temperature rise 3) Change in index resulting from stress 4) Change in index associated with an excited state population of neodymium ions. <p>Section I presents the experimental techniques used and the results obtained throughout this contract. Included in this section are measurements of optical path length variations, pump-induced birefringence, change in physical length, change in refractive index, bulk temperature rise, and the deflection of a light beam.</p> <p>In Section II, the theory of thermal optic distortion is developed for the first time to include Fermat's principle. This approach leads to equations defining both the slope and trajectory of rays through the material. The resulting equations are employed to predict ray refraction, beam divergence, and the</p>			

optical path length through the material as a function of radius, time, and polarization.

Section III compares the results of Sections I and II. Good agreement between theory and experiment is achieved provided a new term is added to the expression for the change in refractive index. This term arises from the fact that the polarizability of the neodymium ion in its excited $^4F_{3/2}$ level is different from its value in the $^4I_{9/2}$ ground level. The inclusion of this new term in the expression for the change in refractive index implies that large optical distortions can exist in "athermalized" glass.